

UNIVERSITY OF ALBERTA

**Mechanical, Electrochemical and Tribological  
Properties of Nanocrystalline Copper Deposit Produced  
by Pulse Current Electrodeposition**

by

**Song Tao**



A thesis submitted to the Faculty of Graduate Studies and Research in  
partial fulfillment of the requirements for the degree of Master of Science

in

Materials Engineering

Department of Chemical and Materials Engineering

Edmonton, Alberta

Fall 2006



Library and  
Archives Canada

Bibliothèque et  
Archives Canada

Published Heritage  
Branch

Direction du  
Patrimoine de l'édition

395 Wellington Street  
Ottawa ON K1A 0N4  
Canada

395, rue Wellington  
Ottawa ON K1A 0N4  
Canada

*Your file* *Votre référence*  
*ISBN: 978-0-494-22384-0*  
*Our file* *Notre référence*  
*ISBN: 978-0-494-22384-0*

**NOTICE:**

The author has granted a non-exclusive license allowing Library and Archives Canada to reproduce, publish, archive, preserve, conserve, communicate to the public by telecommunication or on the Internet, loan, distribute and sell theses worldwide, for commercial or non-commercial purposes, in microform, paper, electronic and/or any other formats.

The author retains copyright ownership and moral rights in this thesis. Neither the thesis nor substantial extracts from it may be printed or otherwise reproduced without the author's permission.

**AVIS:**

L'auteur a accordé une licence non exclusive permettant à la Bibliothèque et Archives Canada de reproduire, publier, archiver, sauvegarder, conserver, transmettre au public par télécommunication ou par l'Internet, prêter, distribuer et vendre des thèses partout dans le monde, à des fins commerciales ou autres, sur support microforme, papier, électronique et/ou autres formats.

L'auteur conserve la propriété du droit d'auteur et des droits moraux qui protègent cette thèse. Ni la thèse ni des extraits substantiels de celle-ci ne doivent être imprimés ou autrement reproduits sans son autorisation.

---

In compliance with the Canadian Privacy Act some supporting forms may have been removed from this thesis.

Conformément à la loi canadienne sur la protection de la vie privée, quelques formulaires secondaires ont été enlevés de cette thèse.

While these forms may be included in the document page count, their removal does not represent any loss of content from the thesis.

Bien que ces formulaires aient inclus dans la pagination, il n'y aura aucun contenu manquant.

  
**Canada**

## ABSTRACT

Nanocrystalline materials have attracted extensive interest due to their improved mechanical, physical and chemical properties. Although electrodeposition has been one of the methods for synthesizing nanocrystalline materials, properties of nanocrystalline electrodeposits are less evaluated.

In this work, nanocrystalline and microcrystalline copper deposits were produced by pulse and direct current electrodeposition processes, respectively. Effects of deposition parameters were investigated for the purpose of controlling the grain size. Mechanical and tribological properties of deposits were investigated using nanoindentation, nanoscratch and microscratch techniques. It was demonstrated that the nanocrystalline deposit shows higher hardness, lower friction coefficient and lower wear rate. The surface stability and corrosion behavior of the deposits were evaluated using Scanning Kelvin Probe, electrochemical polarization and impedance techniques. The synergism of corrosion and wear was investigated using an electrochemical scratch technique. Results indicate that the nanocrystalline surface is more electrochemically stable than the microcrystalline one due to the formation of a stronger and more protective passive film.

## ACKNOWLEDGEMENTS

I would like to express my thanks to the people who have helped me during my M.Sc study at the University of Alberta.

First of all, sincere appreciation is given to my supervisor, Dr. D.Y.Li, for his support, advice and guidance throughout the course of my graduate program. He has been an excellent model of a researcher who has made seeking truth his academic career. I will always treasure the supervision he has given me.

I would like to thank Dr. X.Y.Wang for his assistance in using various instruments and valuable discussions throughout this work. Appreciation also goes to Dr. H.Zhang, Dr. X.S.Guan and Dr. W.Li for sharing the knowledge with me.

I am so happy to have been working with my colleagues in the Surface/Tribology Lab: Yanping Li, Jing Hu, Qiang Chen, Iulian Radu, Saheed Akonko, Songbo Yin and Bin Yu. Discussions with them gave me a new perspective on thinking. I would like to express my special thanks to Yanping, who has always encouraged and helped me in both my study and life.

Most importantly, I would like to offer thanks for the unconditional support and love given me by my father Mr. Baoning Tao, my mother Ms. Jingsheng Guo, my twin sister Ms. Lin Tao and my fiance Mr. Yao Wang; it helped me to bring this work to completion.

# CONTENTS

<b>1</b>	<b>Introduction and Literature Review</b>	<b>1</b>
1.1	Nanocrystalline Materials and Their Synthesis Methods . . . . .	1
1.2	Fabrication of nc-materials by pulse-current electrodeposition . .	5
1.3	Characterization of Structure and Property . . . . .	11
1.4	Properties of nanocrystalline Metals and Alloys . . . . .	22
1.5	Objectives of This Study . . . . .	27
<b>2</b>	<b>Processing Study and Mechanical Property</b>	<b>29</b>
2.1	Introduction . . . . .	29
2.2	Specimen Preparation . . . . .	31
2.3	Surface Morphology . . . . .	32
2.4	Grain Size Determination . . . . .	35
2.5	Mechanical Property . . . . .	41
2.6	Grain Size Control and Processing Parameters . . . . .	44
2.7	The Relation Between Hardness and Grain Size at Nano-scale .	56
2.8	Conclusions . . . . .	57
<b>3</b>	<b>Electrochemical Behavior and Stability</b>	<b>59</b>
3.1	Introduction . . . . .	59
3.2	Experimental Procedure . . . . .	60

3.3	Polarization Behaviors of nc-Cu Deposits in Different Corrosive Media . . . . .	63
3.4	Corrosion Study of Nanocrystalline and Microcrystalline Cu deposits . . . . .	68
3.5	Surface Stability of nc- and mc- Cu Deposits . . . . .	69
3.6	Electrochemical Impedance Spectroscopy Analysis . . . . .	74
3.7	Discussion . . . . .	83
3.8	Conclusions . . . . .	85
<b>4</b>	<b>Tribological Properties</b>	<b>87</b>
4.1	Introduction . . . . .	87
4.2	Experimental details . . . . .	88
4.3	Friction Behavior . . . . .	89
4.4	Wear Behavior . . . . .	94
4.5	Conclusions . . . . .	97
<b>5</b>	<b>Synergism of Corrosion and Wear</b>	<b>98</b>
5.1	Introduction to Synergism of Corrosion and Wear . . . . .	98
5.2	Fundamentals of the Analysis Method . . . . .	100
5.3	Experimental Details . . . . .	103
5.4	Results . . . . .	105
5.5	Synergistic Effect of Corrosion and Wear . . . . .	110
5.6	Conclusions . . . . .	115
<b>6</b>	<b>General Conclusions</b>	<b>117</b>
	<b>Bibliography</b>	<b>119</b>

## LIST OF TABLES

1.1	Possible effects of plating parameters $t_{on}$ and $t_{off}$ on the deposit structure [1]. . . . .	10
2.1	Electrolytes and deposition parameters for Cu deposition. . . . .	32
2.2	Mechanical properties of nc- and mc-Cu deposits determined by nano-indentation under 50 and 100 $\mu\text{N}$ . . . . .	41
2.3	Deposition parameters for Cu deposits, whose force-displacement curves are illustrated in Figure 2.8. . . . .	45
2.4	Effect of $t_{off}$ on the grain size and nano-hardness of deposits produced at low and high $I_p$ . . . . .	48
2.5	Effect of $t_{on}$ on the grain size of deposits produced at low and high $I_p$ . . . . .	52
3.1	Passivation parameters obtained from polarization curves of nanocrystalline (56nm) and microcrystalline (2 $\mu\text{m}$ ) copper deposits in different solutions. . . . .	67
3.2	EWFs of nanocrystalline (56nm) and microcrystalline (2 $\mu\text{m}$ ) Cu deposits after immersion in different solutions. . . . .	69

5.1	Volume loss rates ( $\mu\text{m}^3/\text{s}$ ) of nanocrystalline (56nm) and microcrystalline ( $2\mu\text{m}$ ) Cu determined by electrochemical scratch technique under a load of 20g, at a scratch velocity of 5mm/s in different solutions. . . . .	107
5.2	Volume loss rates ( $\mu\text{m}^3/\text{s}$ ) of nanocrystalline (56nm) and microcrystalline ( $2\mu\text{m}$ ) Cu determined by electrochemical scratch technique under a load of 40g, at a scratch velocity of 5mm/s in different solutions. . . . .	107
5.3	The ratios of volume loss rates caused by corrosion, wear and synergism. . . . .	111

## LIST OF FIGURES

1.1	Schematic potential and electrode kinetics. . . . .	6
1.2	Scheme of the pulse waveform . . . . .	8
1.3	X-ray diffraction patterns (111-reflections) of nanocrystalline copper deposits prepared from electrolytes with variable citric acid content. . . . .	11
1.4	TEM micrographs of electrodeposited nanocrystalline Ni: (a)bright field, (b)dark field, (c)electron diffraction pattern, and (d)grain size distribution . . . . .	13
1.5	A Multi-Atomic Force Microscope (AFM). . . . .	14
1.6	AFM tip and cantilever (a)schematic illustration, and (b)electron micrograph of a cantilevered probe . . . . .	15
1.7	Schematic of indent and compliance curve (load vs displacement) for an elastic-plastic specimen, loading and unloading, from a nanoindentation experiment with maximum load $P_t$ and depth beneath the specimen free surface $h_t$ . The depth of the contact circle $p$ and slope of the elastic unloading $dp/dh$ allow specimen modulus and hardness to be calculated. $h_r$ is the depth of the residual impression, and $h_e$ is the displacement associated with the elastic recovery during unloading. . . . .	19

1.8	(a) Electron micrograph of a Berkovich tip and (b) an AFM contact mode image of a nano-dent. . . . .	20
1.9	Schematic representation of the variation in yield stress as a function of grain size in microcrystalline and nanocrystalline metals and alloys [2]. . . . .	22
2.1	AFM images of as-deposited Cu deposits produced using different electrodeposition methods: (a) DC, and (b) PC (scanned area = $10 \times 10 \mu\text{m}^2$ ). . . . .	33
2.2	A schematic illustration illustrating how a change in current density affects the surface irregularity of plated films. . . . .	35
2.3	X-ray diffraction patterns of a PC-plated Cu deposit and an annealed sample of pure Cu: (a) (111), (200) and (220) peaks, and (b) magnified (111) peaks for grain-size analysis. . . . .	36
2.4	AFM image of a nanocrystalline Cu deposit produced by PC electrodeposition (friction mode). . . . .	39
2.5	Optical microscopic image of a microcrystalline Cu deposit produced by DC electrodeposition. . . . .	40
2.6	Nano-indentation force-displacement curves of nc-Cu deposits (grain size: 56nm) and mc-Cu deposits (grain size: $2\mu\text{m}$ ). . . . .	42
2.7	Schematic illustration of the area enclosed by the load displacement curve representing the energy due to plastic deformation and elastic strains. . . . .	43
2.8	Nano-indentation force-penetration displacement curves of Cu deposits produced with different pulse frequencies for different peak current densities: (a) $I_p=0.2\text{A}/\text{cm}^2$ , and (b) $I_p=1\text{A}/\text{cm}^2$ . . . . .	46

2.9	The effect of frequency on hardness of films produced at two different current densities. . . . .	47
2.10	Effect of $t_{off}$ on the nano-hardness and grain size of Cu deposits produced at $I_p=0.2A/cm^2$ and $t_{on}=0.5ms$ : (a) Nano-indentation curve, (b) AMF image, $t_{off}=9.5ms$ , (c) AMF image, $t_{off}=14.5ms$ , and (d) AMF image, $t_{off}=19.5ms$ (scanned area = $1 \mu m^2$ ). . . . .	49
2.11	Effect of $t_{off}$ on the nano-hardness and grain size of Cu deposits produced at $I_p=1A/cm^2$ and $t_{on}=0.1ms$ : (a) Nano-indentation curve, (b) AMF image, $t_{off}=4.9ms$ , (c) AMF image, $t_{off}=9.9ms$ , and (d) AMF image, $t_{off}=14.9ms$ (scanned area = $1 \mu m^2$ ). . . . .	50
2.12	Effect of $t_{on}$ on the grain size, AFM images of Cu deposits produced at $I_p=1A/cm^2$ and $t_{off}=14.9ms$ with different $t_{on}$ : (a) 0.1ms, (b) 0.4ms, and (c) 0.6ms. . . . .	53
2.13	Effect of $t_{on}$ on the grain size, AFM images of Cu deposits produced at $I_p=0.2A/cm^2$ and $t_{off}=14.5ms$ with different $t_{on}$ : (a) 0.5ms, (b) 0.8ms, and (c) 1.0ms. . . . .	54
2.14	Effect of the grain size on nano-hardness ( $d$ , the average diameter of grains). . . . .	56
3.1	Schematic of the scratch test for the passive films on Cu coatings with in situ monitoring the contact electrical resistance (CER). . . . .	62
3.2	Dynamic polarization curves of nanocrystalline and microcrystalline Cu deposits in 1M $H_2SO_4$ (a), 3.5wt% NaCl (b) and 0.1M NaOH (c). . . . .	65

3.3	AFM images of nanocrystalline Cu deposits produced at a peak current density of $1\text{A}/\text{cm}^2$ and a current-on time of 0.1ms: (a) $t_{off}=4.9\text{ms}$ , grain diameter $D=69\text{nm}$ ; (b) $t_{off}=9.9\text{ms}$ , $D=56\text{nm}$ and (c) $t_{off}=14.9\text{ms}$ , $D=34\text{nm}$ . . . . .	66
3.4	A schematic polarization curve illustrating a few electrochemical parameters that can be determined from the polarization curve. . . . .	66
3.5	Corrosion rates of nanocrystalline and microcrystalline Cu deposits in different solutions. . . . .	70
3.6	EWFs (eV) of nanocrystalline (56nm) and microcrystalline ( $2\mu\text{m}$ ) Cu deposits after immersion in different solutions for 2 hours (X and Y are coordinate axes for the scanned area). . . . .	70
3.7	Micro-scratch tests with <i>in situ</i> monitoring changes in the contact electrical resistance (CER) with respect to the applied load: (a) nc-Cu deposit (56nm), and (b) mc-Cu deposit ( $2\mu\text{m}$ ). . . . .	73
3.8	Nyquist plane plots of the nanocrystalline (56nm) and microcrystalline ( $2\mu\text{m}$ ) Cu deposits after different periods of immersion time in 1M $\text{H}_2\text{SO}_4$ (a), 3.5wt%NaCl (b), and 0.1M NaOH (c). . . . .	76
3.9	A proposed equivalent circuit used to fit experimental EIS data for the Cu deposits-passive film impedance system. . . . .	77
3.10	Variations in the solution resistance ( $R_\Omega$ ) with the immersion time for nanocrystalline (56nm) and microcrystalline ( $2\mu\text{m}$ ) Cu deposits in different solutions, respectively. . . . .	78

3.11	Variations in the constant phase element of surface passive film ( $Q_{pf}$ ) with immersion time for nanocrystalline (56nm) and microcrystalline ( $2\mu\text{m}$ ) Cu deposits in different solutions, respectively. . . . .	79
3.12	Variations in the charge transfer resistance ( $R_{ct}$ ) with the immersion time for nanocrystalline (56nm) and microcrystalline ( $2\mu\text{m}$ ) Cu deposits in different solutions, respectively. . . . .	80
3.13	Variations in $n_d$ of the electrochemical double layer with immersion time for nanocrystalline (56nm) and microcrystalline ( $2\mu\text{m}$ ) Cu deposits in different solutions, respectively. . . . .	81
3.14	AFM morphologies of the nanocrystalline Cu deposit (56nm) in (a) 0.1M NaOH, (b) 3.5wt% NaCl and (c) 1M $\text{H}_2\text{SO}_4$ after immersion for 15 hours. . . . .	82
3.15	Cyclic voltammetries of nanocrystalline (56nm), microcrystalline ( $2\mu\text{m}$ ) Cu deposits and polycrystalline pure Cu in 0.1M NaOH solution. . . . .	83
4.1	Coefficients of friction of nc-Cu (56nm) and mc-Cu ( $2\mu\text{m}$ ) deposits with different loads, determined during micro-scratch experiments using: (a) a ball tip, and (b) a sharp tip. . . . .	90
4.2	Plots of the lateral force vs. normal force during nano-scratch as the tip was moved across the specimen surface under different applied loads, respectively: (a) nc-Cu (56nm) deposit, and (b) mc-Cu ( $2\mu\text{m}$ ) deposit. (The insets show typical AFM images of scratch tracks; the scratch length is $6\mu\text{m}$ .) . . . . .	92
4.3	EWFs of nanocrystalline (56nm) and microcrystalline ( $2\mu\text{m}$ ) Cu deposits with natural passive film. . . . .	93

4.4	Wear volume losses of nc-Cu (56nm) and mc-Cu (2 $\mu$ m) deposits determined during micro-scratch tests. . . . .	95
4.5	Local wear tests of nc-Cu (56nm) and mc-Cu (2 $\mu$ m) deposits under light loads determined during nano-scratch tests: (a) a typical image of a nano-wear track; (b) local wear volume losses.	96
5.1	A schematic illustration of the changes in current with time during electrochemical scratch. . . . .	101
5.2	Schematic illustration of electrochemical scratch system. . . . .	104
5.3	The shape of the diamond tip used in the electrochemical scratch experiment. . . . .	105
5.4	Typical cross-sectional profiles of scratched grooves on the Cu deposits and corresponding AFM image. . . . .	106
5.5	Variation in current during the electrochemical scratch (load=20g) of nanocrystalline (56nm) and microcrystalline (2 $\mu$ m) Cu deposits in 0.1 M NaOH solution. . . . .	108
5.6	The volume loss rates of the nanocrystalline (56nm) and microcrystalline (2 $\mu$ m) Cu deposits scratched at different cathodic potentials in 0.1M NaOH (a), 3.5wt% NaCl (b) and 1M H <sub>2</sub> SO <sub>4</sub> (c). . . . .	109

# CHAPTER 1

## INTRODUCTION AND LITERATURE REVIEW

### 1.1 Nanocrystalline Materials and Their Synthesis Methods

#### Definition and application

Nanostructures are generally defined based on their geometrical dimensions. A structure with two dimensions smaller than 100nm is defined as a nanostructure. An extended definition includes structures with one dimension below 100nm and a second dimension below  $1\mu\text{m}$  [3, 4].

Nanocrystalline metals and alloys with average grain sizes typically smaller than 100nm, have attracted a lot of interest for their improved mechanical, physical and chemical properties [5]. Nanostructures are metastable and could be far away from thermodynamic equilibrium. Relative to their coarse-grained counterpart (microcrystalline grains), nanocrystalline materials contain a higher fraction of grain-boundary volume, which plays a significant role in the increased physical properties of these materials [6].

Improvements in physical properties have been documented for several metallic based nanocrystalline materials. For instance, thermal sprayed nanocrystalline Ni, Inconel 718 and 316 stainless steel have been shown to be approximately 20%, 60% and 36% harder than the conventional [7]. Nanocrystalline

Ni electrodeposits exhibit drastically reduced wear rate and lower coefficient of friction as determined by dry air pin-on-disc tests, compared to conventional polycrystalline Ni. The superior mechanical properties of nanocrystalline materials have led to many industrial applications. For example, the Electrosleeve<sup>TM</sup> process for *in situ* repair of nuclear steam generator tubes by electroforming nanocrystalline Ni (100nm) on their internal wall [8]. The structural repair can be completed at site remaining the structural integrity. The high strength and good ductility of these nano materials can also minimize the impact on fluid flow and heat transfer in the steam generator. The nanocrystalline coating has been successfully applied in both Canadian CANDU and US Pressurized Water Reactors and has been regarded as a standard procedure for pressure tubing repair. The nanocrystalline material can be used in various industries and its potential impact is significant. For instance, in a single ship, there are approximately 1500 weld overlays, whose service life cycle could be considerably extended if a nanocrystalline coating, with higher hardness and wear resistance, could be used [9]. In ships, the valve stem failures due to steam erosion is a serious problem. The improved wear properties of nanocrystalline materials could be ideally suitable.

Some of the most promising industrial applications of nanocrystalline materials are use of soft magnets for high-efficiency transformers, motors, etc. The anticipated reductions in magnetocrystalline anisotropy and coercivity with reducing grain size may generate considerable development in this area [8]. In addition, nanocrystalline materials with higher density of intercrystalline defects present within the bulk [10] are ideally applied and being developed in catalytic and hydrogen applications, such as Nickel Metal Hydride battery systems and alkaline fuel cell electrodes [5]. Nanocrystalline materials have

found increasing applications in many industries.

### **Synthesis methods of nanocrystalline metallic materials**

A number of techniques have been developed to synthesize nano-particles, such as ball milling [11], severe plastic deformation [12], chemical vapor deposition [8], thermal spraying [13] and electrodeposition [8, 14, 15], etc. The formation of nanocrystalline materials during mechanical alloying of ceramics or metallic powders results from intense cold work on the ball milled powders, which are continuously fractured to achieve alloying at the atomic level. This leads to a dramatic increase in the number of imperfections (e.g., point and lattice defects), which decrease the thermodynamic stability of the starting materials. Based on the type of defects introduced, different kinds of nanocrystalline materials with different physical and mechanical properties can be obtained [11]. Thermal spraying is a coating process used to produce metallic, non-metallic and ceramic coatings in which molten or semi-molten solid particles generated from a thermal source are deposited onto a substrate by mechanical bonding. The formation of the nanostructured coating results from rapid solidification of the particulates [3]. The synthesis of nanocrystalline materials by severe plastic deformation such as in equal channel pressing is achieved by introducing defects such as dislocations and point defects. The recovery treatment of the deformed material leads to finer grains and under certain processing conditions to nanostructured materials [12]. Chemical vapor deposition (CVD) can produce deposits with nano-sized structure in a gaseous phase. Precursor gases are delivered into the reaction chamber at approximately ambient temperatures. As they pass over or come into contact with a heated substrate, they react or decompose to form a solid phase or deposit onto the substrate.

The substrate temperature is critical and can influence what reactions will take place. The size of deposits can be controlled easily by changing the pressure, the substrate temperature and the flow rate of the precursors [8].

Among various techniques, milling and co-precipitation methods are used currently to manufacture sufficiently large quantities of micrometer-sized particles with nanostructured grains. Gas condensation, crystallization of amorphous alloys, chemical precipitation, and spray conversion processing are used to synthesize three-dimensional equiaxed nanocrystallites [5]. Chemical precipitation processes including the sol-gel technique have been widely used to prepare clusters with a narrow grain size distribution. Mechanical alloying/milling techniques have been used to produce large quantities of nanocrystalline materials for possible commercial use [8]. However, some commonly used techniques for production of nanocrystalline materials have serious disadvantages. For instance, ball milling enables the production of a large amount of samples but with large lattice strain and appreciable amounts of impure products [11]; for severe plastic deformation, grain sizes smaller than 80nm are hard to obtain [16]; inert gas condensation produces nanocrystalline metals of high purity, but its production rate is very low and a very expensive apparatus is required [13]. Electrodeposition is also an effective method for the production of nanocrystalline materials. Compared to many other methods, electrodeposition is an inexpensive process and offers a simple and variable alternative to those complicated and expensive high-temperature or high-vacuum deposition processes.

## 1.2 Fabrication of nc-materials by pulse-current electrodeposition

### Advantages and basic principles of electrodeposition

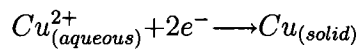
From the synthesis point of view, electrochemical synthesis is one of the oldest methods for the formation of thin films [17]. With the development of nano-technology, it has become a practical and effective way to produce nano-structured materials. Compared with the other methods cited, it offers some attractive features, such as simplicity, low cost, high production rate. Moreover, electrodeposition is generally performed near room temperature, so it can avoid the deleterious inter-diffusion contamination and dopant redistribution, which are typical of high-temperature processes. The main advantages of electrodeposition are [17, 18, 19]:

1. The possibility of growing uniform films on different substrates and over large or irregular areas from  $\text{cm}^2$  to  $\text{m}^2$ .
2. The possibility of preparing a large number of pure metals, alloys and other composites with great ease, having large grain sizes to very small grain sizes such as 10nm.
3. Little limitation to the size and shape of the nano particles formed.
4. A minimum number of technological barriers to the transfer of the technique from laboratory to industry.
5. No post processing requirements, while other methods like the sol-gel method require subsequent consolidation.
6. Versatility due to the fact that the co-deposition technology can produce a variety of novel materials such as nanocomposites.

In addition, there are a variety of electrodeposition techniques, either single or in combination with others including direct current, pulse current, reverse

pulse current, direct plus pulsed current and electroless deposition, etc. Thereinto, direct and pulse current plating have been reported to produce better quality nanocrystalline materials[17].

Figure 1.1 illustrates the basic principles of electrodeposition. Two conducting electrodes are placed in an electrolyte containing ions of the metal or metals to be deposited. When the external power supply generates a current through the cell, the metal ions are reduced to metal atoms at one of the electrodes, known as the cathode. For example, if the electrolyte contained dissolved  $\text{Cu}^{2+}$  ions, the cathode reaction would be



The cathode therefore acts as the substrate for the electrodeposited film, and is also referred to as the working electrode. To complete the circuit, an oxidation reaction takes place at the second electrode, called anode or counter-electrode [17].

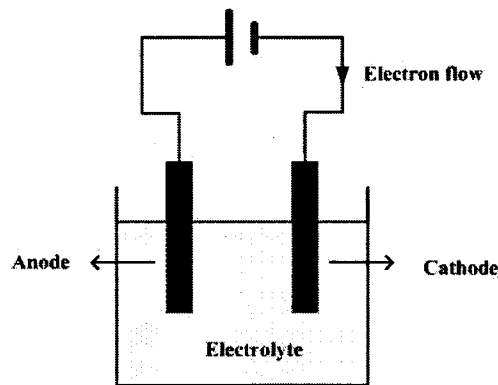


Figure 1.1: Schematic potential and electrode kinetics.

### Advantages of pulse-current electrodeposition

Pulse current (PC) electrodeposition, in which current is imposed in a periodic manner with a rectangular waveform, is a powerful means for controlling the electrocrystallization process and producing deposits with unique structure and properties. Many nanocrystalline metals, alloys and composites have been produced by pulse electrodeposition successfully [8]. Some of them have found industrial and/or commercial applications, such as nanocrystalline copper foils for printed circuit boards [8], heat exchanger repair technology [20], production of water resistant coatings [14] and electrodes for the catalysis of oxidation and evolution reaction [20], etc. Compared with direct current (DC) plating, PC electrodeposition can yield ultrafine-grained structures and a more homogeneous surface appearance of deposits with improved properties, such as the ductility and hardness [18, 19, 21, 1, 22]. More diversified microstructures can be developed, since in PC deposition one can control the microstructure and composition of deposited metals or alloys more effectively by varying the pulse frequency ( $f$ ), the pulse length-current on time ( $t_{on}$ ), the time between two pulses-current off time ( $t_{off}$ ), the peak current density ( $I_p$ ), the average current density ( $I_a$ ) and the duty cycle ( $\theta$ ). Therein,

$$I_a = \frac{I_p t_{on}}{t_{on} + t_{off}}, \quad f = \frac{1}{t_{on} + t_{off}}, \quad \theta = \frac{t_{on}}{t_{on} + t_{off}} \quad (1.1)$$

### Fundamental aspects of pulse electrodeposition

Illustration of the pulse waveform is shown in Figure 1.2. It is a typical and relatively simple waveform of pulse electrodeposition.

Pulse electrodeposition permits electrolysis with a high current density during a short period of time ( $\mu\text{s}$ - $\text{ms}$ ). The deposition of nanostructured coatings

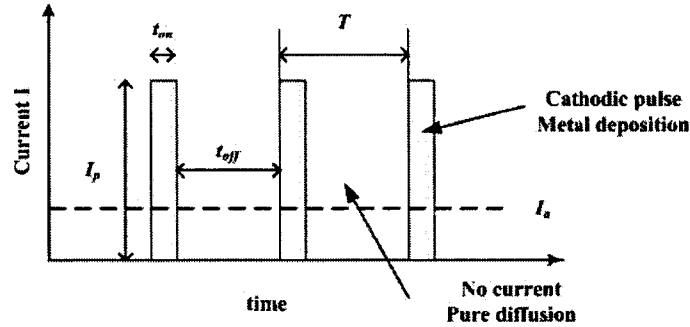


Figure 1.2: Scheme of the pulse waveform

by pulse electrodeposition depends on two fundamental processes, nucleation and growth of grains [22]. During the deposition, these two processes are in competition with each other and are influenced by many factors. Evidently, it is prone to getting ultra-fine grained deposits when the deposited ions are discharged to form new nuclei rather than incorporated into existing crystals. Therefore, factors that usually cause a high nucleation rate and slow grain growth are responsible for the formation of nano-grained deposits.

A number of factors are used as process parameters to control the electrodeposition process and to affect the mechanism of electro-crystallization, which, in turn, control the morphology, composition and mechanical properties of the deposits. These parameters can be subdivided into physical parameters and chemical parameters as described below.

### Physical parameters

The physical parameters are characteristics of the pulse current including current on time ( $t_{on}$ ), current off time ( $t_{off}$ ), peak current density ( $I_p$ ), average current density ( $I_a$ ) and duty cycle ( $\theta$ ). Changing these parameters primarily modifies the cathodic overpotential and thus influences the activation energy of nucleation ( $A_k$ ) and the nucleation rate.  $A_k$  is related to the cathodic

overpotential ( $\Delta\phi$ ) by a relation of Glasstone [23],

$$A_k \propto \left\{ \frac{1}{(\Delta\phi + [a'_{Me^+}/a_{Me^+}])^2} \right\} \quad (1.2)$$

where  $a'_{Me^+}$  is the activity of deposited ion in the electrode film and  $a_{Me^+}$  is their activity in the bulk solution. From the equation, one may see that a high cathodic overpotential can lead to a low  $A_k$ , which results in an increase in nucleation rate.

The peak current density ( $I_p$ ) and the current on time ( $t_{on}$ ) determine the number of ions that are discharged during a pulse. A high deposition rate decreases strongly the ion concentration near the cathode. The current off time ( $t_{off}$ ) controls the repletion rate. During this period, deposited ions migrate toward the electrode. Conditions under which the pulse current plating differs from the direct one (at same average current density) and their effects on the physical phenomena that govern the development of the deposit microstructure are listed in Table 1.1 [1].

### Chemical Parameters

The chemical parameters include the electrolyte composition, ion concentration and addition of complex formers or inhibitors, etc. Among them, inhibition is a key factor in the microstructural development of deposits in terms of grain size and shape. It can reduce surface diffusion by adsorbing on the metal surface by van der Waals attractions [14].

Several studies have shown that smaller grain size can be obtained by adding suitable grain refining agents to the bath [5, 14, 21, 24, 25]. Moreover, a series of fine grain sizes can be obtained by adding different amounts of additives into the bath. These additives are adsorbed on the surface but not incorporated in the deposit. The presence of adsorbed additives can shorten the

Table 1.1: Possible effects of plating parameters  $t_{on}$  and  $t_{off}$  on the deposit structure [1].

Time interval	Conditions that differ from DC plating	Phenomena affected
On-time ( $t_{on}$ )	Double layer charging Overvoltage Concentration profile near electrode Adsorption (ions, additives, hydrogen)	Nucleation rate Growth mechanism (e.g. dendrites) Electrode reaction mechanism Codeposition rate (H, alloy element) Additive reactions
Off-time ( $t_{off}$ )	Double layer discharge Potential relaxation Concentration profile relaxation Desorption (additives, ions, hydrogen)	Surface diffusion Surface recrystallization Corrosion, displacement reactions, passivation Hydrogen diffusion

mean distance for lateral diffusion of ions, which is equivalent to a decrease in the diffusion coefficient of ions. This decrease in the diffusion coefficient leads to less metal atoms reaching growth sites and the formation of new nuclei is preferred. Consequently, the nucleation rate increases, resulting in the formation of fine grains [24].

A large number of grain refiners have been recorded in the literature, for example, saccharin, coumarin, thiorea, and HCOOH have all been successfully applied to achieve grain refinement in producing nanocrystalline nickel electrodeposits [19, 24]. For Cu pulse electrodeposition, study shows that the grain size is reduced from 50 nm to 11 nm after adding citric acid to the electrolyte as shown in Figure 1.3[14]. Their effectiveness depends on surface adsorption, compatibility with the electrolyte, and temperature, etc.

#### Other parameters

Despite the physical and chemical parameters discussed above, the pH value, bath temperature and hydrodynamic conditions also have some influ-

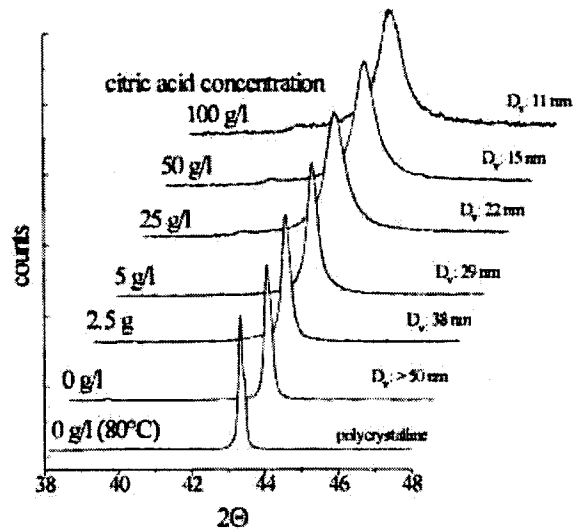


Figure 1.3: X-ray diffraction patterns (111-reflections) of nanocrystalline copper deposits prepared from electrolytes with variable citric acid content.

ences on the morphology of deposits. Studies show that increasing the temperature can accelerate the diffusion of metal ions. The consequence is the formation of coarse grains. In addition, pH value influences the grain size because the structure of the metal complex depends on PH value. For example, it is observed that in copper coatings produced by pulse plating from citric acid electrolyte, the smallest grain size of 8nm can be obtained in the pH range of 1.5-2.0, whereas the grain size goes up continuously to 100nm at pH 11.5 [22].

### 1.3 Characterization of Structure and Property

#### Methodologies for grain size calculation and morphology determination

The nanostructure of nanocrystalline coatings can be characterized using X-ray diffraction (XRD), transmission electron microscopy (TEM), scanning electron

microscopy (SEM) and scanning tunneling microscopy (STM) and atomic force microscopy (AFM), etc.

SEM, as a relatively simple and widely used technique for analyzing the microstructure of materials, is not suitable to characterize the nanostructure. It works well for characterizing the surface morphology of deposits with a relatively large grain size ( $>1\mu\text{m}$ ). An improved model field emission scanning electron microscopy (FESEM) can be used to examine the grain size and surface morphology of ultrafine-grained and nanocrystalline deposits [21, 26, 27]. TEM, with a 300,000 or higher magnification that is 100 times higher than that of SEMs or electron microscopys, is sufficient for examining the nano-scale structure and can be used to determine the grain size of nanocrystalline materials. Although it is a powerful technique, TEM still has disadvantages for routine analysis of particle sizes because: 1) the capital investment is high, 2) the sample preparation (thinning) is difficult and laborious, 3) there is a risk that the nanostructure of sample could change during the thinning process, 4) the statistical evaluation of micrographs is very time consuming[14]. Figure 1.4 shows bright field, dark field, diffraction pattern, and grain size distribution of a nanocrystalline Ni specimen produced by electrodeposition from a modified Watts bath. The average grain size of the specimen is about 25nm. Recently, the scanning tunneling microscope (STM), which can obtain atomic resolution imaging, has attracted wide attention and become popular in charactering nanocrystalline materials.

Grain size calculation is important in studying the grain size effect on material properties. One way of calculating the grain size of deposit's platelet-like morphology is to average the length, width, and thickness of each platelet observed in the images taken by SEM, TEM or AFM. However, this statis-

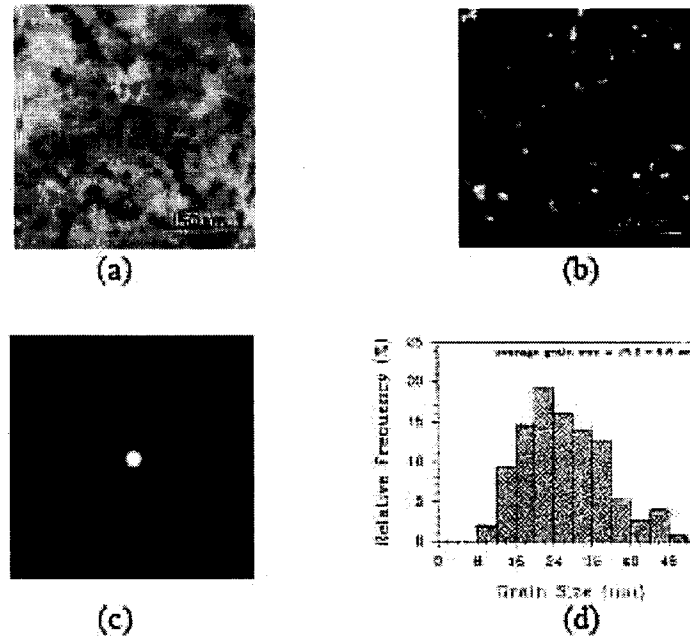


Figure 1.4: TEM micrographs of electrodeposited nanocrystalline Ni: (a) bright field, (b) dark field, (c) electron diffraction pattern, and (d) grain size distribution .

tical evaluation is time consuming and influenced by many factors. Another method, X-ray diffraction, is widely used by many researchers. Grain size and microstrain can be evaluated from peak broadening data using Scherrer's equation [28]. Theoretically, each X-ray diffraction line profile obtained in a diffractometer is broadened due to instrumental and physical (crystallite size and lattice strain) factors. So, after subtracting the instrumental broadening, the physical broadening of Bragg reflection peaks induced by small grain size and microstrain in a measured sample can be obtained [22, 25, 29]. A simple and typical process for calculating the grain size by XRD data is summarized in next chapter.

### Principle of AFM and its application in characterization of nanostructure materials

The atomic force microscopy (AFM, as shown in Figure 1.5) was an early offspring of scanning tunneling microscopy (STM) [30]. It operates by measuring attractive or repulsive forces between the sample and a probe, which is a tip at the end of a cantilever which bends in response to the force. In its repulsive contact mode, the instrument lightly touches a tip at the end of a leaf spring or cantilever to the sample. As a raster-scan drags the tip over the sample, the vertical deflection of the cantilever determine the local sample surface variation in height. Thus, in the contact mode, image is obtained by monitoring the vertical forces on the cantilever, whereas the friction mode image is derived from monitoring the lateral motions of the cantilever.

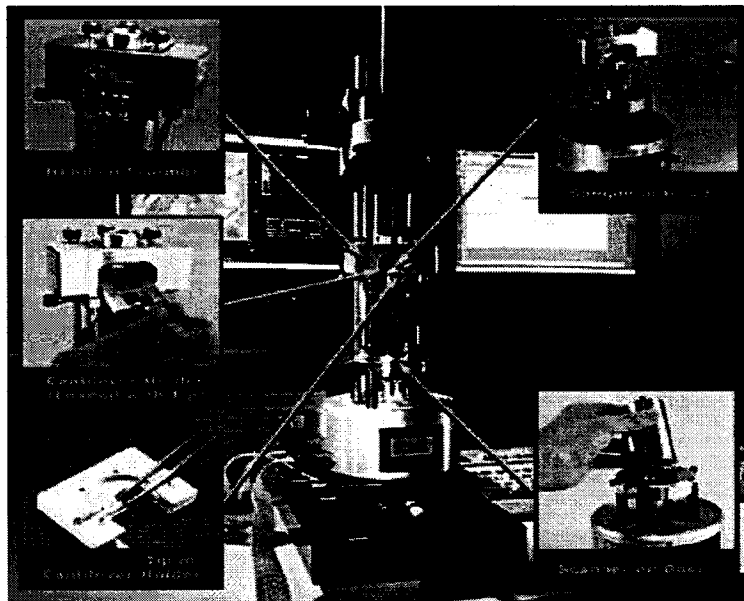


Figure 1.5: A Multi-Atomic Force Microscope (AFM).

The diagram (Figure 1.6) illustrates how AFM works; as the cantilever

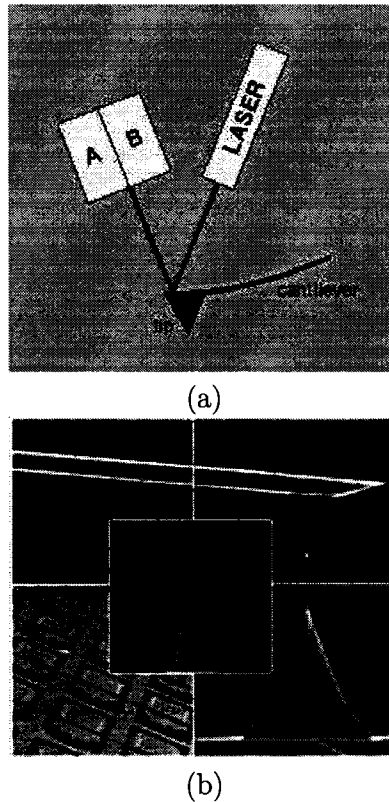


Figure 1.6: AFM tip and cantilever (a)schematic illustration, and (b)electron micrograph of a cantilevered probe

flexes, the light from the laser is reflected onto the split photo-diode. By measuring the difference signal (A-B), changes in the bending of the cantilever can be measured [31]. Since the Cantilever obeys Hooke's Law for small displacements, the interaction force between the tip and the sample can be measured. The movement of the tip or sample is tracked by an extremely precise positioning device made from piezo-electric ceramics.

The image can be obtained in several ways, such as the contact mode, tapping mode and non-contact mode [31]. The contact mode is the most common one. In this mode, the tip and sample remain in contact as the

scanning proceeds. Tapping mode is the next most common mode used in AFM. When operated in air or other gases, the cantilever is oscillated at a resonant frequency and positioned above the surface. More recently, there has been much interest in phase imaging. Non-contact mode is another one which may be employed when imaging by AFM. The cantilever must be oscillated above the surface at such a distance that we are no longer in the repulsive regime of the inter-molecular force curve. In addition, if the scanner moves the sample perpendicular to the long axis of the cantilever, friction between the tip and sample causes the cantilever to twist. Through signal separation, the AFM can distinguish the resultant left-and-right motion from the up-and-down motion of the reflected laser beam. Therefore, it can measure tip-sample friction while imaging the sample topography.

The performance of AFM and the quality of AFM images greatly depend on the operation mode and the sensor (tip) in use. In contact mode, the cantilever acts as a nanometric spring, allowing the scanning tip to measure the surface force. The sharpness of the tip is one of the most important factors influencing the resolution. Tip broadening arises when the radius of curvature of the tip is comparable with, or greater than, the size of an object for imaging.

AFM is ideal for quantitatively visualization of the surface texture for various material surfaces no matter in what environment (ambient air, vacuum or fluid) [32], as well as for measuring the dimensions of surface features. Compared to other imaging techniques, AFM exhibits appreciable advantages: nondestructive and a very high three dimension spatial resolution [33]. Nanostructured materials that are measurable using AFM include: nanocrystals, nanocomposites, nanograins, nanotubes, nanoceramics and nanopowders.

AFM can also be applied to study nano-scale tribology and measure the

surface roughness in the nanometer scale. The natural extension of the AFM for tribological studies is attributed to the motion of a nanometer-sized stylus in the AFM over a surface [31]. A major advantage of AFM for tribological studies is that the AFM can routinely be used on all types of materials including, ceramics [34], metals, polymers, semiconductors, magnetic materials and biomaterials [35]. There are a number of traditional tools for characterizing friction, wear and lubrication, such as pin-on disc, ball on flat and flat on flat in tribometer, etc. Although AFM cannot be used for large-scale tribological testing, many new applications particular at nano/micro-scales are possible:

- Surface characterization of morphology, texture and roughness.
- Measurement of the frictional force at the nanometer scale.
- Direct three-dimensional visualization of wear tracks, or scars on a surface.
- Evaluation of mechanical properties such as hardness and elasticity, and plastic deformation at the nanometer scale.

### **Nano-mechanical probe and its application**

With the increasing need for small-scale metal featuring, miniaturization of electronic components, development of nanostructured materials, thin film technology, and surface science, the quantitative study of mechanical properties of materials at nano and micrometer scales becomes more and more important. Indentation testing is a simple method that consists of touching a material of interest whose mechanical properties are unknown with the indenter whose properties are known. Recent advances in combining the mechanical probe and AFM improve the force and spatial resolutions and allow quantitative measurements of local surface mechanical properties at nanoscale contacts

[31]. The nanoindentation technique is very successful in studying local structure and mechanical property relationships. The forces involved are usually in the millinewton ( $10^{-3}\text{N}$ ) range and are measured with a resolution of a few nanonewtons ( $10^{-9}\text{N}$ ). The penetration depth is in the range from nanometers to microns with a resolution of less than a nanometer ( $10^{-9}\text{m}$ ) [36].

Figure 1.7 schematically illustrates the geometry of an indent and typical load-displacement curve of an elastic/plastic material. When an indenter penetrates into the surface, a compressively strained zone is created and surrounded by an elastically constrained region. As a result, a complex stress-strain state is developed around the contact area. The related load-displacement curve of indentation, describes both elastic and plastic properties of the sample in the vicinity of the indenter.

The mean contact pressure  $P_m$ , and hence, indentation hardness  $H$ , is given by the indenter load  $P$  divided by the contact area  $A$  [36]. The area of contact can be calculated from the known geometry of the indenter and value of  $h_p$  (see Figure 1.7).

$$H = P_m = \frac{P}{A} \quad (1.3)$$

In practice, the nano-indentation test can be performed on a wide variety of substances, such as microelectronic integrated circuits, thin films for disc, capacitors, soft polymer and passivation layers, etc. The shape of the load-displacement curve is often found to be a rich source of information, not only providing a means to calculate modulus and hardness of the specimen, but also for the identification of non-linear events such as phase transformation, crack propagation, fracture toughness of brittle material and delamination of films, etc [36]. The mechanical probe in combination with AFM allows precise

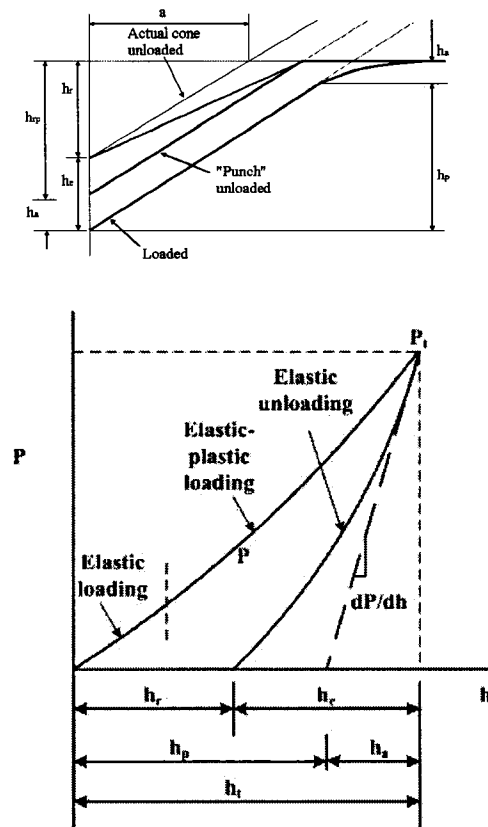


Figure 1.7: Schematic of indent and compliance curve (load vs displacement) for an elastic-plastic specimen, loading and unloading, from a nanoindentation experiment with maximum load  $P_t$  and depth beneath the specimen free surface  $h_t$ . The depth of the contact circle  $p$  and slope of the elastic unloading  $dp/dh$  allow specimen modulus and hardness to be calculated.  $h_r$  is the depth of the residual impression, and  $h_e$  is the displacement associated with the elastic recovery during unloading.

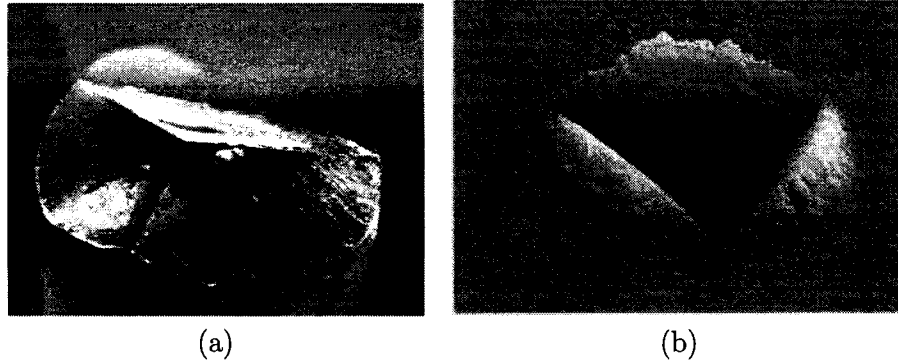


Figure 1.8: (a) Electron micrograph of a Berkovich tip and (b) an AFM contact mode image of a nano-dent.

micro/nanoindentation test and micro/nanoscratch with *in situ* high resolution surface imaging. Figure 1.8 shows the geometry of a Berkovich tip, which is widely used as a standard for nanoindentation and an AFM image of a nano dent.

### Electron work function

The electron work function (EWF) refers to the minimum energy required to remove an electron from the interior of a solid. In general, the EWF is expressed as:

$$\varphi = E_0 - E_F \quad (1.4)$$

where  $E_0$  is the energy of electron at infinity and  $E_F$  is the Fermi energy. The value of  $\varphi$  is approximately the depth of the potential well or the work required to move a electron from the highest electron state of a metal to infinity [33, 37].

The EWF depends on surface physical and chemical properties and environmental conditions as well [38]. The electron work function is a fundamental characteristic of solids in the condensed metallic state and it can be used as

a parameter for surface characterization [39, 40]. As the electron has to move through the surface region, its energy is influenced by the optical, electric and mechanical characteristics of the region. Hence, EWF is a sensitive indicator of surface condition and is affected by absorbed or evaporated layers, surface reconstruction, surface charging, oxide layer imperfections, surface and bulk contamination, etc [41, 42, 43].

The electron work function can be determined by direct or indirect techniques. The direct techniques are based on the electron emission from a metal. Depending on the external excitations, these techniques are subdivided into thermoemission, photoemission and exoelectronic emission [44]. Indirect work function measuring techniques are based on the behavior of an electron beam (or other charged particles) near the surface and the contact potential difference (CPD) [45].

As a very sensitive parameter to surface changes, EWF has found increasing applications in tribological, corrosion, wear and surface science field [44, 46, 47]. Recent studies show that EWF can be applied to study the history prior to wear and the onset of wear [48] as well as to investigate the electrochemical stability of passive films formed on metal surface [49]. EWF has been found to have strong relationships with adhesion [50], deformation [51], dislocation [47] and surface roughness [52], etc. It is also interesting to study the relationship between EWF and electrochemical parameters so that we may better understand the surface property of metals and the effects of microstructure on corrosion and wear. Such study can benefit the investigation and prediction of the behavior of a particular microstructure, such as a nanostructure.

#### 1.4 Properties of nanocrystalline Metals and Alloys

The high density of grain boundaries in nanocrystalline materials give rise to a variety of properties that are different from those of the conventional materials. Enhanced strength or micro-hardness, higher diffusivity, improved ductility/toughness, reduced density, reduced modulus of elasticity, higher electrical resistivity, increased specific heat, higher thermal expansion coefficient, superior soft properties, better adhesion properties are commonly cited properties, which are strongly dependent on the grain size [5]. Another group of properties, including bulk density, thermal expansion and Young's modulus, are little affected by grain size [8]. In the following sections, some mechanical, tribological and electrochemical and magnetic properties are discussed in more detail.

#### Mechanical properties

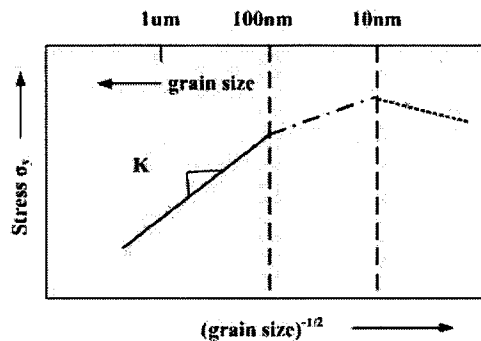


Figure 1.9: Schematic representation of the variation in yield stress as a function of grain size in microcrystalline and nanocrystalline metals and alloys [2].

As a powerful tool to modify material properties and performance, grain refinement has long been the focus of metallurgical research. It has been found

that nanocrystalline materials possess some appealing mechanical properties, such as high strength, decreased toughness, increased strength, higher ductility at high strain rate, and the potential for enhanced superplastic deformation at lower temperatures and higher strain rates [2]. For example, the variation in stress as a function of grain size from micro-scale to nano-scale is schematically shown in Figure 1.9. In many microcrystalline and ultra-fine-crystalline metals and alloys, strengthening with grain refinement can be represented by the well-known Hall-Petch mechanism, which describes the relationship between yield strength  $\sigma_y$ , and grain size  $d$ .

$$\sigma_y = \sigma_0 + Kd^{-1/2} \quad (1.5)$$

where,  $\sigma_0$  and  $K$  are material constants. During plastic deformation, grain boundaries block the motion of dislocations. Large-angle grain boundaries can block the movement of dislocations more effectively. As a result, the grain refinement can lead to an enhanced resistance to plastic flow, thus increasing the material's strength. As the microstructure is refined from the micro regime to the nano regime, the stress versus grain size relationship departs from that described by the Hall-Petch equation [2]. The decrease in the efficiency of strengthening can be attributed to the grain boundary sliding associating with stress relief when the grain size is reduced to the nanoscale. Therefore, the grain boundary can strengthen a material by impeding dislocation but may also soften a material with the grain size is reduced to the nanoscale when grain boundary sliding occurs. When grains are extremely small, the balance between hardening and sliding could lean to the latter [53]. With further decreasing of grain size below the order of 10nm or so, grain refinement can cause weakening of the metal [54].

However, there are still some properties that are not as expected. For example, with high diffusivity and nanometer grain size, nanocrystalline materials are expected to creep at room temperature. But experimental results have shown that this is not the case. The creep rate of nanocrystalline Cu is of the same order of magnitude as that of microcrystalline one, and three orders of magnitude lower than that predicted by the Coble creep model [55]. Some researchers attribute these to the low-angle grain boundaries and the presence of twinning structure, which do not promote vacancy diffusion and resist grain boundary sliding [55].

Additionally, the following phenomena have been observed with nanocrystalline materials produced by pulse electrodeposition: 1) the deposits produced by pulse-current electrodeposition are found to be significantly harder than those made by direct-current electrodeposition, which is related to the changes in grain size, internal stress and porosity; 2) for nanocrystalline deposits produced by pulse plating, the hardness increases with a decrease in the grain size. However, for very small grains ( $<20\text{nm}$ ), with a further decrease in grain size, a reduction in hardness is observed, known as the Inverse Hall-Petch Relationship [19]; 3) annealing (recovery) a sample yields higher hardness values than as-deposited samples [19]. The annealing treatment may minimize the interfacial strain energy by adjusting the crystallographic orientation. The resultant sharper grain boundaries with a high density can block dislocations more effectively [53]. As a result, higher hardness is obtained by annealing (recovery).

### **Tribological properties**

Nanocrystalline materials are expected to exhibit increased resistance to tribological and environmental-assisted damage due to the improved strength. Studies have shown that the coefficient of friction (COF) of nanocrystalline nickel produced by pulse plating was almost half that of polycrystalline nickel. Higher hardness and smoother surface of nanocrystalline Ni could be the main reason for their lower value of COF [24]. Recent study has also demonstrated that the wear resistance of surface nanocrystallized aluminum layer produced by sandblasting and annealing is considerably higher than that of coarse-grained aluminium and exhibits lower friction coefficient and adhesion force [53]. In general, research in this field is still scarce, and how the nanostructure influences the adhesion force and contact area is not well clarified.

### **Corrosion behavior**

The corrosion resistance of nanocrystalline materials in aqueous solution is of great importance to the assessment of nanocrystalline structures for potential applications. It is well known that corrosion is strongly influenced by microstructure [56]. Nanocrystalline materials with a higher density of grain boundaries, which render electrons more active, should exhibit different electrochemical properties, compared to microcrystalline ones. However, to date, research on corrosion and corrosive wear of nanocrystalline materials is insufficient and reported experimental results are not always consistent: both beneficial and detrimental effects of nanostructure on corrosion were observed [5].

Rofagha.R [57] observed that the passive current density of nanocrystalline Ni was higher than polycrystalline nickel in acidic, alkaline and neutral solu-

tions. He concluded that this was attributed to the high surface fraction of grain boundaries and triple junctions in nanocrystalline nickel. There was no difference in corrosion current density at high anodic overpotential but conventional polycrystalline Ni was more susceptible to localized corrosion. Reduced corrosion resistance was also observed for nanostructured  $\text{Cu}_{90}\text{Ni}_{10}$  alloy [58]. However, P.S. Fedkiw [21] compared the corrosion behavior of nanocrystalline Zn deposits with that of Engineering-Galvanized (EG) steel samples and suggested that although the corrosion potential of EG steel was more positive than that of nc Zn, the Zn sample had a more protective film than that of EG steel. As a result, the nanocrystalline Zn deposits showed lower corrosion rate than EG steel. Enhanced corrosion resistance of nc-Fe8Al in  $\text{Na}_2\text{SO}_4$  solution was also reported, which may be attributed to fast diffusion of Al along grain boundaries, leading to a protective oxide film [59]. It has been demonstrated that electrodeposited nanostructured Ni with a grain size of 100nm is intrinsically resistant to intergranular attack and intergranular stress corrosion cracking. Excellent resistance of the nanocrystalline nickel to alkaline environments and reducing acidic environments has also been reported [8].

Due to the discrepancy among the reported experimental observations, how a nanocrystalline structure really influences the electrochemical properties need to be clarified.

### **Electrical and magnetic properties**

A comparison of results from electrical property measurements for nanostructured materials produced by different synthesis routes (e.g., gas condensation, electrodeposition) has shown similar trends. In most cases, the electrical resistivity increases with decreasing grain size, similar to the situation of elec-

trodeposited Ni [5]. This can be attributed to electron scattering at defects, such as grain boundaries and triple junctions. For electrodeposited Cu, it has been reported that no effect of grain size on electrical transport properties was observed [8].

### 1.5 Objectives of This Study

Although pulse current electrodeposition is one of the most effective methods to produce nanocrystalline materials, the properties of such fabricated nanocrystalline electrodeposits have not been well understood compared to those made by CVP or condensation method [8]. Especially, the corrosion resistance and tribological properties of nanocrystalline electrodeposits need to be systematically evaluated, since this is of great importance to a wide range of potential industrial applications of nano-deposits. Previously reported studies are not always consistent.

The objective of the present study is to investigate the tribological, electrochemical and mechanical properties of nanocrystalline Cu deposits produced by pulse current electrodeposition in comparison with the microcrystalline one produced by direct current electrodeposition. Another task is to correlate changes in the properties to the nano grain size. This study also includes investigating how the nanocrystalline structure influences the electrochemical behavior and the synergism of electrochemical and mechanical attack during corrosive wear.

Copper is one of metals most extensively used in industry. In view of its applications as an interconnect material in microelectronic devices as well as its wide applications in the integrated circuit industry, copper was chosen as a sample material for this study. Copper is also the most important coating

material for interior drinking water systems [60]. In addition, copper deposits have found applications in nickel and chromium plating as an undercoat [61]. Electrodeposited copper has been widely investigated regarding their morphological characteristics, electrical properties and corrosion resistance. With the rapid development of nano-technology, nano-tribology becomes more and more important to devices on nanoscale such as Micro-Electro-Mechanical-System (MEMS), Nano-Electron-Mechanical-System (NEMS) and magnetic storage peripherals [36, 31]. However, research in properties of nanocrystalline Cu deposits is still scarce. In particular, few studies have addressed the tribological and electrochemical issues, which are therefore the important tasks of this study.

## CHAPTER 2

### PROCESSING STUDY AND MECHANICAL PROPERTY

#### 2.1 Introduction

It has been found that nanocrystalline materials exhibit superior mechanical properties due to their ultrafine-grains and high volume fraction of grain boundaries. Following the pioneer work of Hall and Petch [62, 63], the relationship between the grain size and mechanical properties has been a subject of continuous investigation. Copper is a widely used metal in industry. Due to its attractive mechanical and physical properties, copper coated rolls have been used in the printing industry and copper coatings are extensively used as an interconnect material in microelectronic devices. Recently, the study of nanocrystalline copper has attracted increasing attention. Bandyopadhyay and Chakravoty [64] produced copper particles of sizes in the range from 3.1nm to 11.4nm using an electrodeposition process. Qian et al.[65] studied a series of nanocrystalline Cu samples with different microstrains but the same grain size, which were obtained by annealing a magnetron-sputtered Cu specimens, and demonstrated that the thermal expansion coefficient of crystalline lattice increases with increasing microstrain. Lu et al.[66] investigated the grain growth and strain releasing processes in electrodeposited nanocrystalline Cu

specimens and found that the grain growth started at about 75°C at which the microstrain in the (111) plane began to be released, while the mean microstrain in (100) plane began to be released at a higher temperature of 150°C. Chang and co-workers [67] investigated the deformation behavior of electrolessly deposited nanocrystalline copper films with a grain size of about 10nm using instrumented nanoindentation and observed that their hardness, shear stress for yielding, and energy release rate were lower than those of electroplated copper films with a larger grain size. They attributed these to the dominant deformation mechanism of grain-boundary sliding and grain rotation instead of dislocation movement. Youssef and co-workers [68] reported a unique way of producing artifact-free nanocrystalline Cu (23nm) with a narrow grain size distribution using mechanical milling/ *in situ* consolidation at both liquid-nitrogen and room temperature; their nanocrystalline Cu showed an extraordinarily high yield strength (770 MPa), along with good ductility (equivalent to %*EL*=30%).

The study reported in this chapter is focused on the synthesis of nanocrystalline copper in a sulphate solution and evaluation of its mechanical properties. Nanocrystalline and microcrystalline copper deposits were produced by pulse and direct current electrodeposition processes, respectively. The grain size of nanocrystalline deposits was determined using both X-ray Diffraction technique and Atomic Force Microscopy (AFM). PC-electrodeposition is a powerful means for producing ultrafine-grained structures because a higher instantaneous current density can be obtained. It is essential to explore influences of pulse electrodeposition parameters, such as the peak current density ( $I_P$ , frequency( $f$ ), current-on time ( $t_{on}$ ) and current-off time ( $t_{off}$ ) on the grain size and mechanical properties of the deposits. Therefore, the goal of the study

reported in this chapter is to produce nanocrystalline copper, to investigate the effects of pulse electrodeposition parameters on the grain size and surface morphology and the effect of the grain sizes on mechanical properties of nanocrystalline copper, including nano-hardness and the ratio of the recoverable energy to the total energy during deformation. The deviation from the Hall-Petch relation caused by nanostructure is also investigated.

## 2.2 Specimen Preparation

Nanocrystalline (nc-) and microcrystalline (mc-) copper deposits were produced by pulse current and direct current electrodeposition processes, respectively, in a copper sulfate electrolyte with thiourea as additive. The chemical composition of two electrolytes and corresponding deposition parameters are listed in Table 2.1. Brass was used as the substrate after polishing, followed by weak and strong pickling in 3% and 25%  $\text{H}_2\text{SO}_4$  solutions, respectively. Pickling was necessary to activate the substrate and enhance the adhesion of deposits. The counter electrode was pure copper, which helped to maintain the copper ion concentration in the electrolyte. After electrodeposition, the copper deposits were rinsed in de-ionized water and dried immediately. The deposits were slightly polished with  $0.05\mu\text{m}$  alumina powder and lightly etched using dilute  $\text{FeCl}_3+\text{HCl}$  solution before evaluating their properties. The thickness of the deposits was about  $15\mu\text{m}$  estimated based on the weight gain of the brass electrode as well as cross-sectional microscopic observation. The roughness of the deposits was  $15\pm 3\text{nm}$ .

Grain size of the nanocrystalline deposits was determined by both the X-ray diffraction peak broadening analysis and atomic force microscopic examination (AFM, manufactured by Digital Instrument, Santa Barbara, CA, USA). X-ray

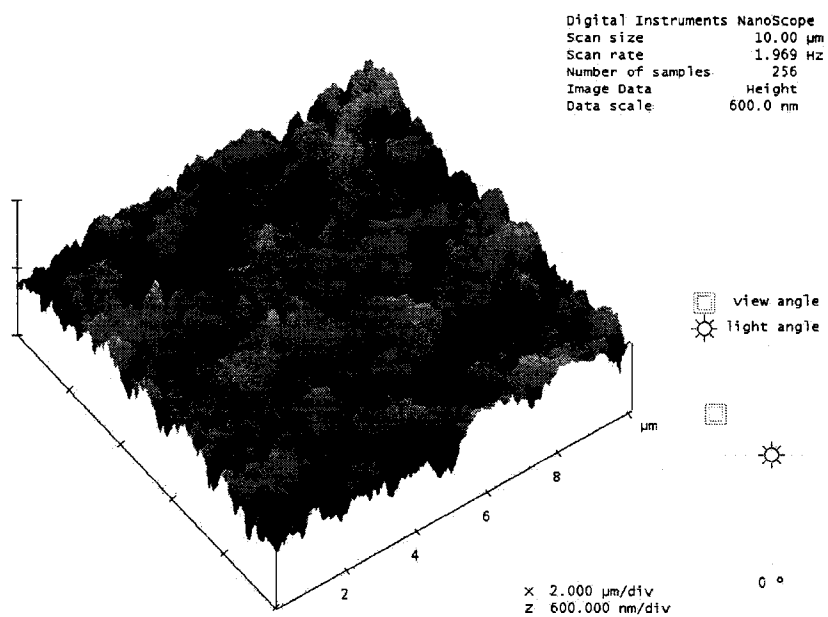
Table 2.1: Electrolytes and deposition parameters for Cu deposition.

Constituents	PC-plating bath	DC-plating bath
CuSO <sub>4</sub> ·5H <sub>2</sub> O	0.15M	0.6M
H <sub>2</sub> SO <sub>4</sub>	0.184M	0.46M
Thiourea	0.05gl <sup>-1</sup>	0.05gl <sup>-1</sup>
Deposition parameters	$I_p=1\text{A cm}^{-2}$ $t_{on}=0.1\text{ms}$ $t_{off}=9.9\text{ms}$ $f=100\text{Hz}$ $I_a=10\text{mA cm}^{-2}$	$I=10\text{mA cm}^{-2}$

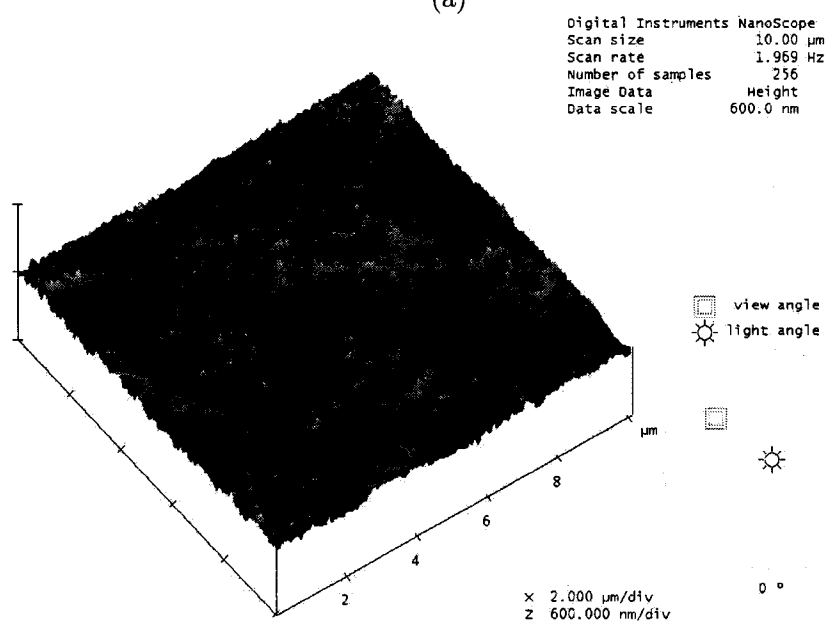
diffraction analysis was carried out using a Rigaku Geigerflex Power Diffractometer with a Co tube and a graphite monochromator. Each diffraction peak profile was obtained at a slow scan rate of 0.002°/sec. The full-width at half-maximum intensity (FWHM) of the XRD peaks was analyzed using a software package, JADE 6.0, installed in the diffractometer. Pearson VII function, a combination of Cauchy and Gaussian functions, was used to separate  $K_{\alpha 1}$  and  $K_{\alpha 2}$ . The surface morphology of deposits was characterized by AFM technique in both friction and contact modes of scanning. A 200- $\mu\text{m}$ -long narrow silicon nitride probe with a spring constant of 0.06 N/m was used. The probe consisted of a cantilever with an ultra sharp tip at the end. The height of the tip was about 10 $\mu\text{m}$ .

### 2.3 Surface Morphology

Figure 2.1 shows AFM images of as-deposited Cu deposits produced by PC and DC electrodeposition processes, respectively. Surface smoothness of the deposits was determined by measuring their root-mean-square (RMS) rough-



(a)



(b)

Figure 2.1: AFM images of as-deposited Cu deposits produced using different electrodeposition methods: (a) DC, and (b) PC (scanned area =  $10 \times 10 \mu\text{m}^2$ ).

ness derived from the AFM images of a scanning area ( $10 \times 10 \mu\text{m}^2$ ). RMS roughness represents the standard deviation of the profile heights [69]. For example, the RMS roughness for two-dimensional profile can be expressed by

$$RMS = \sqrt{\frac{1}{n} \sum_{i=1}^n (Z_i - \bar{Z})^2} \quad (2.1)$$

where,  $\bar{Z}$  is the average profile height and  $Z_i$  is the profile height at position  $i$ .

As shown in Figure 2.1, RMS roughness value of the as-deposited DC-plated Cu thin film was  $98 \pm 10 \text{nm}$ , much higher than that of the PC-plated one that was  $26 \pm 5 \text{nm}$ .

The pulse current electrodeposit was more uniform and smoother than the direct current plated one due to the higher instantaneous current density by pulse control. How the surface roughness changes with current is schematically shown in Figure 2.2. As shown in Figure 2.2, at a low current density, the number of metal ion discharge event per unit area was shown to be small. Because the metal discharge occurs preferentially at protrusions, deposits are produced with a high-density surface of irregularities at low current densities. At high current densities, there is a high density of metals ions and electrons on the cathode surface. Similarly charged particles repel each other if they are brought closer than a critical distance from each other. A high density of metal ions and electrons generated at high current densities will be distributed over the surface according to the magnitude of their repulsive force [70]. As a result, the discharge sites are more uniformly distributed making the surface smoother. The distribution of current densities over the cathode surface is one important cause of surface roughness in electrodeposited films. It can be concluded that surface roughness becomes smaller at higher current density.

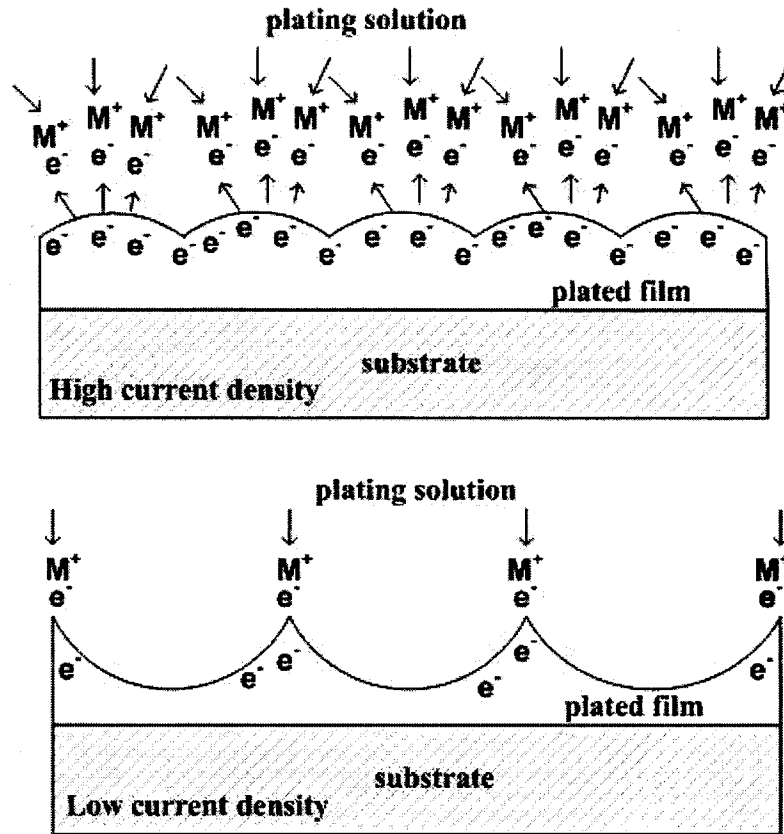
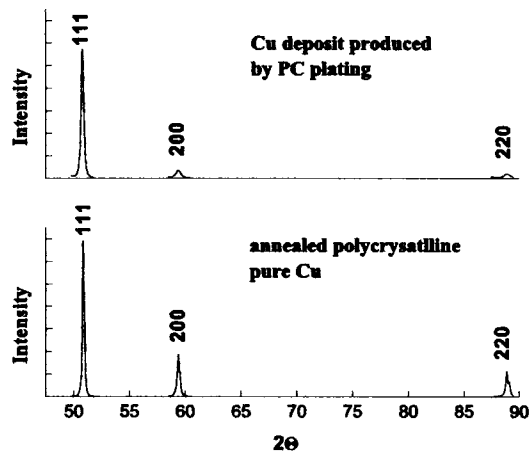


Figure 2.2: A schematic illustration illustrating how a change in current density affects the surface irregularity of plated films.

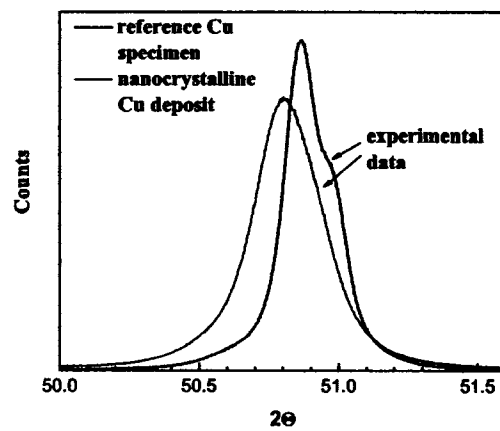
Taking into account that the performance of a material is affected by its surface roughness, the as-deposited coatings were therefore slightly polished and lightly etched to minimize the roughness influence on property measurement. The final surfaces for testing had similar RMS roughness of  $15 \pm 3 \text{ nm}$ .

## 2.4 Grain Size Determination

In the present study, both the XRD technique and AFM were used to determine the grain size and to validate each other. Figure 2.3 shows an X-ray



(a)



(b)

Figure 2.3: X-ray diffraction patterns of a PC-plated Cu deposit and an annealed sample of pure Cu:(a) (111), (200) and (220) peaks, and (b) magnified (111) peaks for grain-size analysis.

diffraction pattern of PC-plated Cu thin film. Theoretically, each X-ray diffraction peak profile obtained is broadened by instrumental and physical factors. So after subtracting the instrumental broadening, the physical broadening of each Bragg reflection peak caused by small grain size or microstrain can be obtained. The grain sizes of nanocrystalline Cu deposits were estimated by applying well-known Scherrer Formula [28] for the (111) peak. The peak position, full-width at half-maximum intensity (FWHM) and integral width of the XRD peaks were analyzed using a software package JADE 6.0, installed in the Rigaku Geigerflex2173 diffractometer. An annealed pure copper sample was used as a reference sample to get rid of the instrumental broadening and to determine the broadening caused by nanocrystallization.

$$D = \frac{0.9\lambda}{\delta(2\theta) \cos \theta} \quad (2.2)$$

Where,  $D$  is the mean dimension of the crystallites and  $\lambda$  is the X-ray wavelength. The instrumental broadening-corrected pure line profile breadth  $\delta(2\theta)$ :

$$\delta(2\theta) = B\left(1 - \frac{b^2}{B^2}\right) \quad (2.3)$$

$B$  and  $b$  are the full width at half maximum (FWHM) of the same Bragg peaks from the experimental and reference samples, respectively, obtained after  $CoK_{\alpha 2}$  stripping and  $CoK_{\alpha 1}$  fitting. The separation of the two reflections was carried out by a computerized XRD analysis system.

The (111) peak profiles are magnified and shown in Figure 2.3(b). The grain size calculated using (111) diffraction was 58nm. It does not take into account the additional line broadening caused by microstrain, which is acceptable if the broadening caused by reduction of grain size is large. In order to verify

the XRD result, the grain size of the nanocrystalline deposit was also directly examined using AFM. Figure 2.4 shows an AFM image (friction mode) of a Cu deposit produced by PC electrodeposition. The scanning area was  $1 \times 1 \mu\text{m}^2$ . The friction-mode image is obtained from monitoring the lateral motions of the cantilever [31]. It appears that the friction mode provided higher resolution than the contact mode in determination of the nano-grain size. From Figure 2.4, the average size is about 56nm, which is in good agreement with the XRD result. XRD tests is based on the theory that when X-ray radiation passes through matter, the radiation interacts with the electrons in atoms, result in scattering of the radiation [28]. If the atoms are organized in planes and distances between the atoms are of the same magnitude as the wavelength of the X-rays, constructive and destructive interference will occur. This result in diffraction where X-ray are emitted at characteristic angles based on the spaces between planes, indicating the grain size calculated from XRD technique represents the vertical dimension of the grain. However, AFM is applied to determine the size of the grains in the nanocrystalline surface layer (cross-section), so the grain size obtained from AFM observation denotes the lateral dimension of the grain. Therefore, grains in nc-Cu deposits produced by PC-electrodeposition exhibited sphere shape.

The XRD peak broadening method for calculating grain size using Scherrer Formula is acceptable for nanocrystalline materials with grain size smaller than 100nm [29]. For comparison, the average grain size of microcrystalline Cu deposits produced by DC electrodeposition was determined using an optical microscope, which was about  $2 \mu\text{m}$  as shown in Figure 2.5.

Comparing the PC and DC electrodeposition methods, the pulse plating is effective for the refinement of grains. It is well known that overpotential

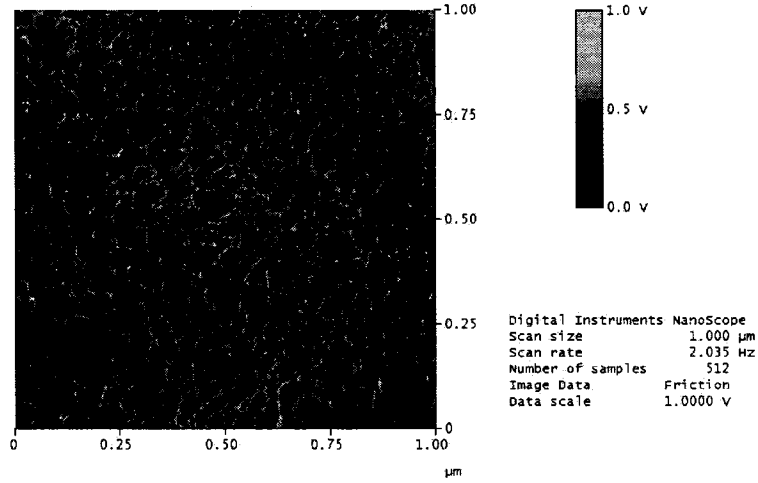


Figure 2.4: AFM image of a nanocrystalline Cu deposit produced by PC electrodeposition (friction mode).

increases linearly with logarithmic current following the Tafel relation [71],

$$\Delta\phi = a + b \log i \quad (2.4)$$

where,  $a$  and  $b$  are constants and  $i$  is the current density. The larger the current density, the higher is the overpotential. According to electrocrystallization theory [23], the high cathodic overpotential decreases the activation energy of nucleation, resulting in an increased nucleation rate as Equation (1.2). According to the classical theories on electrochemical phase formation and growth, the two dimensional (2D) nucleation rate,  $r_n$  is given by [23]

$$r_n = K_1 \exp \frac{-bs\varepsilon^2}{ZekT\Delta\phi} \quad (2.5)$$

where,  $K_1$  is the rate constant,  $b$  is the geometric factor depending on the shape of the 2D grains,  $s$  is the area occupied by one atom on the surface of the grain,  $\varepsilon$  is the specific edge energy,  $Z$  is the electron charge of the ion,

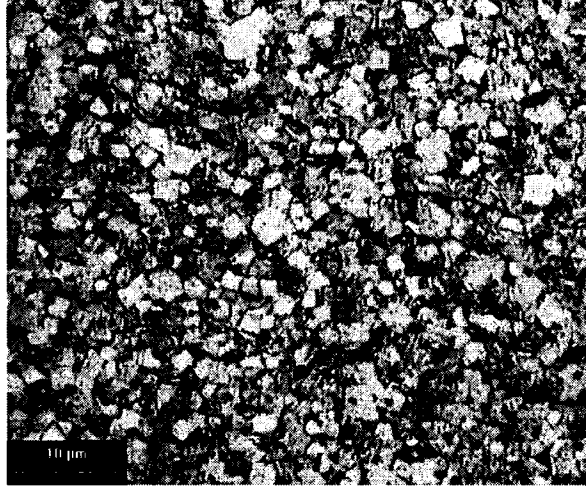


Figure 2.5: Optical microscopic image of a microcrystalline Cu deposit produced by DC electrodeposition.

$e$  is the charge of the electron,  $k$  is the Boltzmann constant and  $\Delta\phi$  is the overpotential. The overpotential is determined as expressed in Equation (2.4). Thus, the nucleation rate increased (see Equation (2.5)), leading to a more homogeneous structure and finer crystal grains.

Moreover, when the nucleation dominates the deposition process with a large number of nuclei generated on the substrate, the growth of nuclei and crystallites is strongly impeded. As a result, the electrodeposition of nanocrystalline deposits could be realized by the use of high current densities. Such high currents corresponding to high voltages are not conceivable in DC-plating because of limitation in the material transport and the massive evolution of hydrogen. In pulsed electrodeposition the peak current density can be very high during a very short on-time although the average current density is the same as that for a DC-plating process.  $I_p$  and  $t_{on}$  determine the number of atoms that are deposited on the substrate during a pulse, including atoms for generating nuclei and those incorporated into the existing crystals. The high

deposition rate largely decreases the ion concentration near the cathode. In addition, during  $t_{off}$ , Cu ions migrate into the depleted vicinity of the cathode. Longer  $t_{off}$  can stabilize the existing fine grains and replenish sufficient ions to deplete at the cathode in the next pulse period. However, there is a risk that the grains may grow during the relaxation time. More discussions on this issue are given in the following sections.

## 2.5 Mechanical Property

Mechanical properties of the deposits were evaluated using a Triboscope (made by Hysitron, Minneapolis, MN, USA), a combination of a nano-mechanical probe and AFM. The probe was a three-sided pyramidal Berkovich indenter made of diamond. The angle between two faces of the tip is 142.3 degrees. Force-displacement curves of the indentation are recorded during the test. Indentation loads of 50 and 100  $\mu\text{N}$  were used. Hardness and elastic behavior of the deposit were evaluated from the force-displacement curves and the results presented in this thesis are values averaged over more than ten indentation tests.

Table 2.2: Mechanical properties of nc- and mc-Cu deposits determined by nano-indentation under 50 and 100  $\mu\text{N}$ .

Materials	Grain size(nm)	Force ( $\mu\text{N}$ )	Maximum depth(nm)	Hardness (GPa)	$\eta = W_r/W_t$ (%)
nc-Cu	56	50	6.6 $\pm$ 0.3	4.86 $\pm$ 0.24	45.0 $\pm$ 4.2
		100	11.6 $\pm$ 0.4	4.96 $\pm$ 0.21	35.5 $\pm$ 3.8
mc-Cu	2000	50	25.6 $\pm$ 0.4	1.22 $\pm$ 0.13	24.0 $\pm$ 3.3
		100	48.2 $\pm$ 0.4	1.11 $\pm$ 0.14	18.7 $\pm$ 4.0

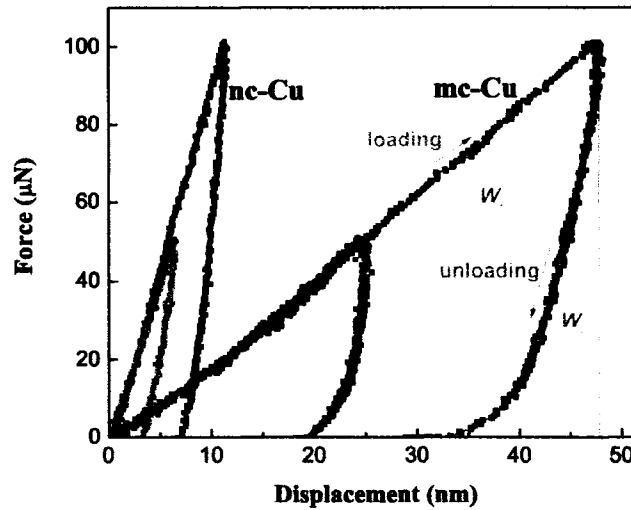


Figure 2.6: Nano-indentation force-displacement curves of nc-Cu deposits (grain size: 56nm) and mc-Cu deposits (grain size:  $2\mu\text{m}$ ).

Nano-indentation tests were performed to evaluate mechanical properties of the deposits. Figure 2.6 shows force-displacement curves of the nanocrystalline and microcrystalline Cu deposits. The applied loads of 50 and  $100\mu\text{N}$  were low enough to make penetration depths much less than the required 10% of the film thickness so as to avoid influence of the substrate on the hardness measurement [36]. The penetration depth, nano-hardness and the ratio of recoverable deformation energy to total deformation energy ( $\eta$ ) were determined and are listed in Table 2.2. In principle, under a given load, the smaller the penetration depth, the harder is the material. The  $\eta$  value reflects the elastic behavior of a material, indicating the contribution of elastic work to the total work during deformation. The area under the loading curve represents the total deformation energy ( $W_t$ ), which includes the total energy consumed dur-

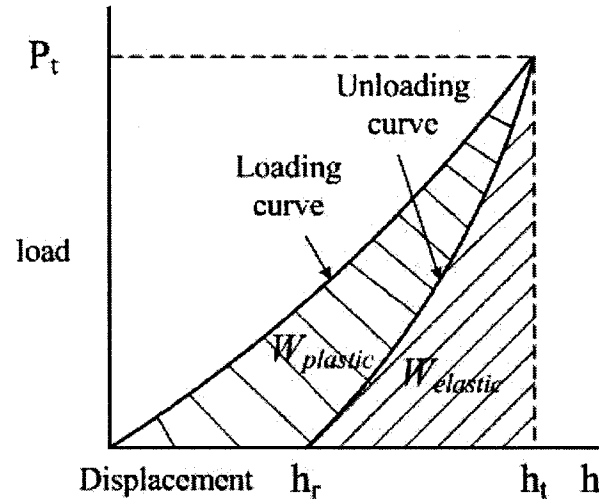


Figure 2.7: Schematic illustration of the area enclosed by the load displacement curve representing the energy due to plastic deformation and elastic strains.

ing the indentation process, and the area under the unloading curve denotes the recoverable energy ( $W_r$ ), namely the energy associated with the elastic deformation (see Figure 2.7). Defined as the contact pressure, the indentation hardness is equal to the applied load divided by the contact area, which can be estimated from the depth of penetration with the known geometry of the indenter [36]. The nano-indentation tests demonstrated that the nanocrystalline deposit had smaller penetration depth, higher hardness and  $\eta$  value. The grain size is a major parameter affecting the grain boundary hardening. Based on the Hall-Petch relationship, nanocrystalline materials are expected to exhibit higher strength than their microcrystalline counterpart. In this case, the decrease of grain size from  $2\mu\text{m}$  to  $56\text{nm}$  lead to an increase in hardness almost by a factor of 4 (see Table 2.2). According to the strengthening mechanism, the increase in hardness can be attributed to an increased density of grain boundaries in nanocrystalline materials, which helps to block the dislocation

motion, thus enhancing the resistance to plastic deformation. Palumbo [10] showed that the volume fraction of grain boundary could be as high as 50% for grains smaller than 5nm in diameter, 10% for grains around 50nm, and lower than 1% when the grain size is  $1\mu\text{m}$ . In addition, the increased strength extends the elastic deformation range, leading to higher  $\eta$  values. It should be noted that when the grain size is smaller than 10nm or so, the grain refinement may cause softening of nanocrystalline metals [2]. In the present study, the nano-grain size did not get into that range.

## 2.6 Grain Size Control and Processing Parameters

### Effect of frequency and peak current density on grain size and hardness

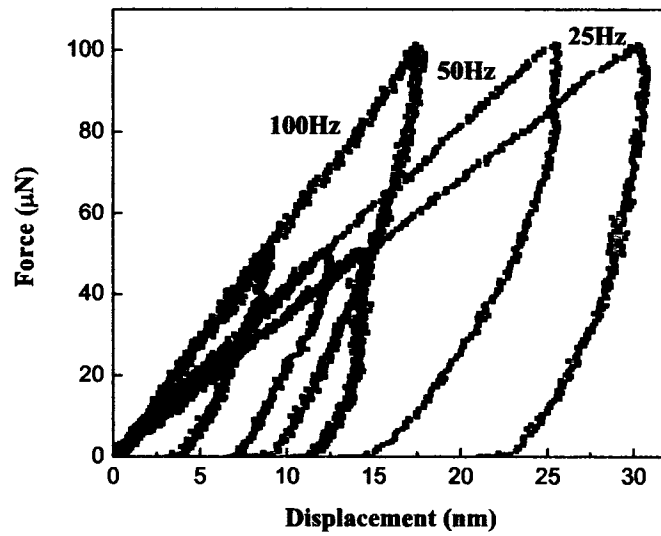
Nano-indentation tests were used to evaluate the effect of deposition parameters on hardness of deposits, associated with AFM observation. Most of the current research is devoted to the adjustment of electrolytes and additives [20, 18, 19, 21], while this study is more focused on the effect of pulse control parameters on the grain size of the deposit. Figure 2.8 shows the force-displacement curves of Cu deposits produced by pulse plating using different frequencies and peak current densities of  $0.2\text{A}/\text{cm}^2$  and  $1\text{A}/\text{cm}^2$ , respectively. At the same peak current density, the frequency was changed from 25Hz to 100Hz through changing current-on time ( $t_{on}$ ) and current-off time ( $t_{off}$ ) simultaneously but fixing the duty cycle  $\theta$ , which is defined as the ratio of the pulse time ( $t_{on}$ ) to the total period ( $t_{on} + t_{off}$ ). The deposition parameters are listed in Table 2.3. The average current density was  $10\text{mA}/\text{cm}^2$  for all conditions. Results indicated that at low  $I_p$  of  $0.2\text{A}/\text{cm}^2$ , the hardness increased with increasing frequency obviously (in Figure 2.8(a)), but the situation be-

came more complicated at higher  $I_p$  of  $1\text{A}/\text{cm}^2$ , at which the film produced by 50Hz showed highest hardness followed by those produced at 25Hz and 100Hz (in Figure 2.8(b)). The effect of frequency on hardness of deposits produced at low and high  $I_p$  is concluded in Figure 2.9. It is obvious that at the same frequency, an increase in  $I_p$  from  $0.2$  to  $1\text{ A}/\text{cm}^2$  dramatically decreased the maximum penetration depths or increased hardness, because the higher cathodic overpotential, caused by a higher instantaneous current density during pulsed-current can accelerate the nucleation process and thus results in the formation of finer grains [23].

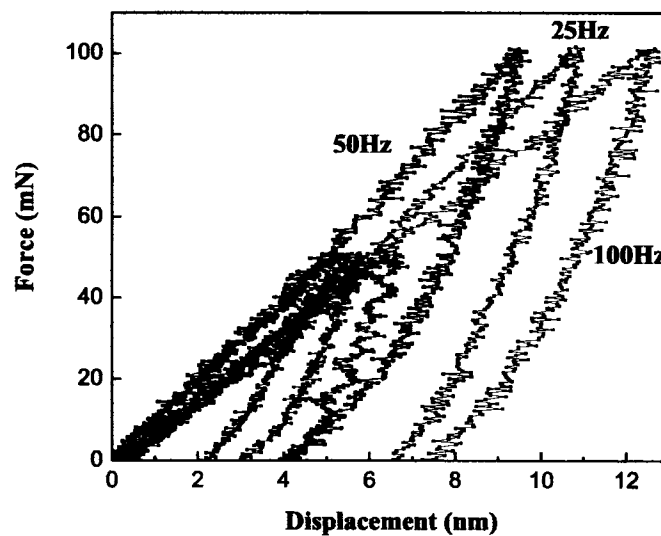
Table 2.3: Deposition parameters for Cu deposits, whose force-displacement curves are illustrated in Figure 2.8

$I_p(\text{A}/\text{cm}^2)$	0.2	0.2	0.2	1	1	1
$t_{on}(\text{ms})$	2	1	0.5	0.4	0.2	0.1
$t_{off}(\text{ms})$	38	19	9.5	39.6	19.8	9.9
$f(\text{Hz})$	25	50	100	25	50	100

The effect of frequency on hardness at low  $I_p$  and high  $I_p$  was attributed to the formation of grains with different sizes. As mentioned earlier, the nanostructure produced by pulse electrodeposition depends on two basic processes, nucleation and grain growth. At low  $I_p$  corresponding to low nucleation rate, during  $t_{on}$   $\text{Cu}^{2+}$  ions were deposited more likely for growth of non-stable grains rather than formation of nuclei. At low  $I_p$ ,  $t_{off}$  is less important because it is usually long enough to supply sufficient ions diffusing to the cathode surface for depletion at low deposition rate. Therefore, increasing the frequency reduces the time interval for continuous deposition and thus accelerates the formation of finer grains by inhibiting grain growth. Shorter  $t_{on}$  results in higher frequency if  $t_{on}/t_{off}$  is fixed, so the grain size decreases with increasing



(a)



(b)

Figure 2.8: Nano-indentation force-penetration displacement curves of Cu deposits produced with different pulse frequencies for different peak current densities: (a)  $I_p = 0.2 \text{ A/cm}^2$ , and (b)  $I_p = 1 \text{ A/cm}^2$ .

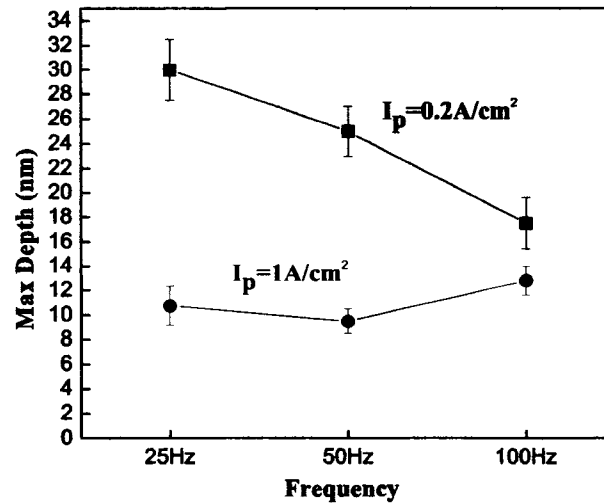


Figure 2.9: The effect of frequency on hardness of films produced at two different current densities.

the frequency. However, at higher  $I_p$ ,  $t_{on}$  and  $t_{off}$  both influence the electrocrystallization process effectively [22], probably in the opposite ways in terms of grain refinement, so that controlling the structure of deposits by only changing the frequency does not always work. As a conclusion, the frequency is not a fundamental parameter for grain size control. As a matter of fact, the frequency is a function of  $t_{on}$  and  $t_{off}$  as Equation (1.1) expresses, which does not reflect individual effects of  $t_{on}$  and  $t_{off}$ . It is reported that the grain size of Zn deposits decreases with increasing  $t_{on}$  time and increases with increasing the  $t_{off}$ , respectively [21]. Inconsistent results are also reported for electrodeposited Cu [22], in which experiments are set by increasing  $t_{on}$  or  $t_{off}$  with increasing  $I_p$  simultaneously in order to fix average current density ( $I_a$ ). It cannot be explained clearly that the decrease in grain size with increasing  $t_{off}$  is only attributed to the grain stabilization since grains also become smaller

with increasing current density. In this study, effort was made to study the individual effects of  $t_{on}$  and  $t_{off}$  on grain size and hardness with keeping  $I_p$  constant.

### Effect of pulse-on time and pulse-off time on grain size and hardness

Table 2.4: Effect of  $t_{off}$  on the grain size and nano-hardness of deposits produced at low and high  $I_p$ .

	$I_p$ (A/cm <sup>2</sup> )	$t_{on}$ (ms)	$t_{off}$ (ms)	Grain size(nm)	Nanohardness(GPa)
DC	0.01			2000	1.17±0.18
PC	0.2	0.5	9.5	78	4.48±0.21
	0.2	0.5	14.5	102	3.53±0.16
	0.2	0.5	19.5	167	2.80±0.16
	1	0.1	4.9	69	4.61±0.23
	1	0.1	9.9	56	4.92±0.16
	1	0.1	14.9	34	5.27±0.16

The experimental results indicate that  $t_{on}$  and  $t_{off}$  have pronounced effects on the grain size of Cu deposits. Figure 2.10 demonstrates how  $t_{off}$  influences the hardness and grain size of Cu deposits produced at a low peak current of  $I_p = 0.2\text{A/cm}^2$  when  $t_{on}$  was kept constant (0.5ms) but  $t_{off}$  changed from 9.5 through 14.5 to 19.5ms. The measured nano-hardness from nano-indentation tests and average grain size determined from AFM images are given in Table 2.4. Results indicate that at low  $I_p$ , the shorter the  $t_{off}$ , the smaller the grain size and the harder the materials, but the situation was reversed at high  $I_p$ . Figure 2.11 and Table 2.4 show the effect of  $t_{off}$  on hardness and grain size of the deposits produced at a higher  $I_p = 1\text{A/cm}^2$ , with a fixed  $t_{on}=0.1\text{ms}$  but changing  $t_{off}$  from 4.9 through 9.9 to 14.9ms. In this case, increases in  $t_{off}$

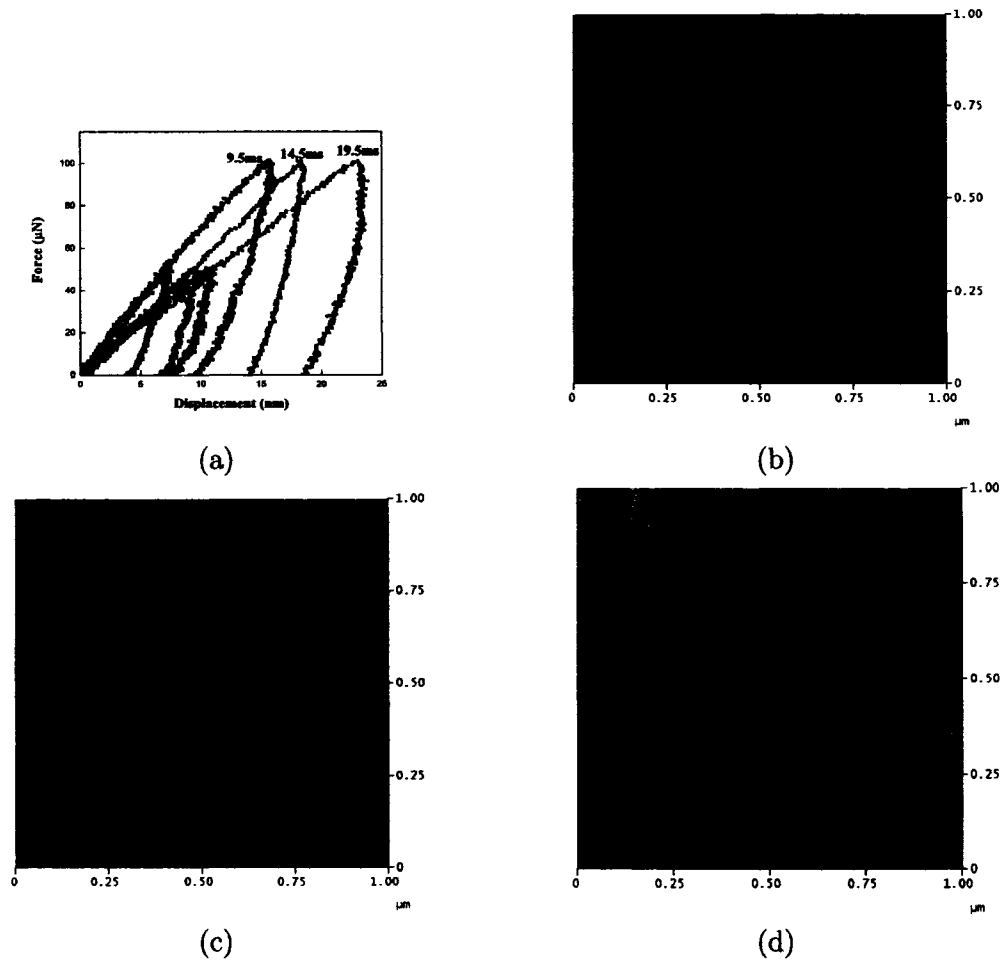


Figure 2.10: Effect of  $t_{off}$  on the nano-hardness and grain size of Cu deposits produced at  $I_p=0.2\text{A}/\text{cm}^2$  and  $t_{on}=0.5\text{ms}$ : (a) Nano-indentation curve, (b) AMF image,  $t_{off}=9.5\text{ms}$ , (c) AMF image,  $t_{off}=14.5\text{ms}$ , and (d) AMF image,  $t_{off}=19.5\text{ms}$  (scanned area =  $1 \mu\text{m}^2$ ).

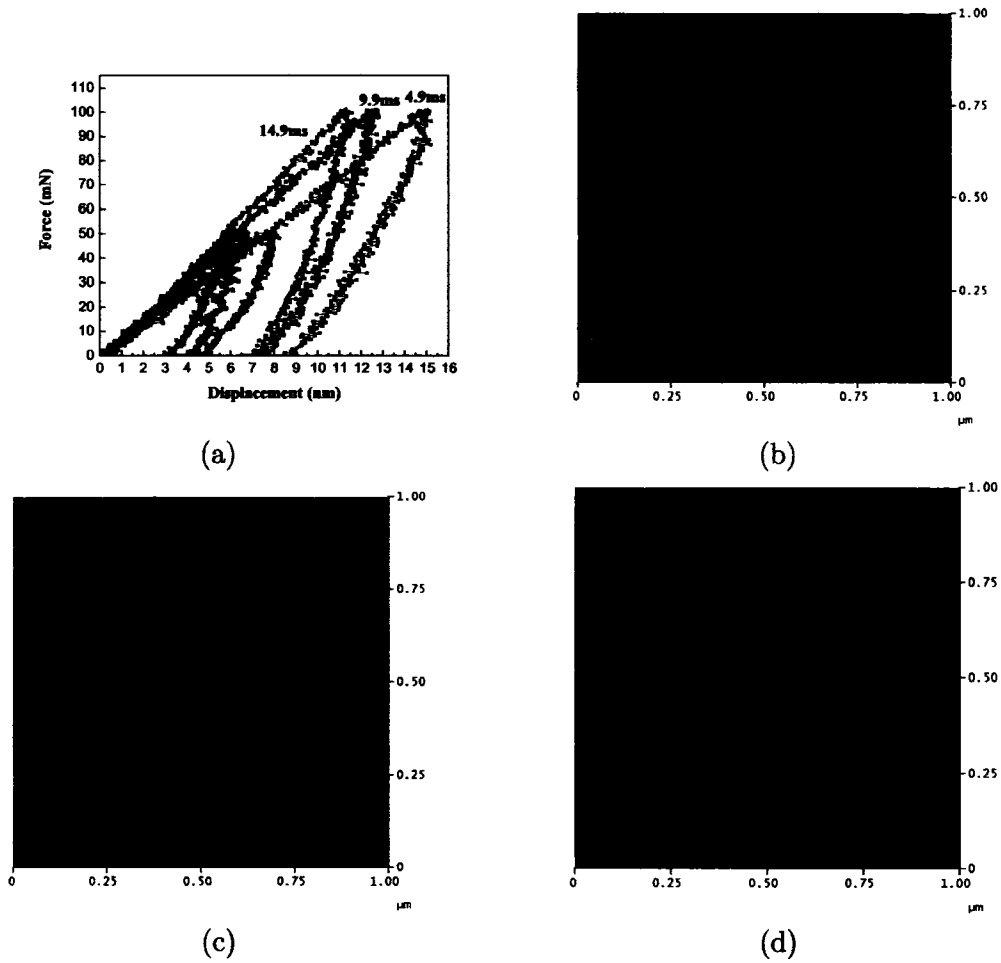


Figure 2.11: Effect of  $t_{off}$  on the nano-hardness and grain size of Cu deposits produced at  $I_p=1A/cm^2$  and  $t_{on}=0.1ms$ : (a) Nano-indentation curve, (b) AMF image,  $t_{off}=4.9ms$ , (c) AMF image,  $t_{off}=9.9ms$ , and (d) AMF image,  $t_{off}=14.9ms$  (scanned area =  $1 \mu m^2$ ).

enhanced the deposit's hardness due to the formation of finer grains.  $T_{off}$  is an ambivalent parameter in a deposition process.  $T_{off}$  should be as long as necessary to enable  $\text{Cu}^{2+}$  ions transport into the depleted vicinity of the cathode, which is more important when deposited at high nucleation rates; otherwise the diffusion layer nearby the cathode may become thicker, thus leading to a decrease in the limiting current density (The maximum current density that can be achieved for an electrode reaction at a given concentration of the reactant in the presence of a large excess of supporting electrolyte [56]). Moreover, longer  $t_{off}$  can make the existing nano-grains stable and not continuously grow in the next pulsed time. The decrease in grain size of deposits with increasing  $t_{off}$  can also be attributed to the fact that during a long  $t_{off}$  period, an increased number of inhibitor thiourea molecules reach the active sites and are adsorbed on the freshly deposited layer, which may block the continued grain growth during the next pulse. Usually, metals migrate faster than the big organic molecules. For short  $t_{off}$ , only a small fraction of the inhibitor molecules reach the growth sites, which is not desirable for grain refinement. However, on the other hand,  $t_{off}$  has to be as short as possible in order to minimize grain growth due to the exchange current density ( $i_0$ ) coming from a couple of balanceable reactions during which the smaller grains dissolve and larger grains grow preferentially, driven by the minimization of grain boundary energy. Although unavoidable, grain growth during the relaxation time proceeds only at a low rate. At low  $I_p$ , the deposit's grains are less uniform because of the uneven charge distribution caused by low overpotential; in this situation, the grain growth during  $t_{off}$  due to the existence of exchange current density cannot be ignored. Therefore, as the results show, at a high  $I_p$ , corresponding to a high nucleation rate, longer  $t_{off}$  favored the formation of fine grains. The

blockage of grain growth in pulse time is important. However, at a lower  $I_p$  corresponding to lower nucleation rate ( $I_p$ ), it is not necessary to use long  $t_{off}$  for the replenishment of Cu ions and inhibitors, and the inhibition of grain growth through decreasing  $t_{off}$  is favourable.

Table 2.5: Effect of  $t_{on}$  on the grain size of deposits produced at low and high  $I_p$ .

$I_p(\text{A/cm}^2)$	$t_{on}(\text{ms})$	$t_{off}(\text{ms})$	Grain size(nm)
0.2	0.5	14.5	102
0.2	0.8	14.5	142
0.2	1.0	14.5	180
1	0.1	14.9	34
1	0.4	14.9	85
1	0.6	14.9	96

$T_{on}$  is another basic parameter affecting the grain size of deposits. Figures 2.12, 2.13 and Table 2.5 demonstrate the effect of  $t_{on}$  on the grain size of Cu deposits produced at high  $I_p = 1\text{A/cm}^2$  and low  $I_p = 0.2\text{A/cm}^2$ , respectively, while keeping  $t_{off}$  constant. As shown, no matter at high or low  $I_p$ , the grain size of Cu deposits increased with increasing  $t_{on}$ . This happened because a shorter  $t_{on}$  reduced the number of ions discharged to deposit and thus limited the growth of nuclei. By analyzing the above experimental results, one may see that the effect of  $t_{on}$  on grain size is basically consistent with that of frequency. However,  $t_{off}$  also plays a crucial role, largely depending on the peak current density,  $I_p$ .

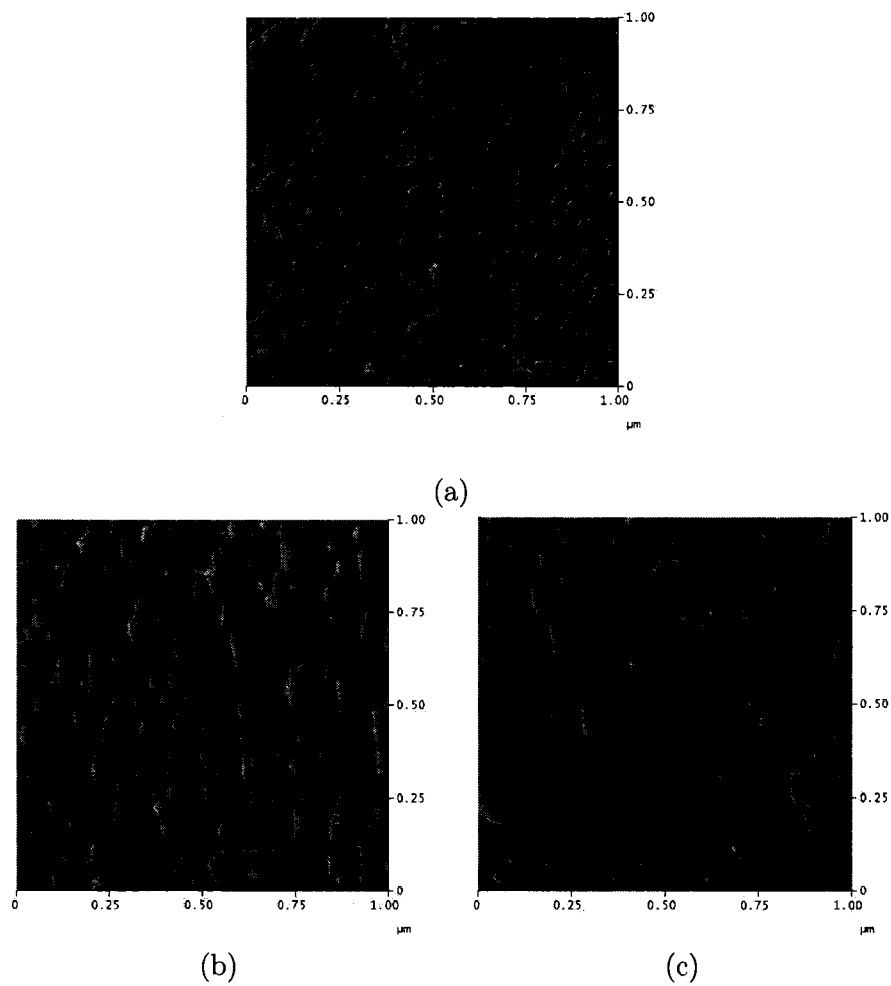


Figure 2.12: Effect of  $t_{on}$  on the grain size, AFM images of Cu deposits produced at  $I_p=1\text{A}/\text{cm}^2$  and  $t_{off}=14.9\text{ms}$  with different  $t_{on}$ : (a) 0.1ms, (b) 0.4ms, and (c) 0.6ms.

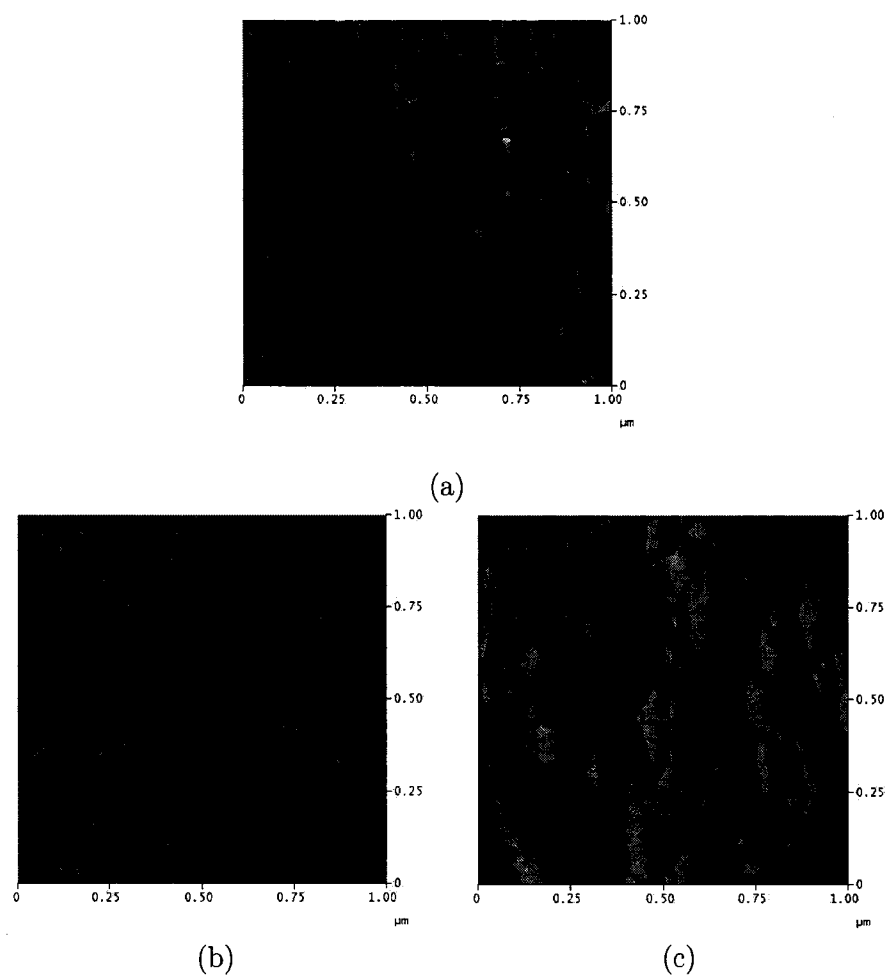


Figure 2.13: Effect of  $t_{on}$  on the grain size, AFM images of Cu deposits produced at  $I_p=0.2\text{A}/\text{cm}^2$  and  $t_{off}=14.5\text{ms}$  with different  $t_{on}$ : (a) 0.5ms, (b) 0.8ms, and (c) 1.0ms.

**Discussion on effects of the process parameters on nanocrystallization**

According to the electrocrystallization theory, the crystallization process usually takes place in two steps. The first step is the discharge of copper ions and the generation of copper atoms. There are two possibilities for the second step: i) the incorporation of copper atoms into crystal, namely grain growth, and ii) the formation of new nuclei when the rate of crystal growth may not be sufficient to cater for faster generation of the atoms. If the generation of new nuclei is dominant in the second step, fine-grained deposits are obtained.

The cathodic overpotential and the exchange current nucleation rate are the crucial electrochemical quantities. A large cathodic overpotential favors a high nucleation rate resulting in the formation of crystallite nuclei in large quantities but small size. The necessary large current density can not be achieved for DC-electrodeposition because of ionic transport limitation. But large current densities are feasible as peak current density in short current pulse because in this way sufficient ionic transport takes place during  $t_{off}$ . Moreover, the higher the peak current density, the faster is the nucleation rate. To some extent, a small  $t_{on}$  means a high  $I_p$  for a fixed average current density. A short current on time and relatively long pulse relaxation time limits the growth of nuclei during deposition. The exchange current is the main reason for the grain growth in the relaxation time, which occurs during the  $t_{off}$  in such a way larger that grains grow at the expense of smaller ones. Since the grain growth is hardly avoidable,  $t_{off}$  should therefore be optimized to limit the time of grain growth.  $T_{off}$  should be as low as possible and as large as necessary for the stabilization of the nano-grains and recovery of the ion concentration in the solution around the cathode.

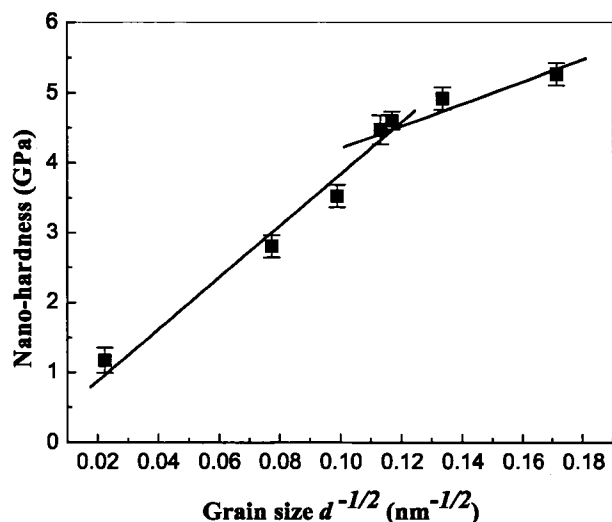


Figure 2.14: Effect of the grain size on nano-hardness ( $d$ , the average diameter of grains).

How to control the grain size of deposits and refine grains are extremely important in studying the nanostructure materials and effects of grain size and grain boundary on materials properties. The first way for grain size reduction is an electrodeposition process with short  $t_{on}$  combined with high  $I_p$ . The second way is the use of an electrolyte for deposition, which contains organic additives (e.g. carboxylic acids). A third but less-recommendable way for grain size control is the variation of the bath temperature.

## 2.7 The Relation Between Hardness and Grain Size at Nano-scale

The formation of nanocrystalline deposits by pulse electrodeposition can be achieved if abundant nuclei are generated on the substrate at a high rate and the grain growth is effectively impeded. Generally, nanocrystalline deposits can be realized by controlling three basic parameters,  $I_p$ ,  $t_{on}$  and  $t_{off}$ .

A nanocrystalline deposit has higher hardness as demonstrated in Table 2.4. According to Hall-Petch relation (Equation (1.5)), for many microcrystalline metals and alloys, the hardness increases inversely with the square root of the average grain diameter. The hardness of Cu coatings with different grain sizes is illustrated in Figure 2.14, demonstrating the linear relation between  $H$  and  $d^{-1/2}$ . The key mechanism for grain refinement strengthening is that dislocations are blocked by grain boundaries, which enhances the resistance to plastic deformation. However, as the grain size is further refined and is smaller than 100nm, the strengthening effect decreases (see Figure 2.14) and may eventually become negative as the grain size is below 10 nm, i.e. the so-called inverse Hall-Petch relation occurs [2]. In this case, sliding of a large number of grain boundaries in nanocrystalline deposits could be responsible for weakened strengthening effect as well as the inverse Hall-Petch relation [26]. Grain-boundary sliding becomes a dominant deformation mechanism when the grain size reaches ultra-fine scale, like 10nm.

## 2.8 Conclusions

The main conclusions drawn from studies reported in this chapter are:

- Nanocrystalline and microcrystalline copper deposits were successfully produced by PC and DC electrodeposition processes, respectively. The grain size of the nanocrystalline deposit was about 56nm determined by XRD and AFM.
- Changing the electrodeposition parameters, e.g.,  $t_{on}$ ,  $t_{off}$  and  $I_p$ , is an effective way to control the grain size and corresponding properties of the deposit. At high  $I_p$ , the longer the  $t_{off}$  or the shorter the  $t_{on}$ , the

finer is the grain. However, grain size decreases with decreases in both  $t_{off}$  and  $t_{on}$  at low  $I_p$ .

- Mechanical properties of the nanocrystalline copper film are markedly superior to those of the DC-plated film with higher hardness and  $\eta$  value. Hardness increases with grain refinement, but the strengthening effect is weakened when the grain size gets into the nano-scale below 100nm.

## CHAPTER 3

### ELECTROCHEMICAL BEHAVIOR AND STABILITY

#### 3.1 Introduction

Metals are generally polycrystalline consisting of many randomly oriented crystallites or grains. Reducing the size of grains can lead to a great impact on materials properties. As the grain size in a metal is reduced to the nanoscale, a large portion of atoms are located at grain boundaries, where they behave differently from those within the crystallites, which may dramatically alter the overall properties of the metal. It has been demonstrated that nanocrystalline metals exhibit considerably higher strength, improved magnetic properties, higher diffusion coefficient, and improved thermal expansion properties [5]. Electrochemical stability should also be affected by nanocrystallization. It is known that corrosion is strongly influenced by microstructure [56]. Nanocrystalline materials have a higher density of grain boundaries, which render electrons more active, thus varying the corrosion behavior. However, we cannot simply determine corrosion properties of a nanocrystalline material only based on the increased surface reactivity due to its high grain boundary density, because the high grain boundary density affects the formation of the surface oxide film that influences the surface reactivity as well. As a matter of fact,

previously reported studies are not always consistent (see Section 1.4). Therefore, how a nanocrystalline structure influences the electrochemical properties and why discrepancies exist in literature need clarification.

The main objective of this part of the study is to investigate how the nanocrystalline structure influences the electrochemical behavior when attacked by different corrosive media. The electron stability and chemical reactivity of the film surfaces were evaluated by measuring their electron work function (EWF). Corrosion behavior of the Cu electrodeposits was studied in various solutions, including NaOH, NaCl and H<sub>2</sub>SO<sub>4</sub>, using potentiodynamic polarization and electrochemical impedance measurements. The contributions of mechanical and electrochemical actions during corrosive wear were investigated using an electrochemical scratch technique.

### 3.2 Experimental Procedure

#### Dynamic polarization

Electrochemical polarization measurements were carried out in a 0.1M NaOH solution, 3.5wt% NaCl solution and 1M H<sub>2</sub>SO<sub>4</sub> solutions, respectively, using a commercial electrochemical system (Gamry Instruments Inc., Warminster, PA, USA). All as-deposited coatings were polished using a slurry paste containing 0.05 $\mu$ m aluminum particles and then rinsed with de-ionized water and degreased with acetone thoroughly before the electrochemical tests. The passivation behaviors of the deposits in the different solutions were evaluated using dynamic polarization tests at a scan rate of 5mVs<sup>-1</sup> from -200mV to 1000mV about the corrosion potential ( $E_{corr}$ ). Anodic and cathodic Tafel slopes were determined in the range of 100mv about the  $E_{corr}$  at a scanning rate of 0.5mVs<sup>-1</sup>. The linear polarization resistance was determined by per-

forming polarization test in the range of 5mV about the  $E_{corr}$  at a scanning rate of  $0.1\text{mVs}^{-1}$ . Before the tests, the deposits were mounted with epoxy and had their surface area of  $100\text{mm}^2$  exposed to the corrosive medium for 30 min. A saturated calomel electrode (SCE) was used as the reference electrode and a platinum plate was used as the counter electrode. All electrochemical tests were performed at room temperature.

### **Electron work function measurement**

The electrochemical stability of deposit surfaces after immersion in different solutions, respectively, for 2 hours was evaluated using a scanning Kelvin probe (SKP, made by KP Technology Ltd., Wick, UK) by measuring their electron work function under the ambient conditions. A gold tip of 1mm in diameter was used to scan the surface within an area of  $2\times 2\text{mm}^2$  covering  $10\times 10$  measurement points. The EWF was represented using an average value over the scan area. The oscillation frequency of the SKP tip was 173Hz.

### **Contact electrical resistance**

The failure resistance of the passive films formed on the deposits was evaluated by scratch tests using a universal micro-tribometer (UMT, provided by CETR, Mountain View, California, USA). Before tests, the passive films on the PC- and DC-plated deposits were formed by immersion in 0.1M NaOH under an imposed potential of 0.1V (vs. SCE) for 1min at room temperature. Figure 3.1 is a schematic illustration of the scratch test performed on the passive film on a Cu coating surface. During the scratch test, the surface was scratched under a normal load, which was increased linearly from 0 to 10g. The scratch probe was made of tungsten carbide. The information on the probe geometry

can be found in [18]. During scratching, the tip scratched the surface under the applied load at a velocity of 0.05mm/s. At the same time, changes in the contact electrical resistance (CER) between the tip and specimen surface with respect to the load were recorded. When the passive film failed under a critical load, the CER value dropped steeply. The critical load is therefore a measure of the resistance of a passive film to failure.

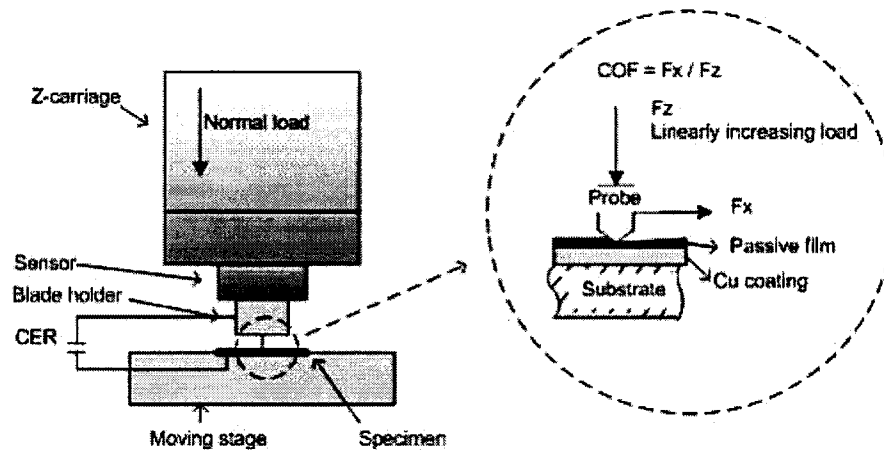


Figure 3.1: Schematic of the scratch test for the passive films on Cu coatings with in situ monitoring the contact electrical resistance (CER).

### Electrochemical impedance

Electrochemical impedance (EI) measurements were carried out using a Gamry electrochemical system. The frequency range was chosen from 0.01 Hz to 100000 Hz with 5-mV peak amplitude about the corrosion potential. Before performing the experiments, the cell electrodes were kept in a solution under study for 30 min in order to stabilize the corrosion potential. To evaluate the protective efficiency of a passive film, the EI measurement were employed on the sample as a function of immersion time. An equivalent-circuit simulation

program was used for data fitting and analysis.

### 3.3 Polarization Behaviors of nc-Cu Deposits in Different Corrosive Media

The electrochemical behavior of nanocrystalline Cu deposits in different solutions was investigated using potentiodynamic polarization experiments. Figure 3.2 illustrates polarization curves of both nanocrystalline and microcrystalline Cu deposits in 1M H<sub>2</sub>SO<sub>4</sub>, 3.5wt% NaCl and 0.1M NaOH solutions, respectively. In the H<sub>2</sub>SO<sub>4</sub> solution, there is no appreciable difference between nanocrystalline and microcrystalline Cu deposits. No active-passive polarization behavior was observed for both the deposits because the current densities were very high in the anodic region. In the NaCl solution, the polarization curves of nc- and mc-Cu deposits are also similar to each other. The active-passive polarization behavior was noticed for either of the nc-Cu and mc-Cu deposits, but there was no obvious stable passive region. The corrosion potential of nc-Cu was lower than that of the mc-Cu. Above the breakdown potential, where the current starts to increase with increasing potential due to the breakdown of passive film, the nanocrystalline Cu exhibited higher dissolution rate or higher current density. In the NaOH solution, both the deposits were passive (see Figure 3.2(c)). Electrochemical polarization curves of two additional nanocrystalline Cu deposits with grain sizes of 34nm and 69nm, respectively, are also presented in Figure 3.2(c). The morphology of the deposits and corresponding deposition parameters are illustrated in Figure 3.3. Compared with the microcrystalline one, all nanocrystalline Cu deposits exhibited improved passivation behavior with lower current densities in the passive region, although the corrosion potential was slightly more negative. Moreover,

### 3.3 Polarization Behaviors of nc-Cu Deposits in Different Corrosive Media 64

the passive current density decreased with decreasing grain size. At high potentials greater than the breakdown potential, the polarization curves of nc- and mc-Cu deposits overlap each other, indicating that in NaOH solution, the dissolution rate at high potential is not controlled by the structure as it was at relatively lower potentials in the passive region.

The passivation behavior of a metal depends on its microstructure and the electrolyte. In the NaOH solution, the deposits are passive and more stable and protective than those formed in the NaCl and H<sub>2</sub>SO<sub>4</sub> solutions. These may be seen from some parameters that can be estimated from the polarization curves (see Figure 3.4), including passive current density  $i_p$ , critical current density  $i_c$ , at which the current starts to decrease with increasing potential before getting into the passive region, passivation potential  $E_p$ , the lowest potential of metal in passive region, and the breakdown potential  $E_b$ . These parameters of the nc-Cu and mc-Cu deposits are presented in Table 3.1.  $i_c$  and  $E_p$  reflect the degree of ease for passivation. The lower the  $i_c$  and  $E_p$ , the easier is the system to be passivated.  $i_p$  and  $E_b$  are related to the stability of the passive state. As shown, the passive film formed in NaOH is more protective than that formed in NaCl associated with lower  $i_p$ , or a smaller dissolution rate of the passive film, and a higher  $E_b$ , that reflects higher resistance of the passive film to damage. The higher the  $E_b$ , the larger the pitting corrosion resistance. In NaCl, the passive film is not stable and easily damaged because the pitting corrosion caused by Cl<sup>-</sup> is more severe than that caused by other ions. In the H<sub>2</sub>SO<sub>4</sub> solution, passivation parameters cannot be obtained directly from polarization curves because there is no stable passive film formed on deposits.

Furthermore, in NaOH solution the grain size has a noticeable effect on the passivation behavior. As shown in Figure 3.2(c), when the grains become

### 3.3 Polarization Behaviors of nc-Cu Deposits in Different Corrosive Media 65

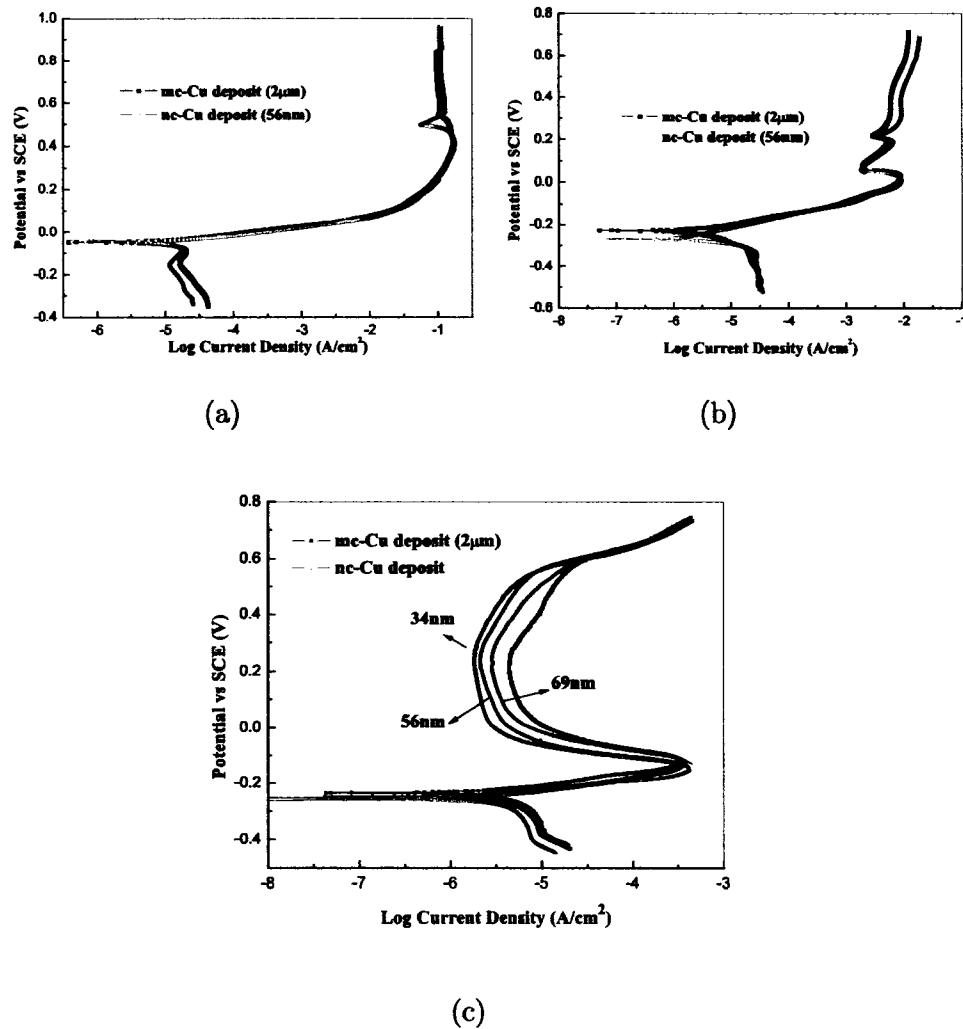


Figure 3.2: Dynamic polarization curves of nanocrystalline and microcrystalline Cu deposits in 1M H<sub>2</sub>SO<sub>4</sub> (a), 3.5wt% NaCl (b) and 0.1M NaOH (c).

### 3.3 Polarization Behaviors of nc-Cu Deposits in Different Corrosive Media 66

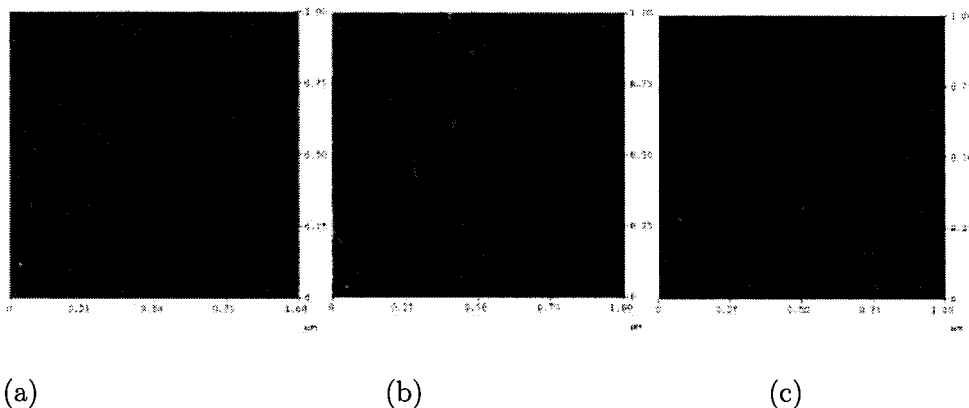


Figure 3.3: AFM images of nanocrystalline Cu deposits produced at a peak current density of  $1\text{A}/\text{cm}^2$  and a current-on time of  $0.1\text{ms}$ : (a)  $t_{off}=4.9\text{ms}$ , grain diameter  $D=69\text{nm}$ ; (b)  $t_{off}=9.9\text{ms}$ ,  $D=56\text{nm}$  and (c)  $t_{off}=14.9\text{ms}$ ,  $D=34\text{nm}$ .

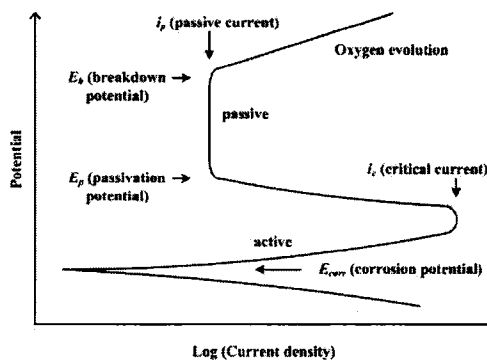


Figure 3.4: A schematic polarization curve illustrating a few electrochemical parameters that can be determined from the polarization curve.

### 3.3 Polarization Behaviors of nc-Cu Deposits in Different Corrosive Media 67

Table 3.1: Passivation parameters obtained from polarization curves of nanocrystalline (56nm) and microcrystalline (2 $\mu$ m) copper deposits in different solutions.

Solution	Materials	$E_{corr}$ (mV)	$E_p$ (mV)	$E_b$ (mV)	$i_c$ (mA)	$i_p$ (mA)
H <sub>2</sub> SO <sub>4</sub>	nano	-48	-	-	63.0	-
	micro	-52	-	-	58.8	-
NaCl	nano	-215	64	208	12.6	1.78
	micro	-270	58	202	12.4	1.58
NaOH	nano	-230	35	563	3.6	$6.3 \times 10^{-3}$
	micro	-248	24	573	3.8	$2.2 \times 10^{-3}$

smaller, both passive current and passive potential decrease. The refinement of grains improved the passivation behavior. A geometric calculation shows that the volume fraction of grain boundary could be as high as 50% in a solid having its grains smaller than 5nm in diameter, and lower than 1% when the grain size is 1 $\mu$ m [10]. Atoms in the vicinity of a grain boundary have higher energy and are therefore less stable than atoms within grains. As a result, a solid having finer grains is more active to participate in electrochemical reactions. So the nanocrystalline Cu deposits was less inert with a more negative corrosion potential before getting into the passive region. In the NaCl solution, the nc-Cu deposits corroded faster than mc-Cu when the relatively weaker passive film was damaged at high potentials. However, on the other hand, a high reactivity accelerates passivation. Since the formation of passive films on the corroded surface is controlled by diffusion [8], with a higher density of grain boundaries, nanocrystalline materials usually exhibit anomalously enhanced diffusion because the mass transport along grain boundaries is much faster than that within grains. Consequently, the nanocrystalline deposit exhibited improved passivation behavior than the microcrystalline one evidenced by its lower current density in the passive region. The passive current den-

sity decreased with decreasing the grain size, although the critical current of passivation for all the deposits were similar.

### 3.4 Corrosion Study of Nanocrystalline and Microcrystalline Cu deposits

The corrosion rates of the nanocrystalline and microcrystalline deposits in different solutions were determined using the Stern-Geary relation [72] and the polarization experimental results.

$$i_{corr} = \frac{\beta_a \beta_c}{2.303 R_P (\beta_a + \beta_c)} \quad (3.1)$$

where,  $i_{corr}$  is the corrosion current density or corrosion rate,  $R_P$  the polarization resistance, and  $\beta_a$ , and  $\beta_c$  the anodic and cathodic Tafel slopes, respectively. The polarization resistance was determined from the slope of the linear potential vs. current density plot in the range of 5mV about the corrosion potential.

$$\left(\frac{dE}{di}\right)_{i \rightarrow 0} \quad (3.2)$$

The calculated corrosion rates are illustrated in Figure 3.5. As shown, in the NaOH solution, the nc-Cu exhibited a lower corrosion rate than that of the mc-one. In the NaCl, nc-Cu showed a slightly higher corrosion resistance. However, in the H<sub>2</sub>SO<sub>4</sub> solution, the result was reversed. The different corrosion resistances of the deposits in different solutions may result from different films formed on the deposits. A stable oxide of copper with properties close to those of a p-type semiconductor [73] could form in solution in high pH ranges, e.g., NaOH. The oxide films retarded the migration of copper ions or elec-

trons to the surface, thus suppressing further electrochemical reactions. The high-density of grain boundaries in the nc-deposits could promote the atomic migration and thus enhance its passivation capability. Besides, the high density of grain boundaries in the nc-deposit could also enhance the adhesion between the passive film and the deposit due to the increase in the electron activity at grain boundaries and possible pegging of the passive film into the GB. As a result, a more protective passive film could form on the nc-deposit in the NaOH solution, leading to improved corrosion resistance. However, in acidic solutions with low pH values, copper does not form a stable passive film [74]. Therefore, the nc-Cu corroded faster due to the higher reactivity of its nanostructure. It is known that grain boundaries are usually preferential attack sites when exposed to a corrosive environment [56]. They act as anodes due to their interfacial mismatch and possible segregation of impurities. Consequently, the nc-deposit performed poorly when in the H<sub>2</sub>SO<sub>4</sub> solution without passivation. As for the NaCl solution, the performance of nc-deposit depends on the stability of the passive film. If the passive film was damaged, the nc-Cu deposit could suffer more from corrosion attack than the mc-one.

### 3.5 Surface Stability of nc- and mc- Cu Deposits

Table 3.2: EWFs of nanocrystalline (56nm) and microcrystalline (2 $\mu$ m) Cu deposits after immersion in different solutions.

Materials	NaOH	NaCl	H <sub>2</sub> SO <sub>4</sub>
nc-Cu	4.62 $\pm$ 0.04	4.39 $\pm$ 0.04	4.15 $\pm$ 0.05
mc-Cu	4.33 $\pm$ 0.05	4.30 $\pm$ 0.03	4.19 $\pm$ 0.04

In order to better understand the electrochemical properties of nc- and mc-deposits, the chemical stability of deposit surfaces was investigated by measur-

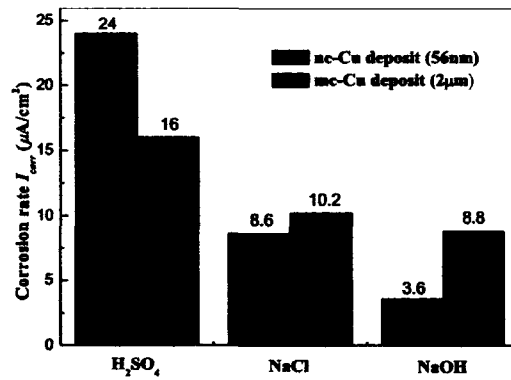


Figure 3.5: Corrosion rates of nanocrystalline and microcrystalline Cu deposits in different solutions.

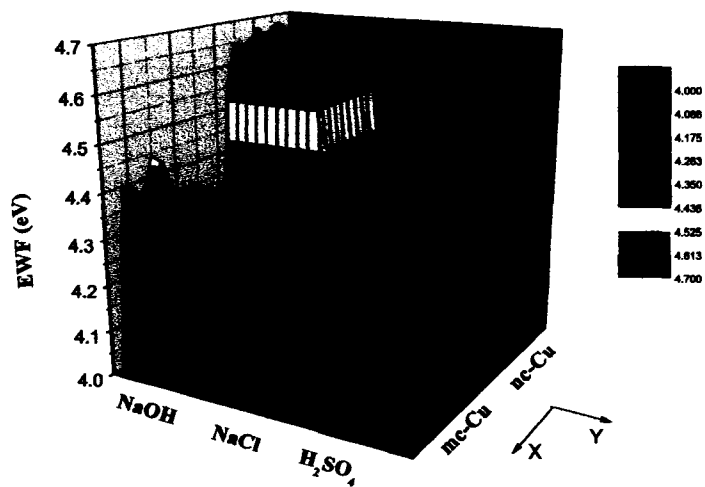
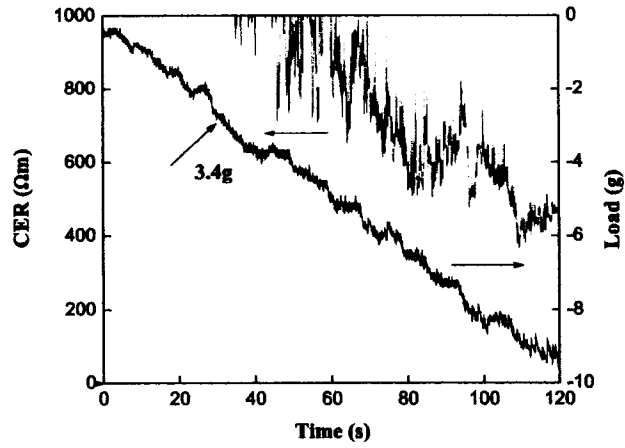


Figure 3.6: EWFs (eV) of nanocrystalline (56nm) and microcrystalline (2 $\mu m$ ) Cu deposits after immersion in different solutions for 2 hours (X and Y are coordinate axes for the scanned area).

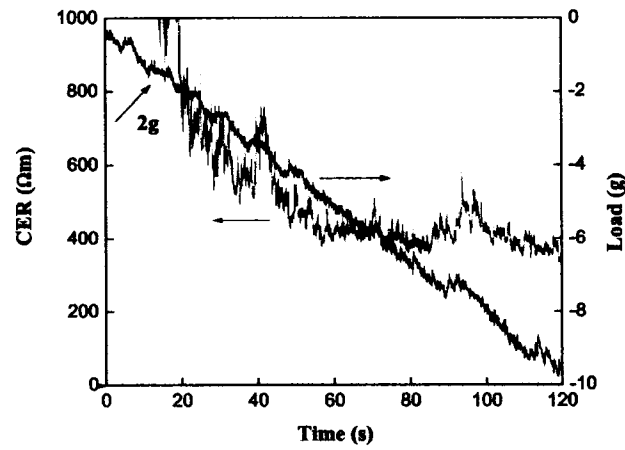
ing their electron work function, which refers to the minimum energy required to move an electron from the interior of a solid to its surface [37]. As a highly sensitive indicator of surface condition, EWF is influenced by adsorbed layers, surface reconstruction, surface charging, oxide films, surface imperfections and contamination, etc [43, 49, 52]. The EWF reflects the inertness of a surface to environmental attack. An increase in EWF may correspond to an increase in the stability of surface and its resistance to electrochemical attack. In the present study, the nanocrystalline (grain size of 56nm) and microcrystalline ( $2\mu\text{m}$ ) Cu deposits were immersed in NaOH, NaCl and  $\text{H}_2\text{SO}_4$  solutions for 2 hours, respectively, then rinsed thoroughly with de-ionized water and dried immediately before the EWF measurement. EWF tests were performed using a scanning Kelvin probe in the ambient condition. Average EWF values of different deposits after immersion in the different solutions were measured, which together with typical EWF diagrams are shown in Table 3.2 and Figure 3.6, respectively. It was demonstrated that the nanocrystalline surface had a higher EWF in the NaOH and NaCl solutions so that it was more electrochemically stable than the microcrystalline one in these two solutions. However, the nanocrystalline Cu deposit was less noble than the microcrystalline one in the  $\text{H}_2\text{SO}_4$  solution. These phenomena may be explained when the formation of a passive film on the deposit is taken into account. It is known that stable oxides of copper could form in the range of pH8-pH12. When the pH value is below 7, the dissolution of copper becomes significant, especially when  $\text{pH} < 5$ , the formation of stable surface oxides becomes impossible [74]. A protective passive film could increase EWF or the surface electron chemical stability [49]. Therefore, the higher EWF of nc-Cu deposit in NaOH can be attributed to the formation of a more protective passive film. However, in the acidic solution,

without the formation of a stable passive film, the EWF of the nc-deposit was lower due to its high-density of grain boundaries that made the surface more reactive. The situation changed in the NaOH solution; the high-density of grain boundaries could render electrons more active and thus accelerate the formation of a protective passive film. The EWF results are consistent with the electrochemical behavior of the deposits determined during the polarization tests in different solutions. The nanostructure enhanced both the kinetic process of passivation and the stability of the passive film. It should be mentioned there is strong correlation between EWF and corrosion rate. As shown in this study, the higher EWFs corresponded to lower corrosion rates.

In order to further evaluate the effect of nanocrystallization on the passivation behaviour and properties of the passive film, micro-scratch experiments were carried out to evaluate the resistance of the passive film to scratch failure. Since the natural passive film formed on Cu deposits could be too thin to be detected, the deposits were passivated by anodic polarization in 0.1 M NaOH before the scratch test. The formation of passive films on Cu in aqueous solution is in agreement with the Pourbaix diagram [75]. With an increasingly important role in electric chips, the knowledge about the passivation behavior of Cu and the properties of its anodic layer is of great importance. During the scratch tests, the specimen surface was scratched by a tungsten carbide tip under an applied load that was increased gradually. The contact electrical resistance (CER) was monitored *in situ* with respect to the load. When the passive film failed under a critical load, the tip contacted the substrate metal, leading to a drop in CER as shown in Figure 3.7. This critical load corresponding to the drop in CER is a measure of the resistance of the passive film to scratch or its protection capability. In Figure 3.7, the passive film



(a)



(b)

Figure 3.7: Micro-scratch tests with *in situ* monitoring changes in the contact electrical resistance (CER) with respect to the applied load: (a) *nc*-Cu deposit (56nm), and (b) *mc*-Cu deposit (2 $\mu\text{m}$ ).

of nanocrystalline Cu failed under a critical load of 3.4g, higher than that of passive film on the microcrystalline one, which is 2g. This further confirms that the passive film formed on nanocrystalline surface is stronger and more adhesive and protective.

### 3.6 Electrochemical Impedance Spectroscopy Analysis

The passive films formed on metal surfaces can be protective or non-protective. If a passive film can protect a metal from corrosion, its stability and resistance could increase with time when exposed to the electrolyte. If the metal surface has a porous hydroxide layer that only slows down corrosion but does not protect the metal from further corrosion, its stability and resistance may decrease. Electrochemical impedance technique is a useful technique to characterize passive films, which was employed in this study to investigate the surface degradation of the nc- and mc-deposits with time in different solutions. The surfaces can be tested in relatively equilibrium condition, compared to the potential sweep techniques that may generate relatively large errors because of changes in surface properties under a large electrode over-potential. The Nyquist plots for nanocrystalline and microcrystalline Cu deposits after immersion in different solutions for different periods of time are presented in Figure 3.8. The diameter of the semicircular curves in Figure 3.8 is a measure of the polarization resistance [56]. As shown, in NaOH the diameters of the semicircles increase with the immersion time and the nc-Cu deposits have greater diameters than the mc-deposits. The increase in the diameter of a  $Z'' \sim Z'$  curve with time indicates an increase in the corrosion resistance, so the corrosion products, i.e., the passive film can protect the surface from further corrosion, especially for nanocrystalline copper. However, in the  $H_2SO_4$

solution, the diameter of the  $Z'' \sim Z'$  curves decreases with the immersion time and the nc-Cu deposits have smaller diameters, indicating that the corrosion products at the surface can not protect the surface. Or, without the formation of a protective passive film in the solution, nanocrystalline copper corroded faster because of its high-density of grain boundaries. In the NaCl solution, there was no significant difference in the curves' diameter of nc- and mc-Cu deposits.

A model circuit shown in Figure 3.9 was used to simulate the passive film and Cu-electrolyte interface in an aqueous solution. In this model circuit, there is a solution resistance ( $R_{\Omega}$ ) between the working electrode and the reference electrode. Both  $Q_{pf}$ , a constant phase element for the passive film, and  $R_{pf}$ , the passive film resistance, characterize properties of the passive film formed on Cu deposits. These parameters were analyzed as a function of time.  $Q_{dl}$  is a constant phase element for the electrical double layer, and the charge transfer resistance ( $R_{ct}$ ) represents electrochemical properties of metal-electrolyte interface. Capacitors in EIS experiments often do not behave ideally. Instead, for a non-uniform surface, the ideal capacitive element would be replaced by the constant-phase element  $CPE$ , which fits the EI results better. For example, the double layer capacitor on real cells often behaves like a  $CPE$  instead of like a capacitor. The impedance of constant phase element has the form [56]:

$$Z_{CPE} = [Q(j\omega)^n]^{-1} \quad (3.3)$$

where  $Q$  is a constant which has the numerical value of the admittance, and  $n$  is a fitting parameter, which takes into account the degree of surface inhomogeneity as a function of the immersion time.  $Q$  and  $n$  are frequency-independent

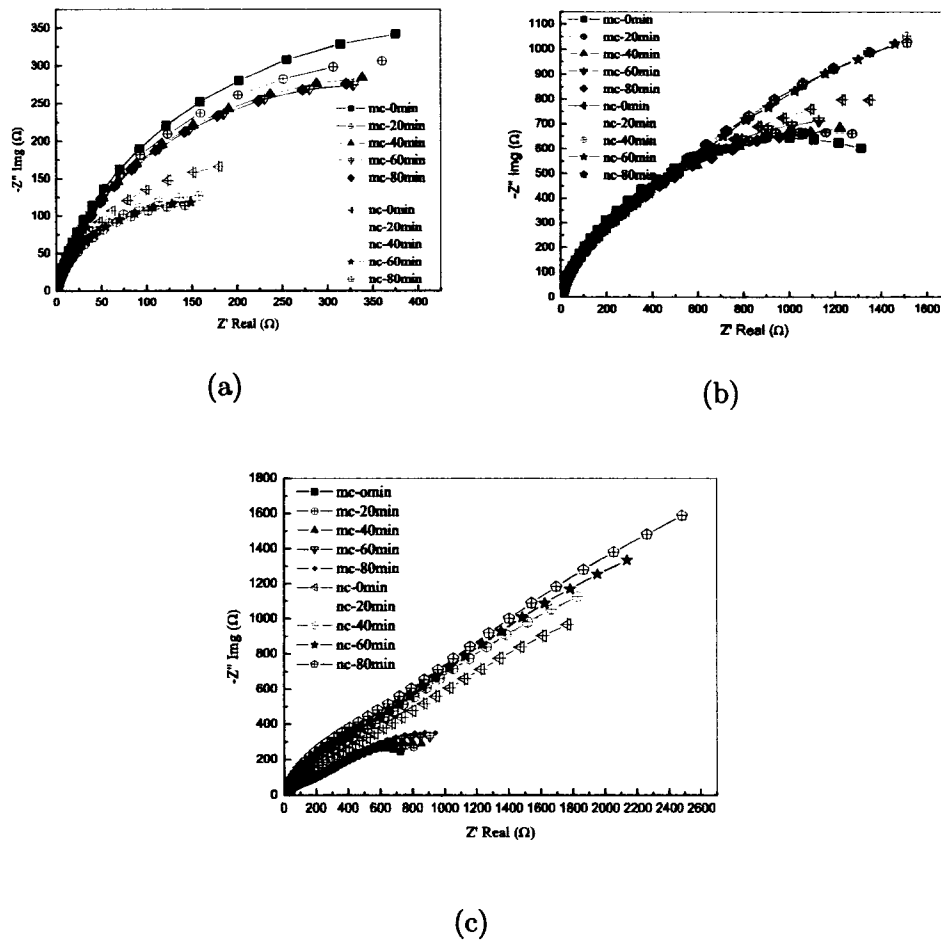


Figure 3.8: Nyquist plane plots of the nanocrystalline (56nm) and microcrystalline ( $2\mu\text{m}$ ) Cu deposits after different periods of immersion time in  $1\text{M H}_2\text{SO}_4$  (a),  $3.5\text{wt}\%\text{NaCl}$  (b), and  $0.1\text{M NaOH}$  (c).

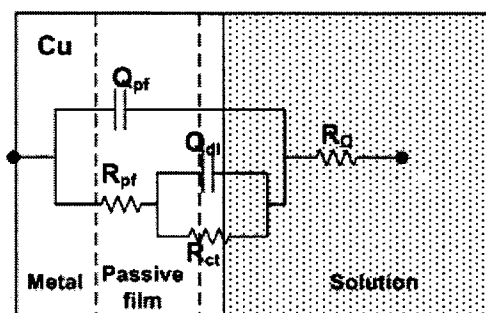


Figure 3.9: A proposed equivalent circuit used to fit experimental EIS data for the Cu deposits-passive film impedance system.

parameters. For an ideal capacitor,  $n=1$  ( $Q$  is equal to the capacitance  $C$ ), and for an ideal resistor,  $n=0$ . For  $0.5 < n < 1$ , the  $CPE$  describes a distribution of dielectric relaxation times in the frequency space. The presence of a  $CPE$  is attributed to the non-ideal capacitive behavior of the barrier film caused by the inhomogeneities of the electrode material. A simulation program was used to build a model circuit and fit it with experimental data using a complex non-linear least-square procedure with minimum error. The variations in some circuit parameters with the immersion time are analyzed as follows.

Variations in the solution resistance as a function of the immersion time are shown in Figure 3.10. There are no noticeable changes in the solution resistance during the immersion time for all cases. Usually, this resistance is small for a given electrolyte. The nc-Cu deposit in the NaOH solution had a relatively high value of solution resistance about  $20\text{ohm}\times\text{cm}^2$ .

Variations in the constant phase element of the passive film as a function of the immersion time are illustrated in Figure 3.11. Surface films formed in the solutions had sufficiently high  $n_{pf}$  values (approximate 1), so that  $CPE$  could be regarded as the capacitance of the surface films formed in these solutions. The capacity  $C$  of a generated oxide passive film can be examined using the

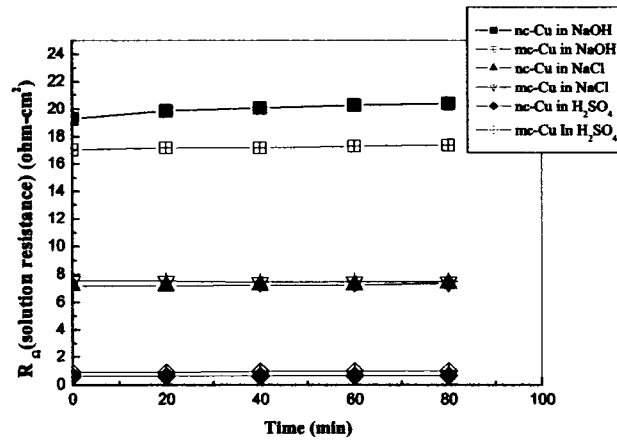


Figure 3.10: Variations in the solution resistance ( $R_s$ ) with the immersion time for nanocrystalline (56nm) and microcrystalline (2 $\mu$ m) Cu deposits in different solutions, respectively.

equation for a parallel plate capacitor:

$$\frac{1}{C} = \frac{d}{\epsilon\epsilon_0 A\sigma} \quad (3.4)$$

where  $d$  is the thickness of the oxide passive film,  $\sigma$  is a surface roughness-related factor,  $A$  is the effective surface area of the passive film,  $\epsilon_0$  is the dielectric constant of vacuum, and  $\epsilon$  is the dielectric constant of the passive film. Dielectric constant is a number related to the ability of a material to carry an alternating current, which represents the relative permittivity of a dielectric material. Factors that influence the capacitive behavior of electrochemical surfaces are the reaction rate, surface roughness and thickness of the film on the surface. According to Equation (3.4), a lower capacity corresponds to a thicker passive film, smaller surface roughness and dielectric constant, all of which may render a passive film more protective and noble. As shown in Figure 3.11, the

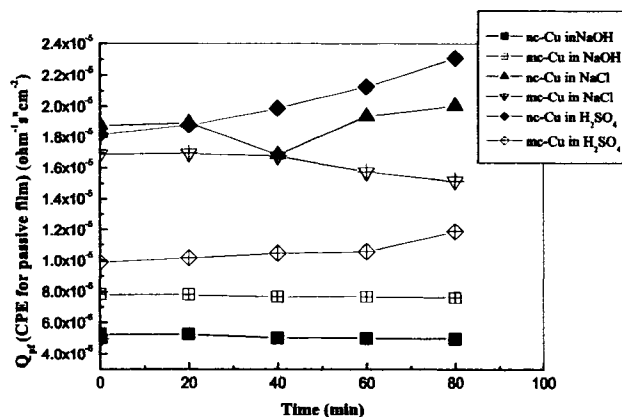


Figure 3.11: Variations in the constant phase element of surface passive film ( $Q_{pf}$ ) with immersion time for nanocrystalline (56nm) and microcrystalline ( $2\mu\text{m}$ ) Cu deposits in different solutions, respectively.

nc-Cu deposit in NaOH had the lowest  $CPE$ , which decreased gradually with the immersion time. However, in the  $\text{H}_2\text{SO}_4$ , the nano-one showed the highest  $CPE$ , which increased with time and the mc-Cu deposit performed better in this solution. The variation trend of  $Q_{pf}$  in the NaCl solution with time was less stable because the chloride ions can penetrate into the metal and damage the surface oxide layer. However, this accelerated dissolution is associated with the repassivation process.

Variations in the charge transfer resistance  $R_{ct}$ , which reflects the resistance of electrons to pass through the double layer during the discharge process, with the immersion time is plotted in Figure 3.12. The discharge process occurred on the electrode surface.  $R_{ct}$  is generally related to a kinetically controlled electrochemical reaction. Usually, a diffusion-controlled impedance, Warburg impedance should be observed in series with the resistance to kinetically controlled reaction, especially at low frequencies where the reactant can diffuse

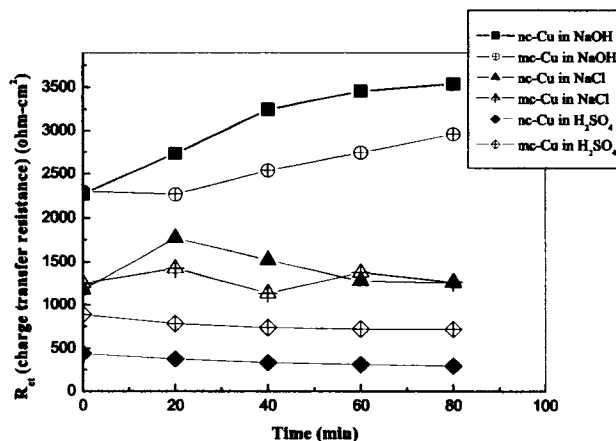


Figure 3.12: Variations in the charge transfer resistance ( $R_{ct}$ ) with the immersion time for nanocrystalline (56nm) and microcrystalline (2 $\mu$ m) Cu deposits in different solutions, respectively.

farther. The charge transfer resistance  $R_{ct}$  was obtained by fitting the experimental EIS data at a high frequency at which the Warburg impedance was small since the diffusing reactants did not move very far. It has been reported that the polarization resistance should include the charge transfer resistance and the diffusive layer impedance in series [76]. If the Warburg impedance can be ignored,  $R_{ct}$  would approximate the polarization resistance. The average  $R_{ct}$  value followed the same order of magnitude as that of polarization resistance  $R_p$  (see Section 3.4) obtained from linear polarization, which is inversely proportional to the corrosion rate. Therefore, comparison of  $R_{ct}$  with the immersion time among different deposits in different solution is meaningful. The nanocrystalline Cu exhibited the highest  $R_{ct}$ , which increased with time before going to a stable state. The increase of  $R_{ct}$  is related to a decrease in the corrosion current density. However, the situation was reversed in the acidic solution, and the performance of the deposits in NaCl was between those in

the  $\text{H}_2\text{SO}_4$  and  $\text{NaOH}$  solutions in terms of the charge transfer resistance.

Variations in the fitting parameter of the capacitance for double layer,  $n_{dl}$ , as a function of time are shown in Figure 3.13. Surface inhomogeneity is the main factor that causes deviation from the ideal capacitive behavior of electrochemical surfaces. Therefore, the value of  $n_{dl}$  can describe the surface roughness caused by corrosion of the electrode. The lower the value of  $n_{dl}$ , the rougher is the electrode surface. The results indicate that the nc-Cu deposit surface was the smoothest after immersion in  $\text{NaOH}$ , but the roughest after immersion in  $\text{H}_2\text{SO}_4$ . The observation was confirmed by morphology analysis from AFM images of nanocrystalline Cu deposits immersed in different solutions for 15 hours, as shown in Figure 3.14.

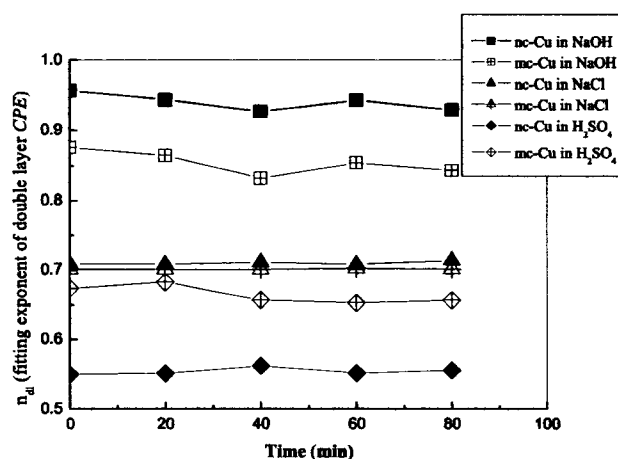


Figure 3.13: Variations in  $n_{dl}$  of the electrochemical double layer with emersion time for nanocrystalline (56nm) and microcrystalline ( $2\mu\text{m}$ ) Cu deposits in different solutions, respectively.

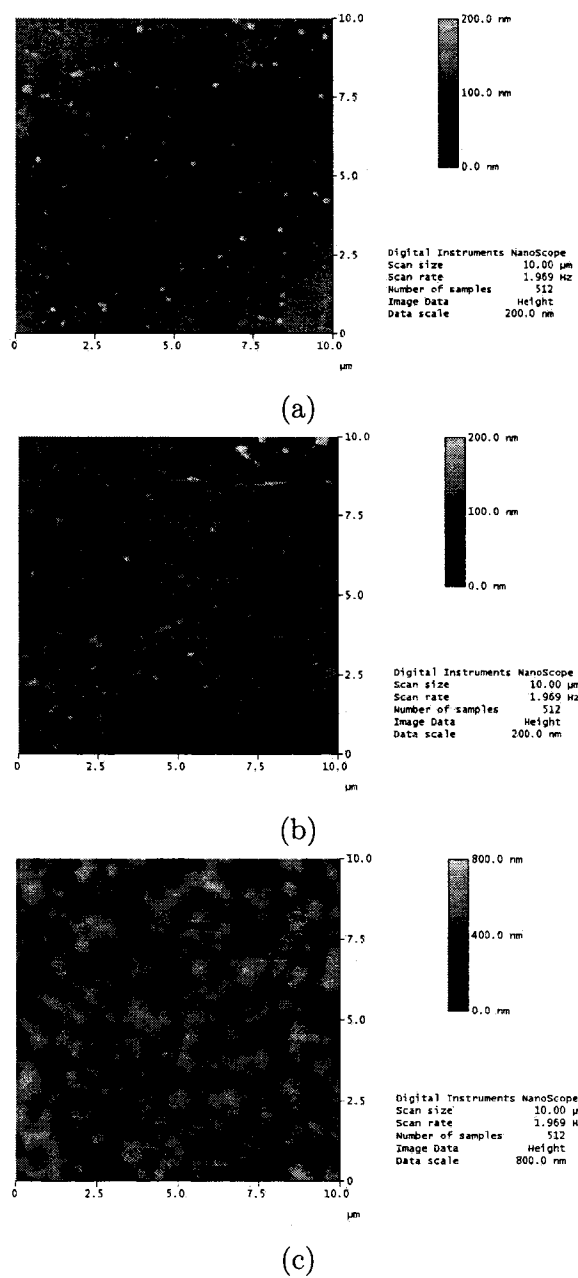


Figure 3.14: AFM morphologies of the nanocrystalline Cu deposit (56nm) in (a) 0.1M NaOH, (b) 3.5wt% NaCl and (c) 1M H<sub>2</sub>SO<sub>4</sub> after immersion for 15 hours.

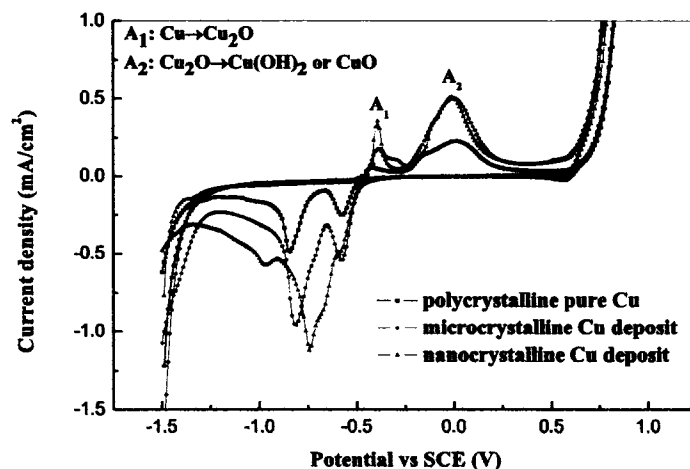


Figure 3.15: Cyclic voltammeteries of nanocrystalline (56nm), microcrystalline (2 $\mu$ m) Cu deposits and polycrystalline pure Cu in 0.1M NaOH solution.

### 3.7 Discussion

Based on the above analysis and discussion, the electrochemical reaction between Cu deposits and the NaOH solution may result in the formation of a compact passive film with high coverage that can protect the metal from corrosion. This may be attributed to the formation of stable cuprite ( $\text{Cu}_2\text{O}$ ) when the pH value of the electrolyte is higher than 5. This oxide has been proven to be the best naturally protective layer for Cu, since it is the most stable type of copper (I) oxide [77, 78, 79]. It is reported that the cuprous oxide ( $\text{Cu}_2\text{O}$ ) plays a role in protection of copper in aqueous media. Kruger [79] has observed that  $\text{Cu}_2\text{O}$  is the only corrosion product for a short immersion time while  $\text{CuO}$  may form over underlying  $\text{Cu}_2\text{O}$  film after a longer immersion period. Hydrated oxides of copper have also been found to form on underlying  $\text{Cu}_2\text{O}$  film as a second component of the oxide film forming in aqueous environments [76].

The cyclic voltammeteries (CVs) of the nanocrystalline and microcrystalline Cu deposits in 0.1M NaOH solution are shown in Figure 3.15. Two peaks can be seen in the anodic region of copper CV curves. The current peak  $A_1$  is related to the formation of a  $Cu_2O$  layer, whereas the current peak  $A_2$  is associated with the anodic formation of a complex hydrous CuO film. CVs can be used to qualitatively diagnose electrode reactions [56]. As shown, the area under peak  $A_1$  of nc-Cu is much greater than that of mc-one, but there is no difference in the area associated with peak  $A_2$ . Therefore, the nanostructure enhanced the formation of  $Cu_2O$ , the strongest oxide among copper oxides. As a result, the passive film formed on nanocrystalline copper was more complete and protective, which is consistent with the lower capacitance value and higher resistance of the nc-Cu deposit. Mechanical properties of the deposits were determined as well (see Chapter 2 and 4). Nano-indentation and nano-wear tests indicated that nc-Cu exhibited much higher hardness and wear resistance, which may be attributed to its stronger passive films to some extent. Scratch experiments (Section 3.5) performed on passive films on nc- and mc- Cu deposits in a NaOH solution showed that the passive film formed on the nanocrystalline deposit had a larger critical load at failure, indicating that its passive film was more adhesive and stronger. Regarding the case of NaCl solution, although a passive film can form in the solution, the high penetration capability of chloride ion makes the situation complicated. It was reported by North and Pryor [78] that the oxide film on copper exposed to 3.4% NaCl consisted of  $Cu_2O$  with traces of  $Cu_2(OH)_3Cl$  on the top of  $Cu_2O$  after a longer immersion time. By incorporation of less stable copper chloride products in relatively stable oxide passive film  $Cu_2O$ , defects are created, which are believed to be the cause for earlier initiation of pitting. As a result, the charge transfer resistance of nc-

Cu increased initially when exposed to the NaCl solution, and then decreased slightly as Figure 3.12 illustrates. This result is also consistent with the pitting morphology of nc-Cu, which shows the formation of a less protective film with pitting sites when in NaCl solution in comparison with that formed in NaOH (see Figure 3.14).

### 3.8 Conclusions

The main conclusions drawn from studies reported in this chapter are:

- Nanostructure with a high density of grain boundaries can make the surface more active, corresponding to poor corrosion resistance. However, if passivation exists, nanostructure accelerates the formation of passive film, thus resulting in a more protective film formed to diminish further corrosion.
- The grain refinement considerably improved passivation of copper deposits in a NaOH solution. The passive film formed on the nanocrystalline copper was stronger and more protective with higher surface electron work function and lower corrosion rate than that formed on microcrystalline copper deposits. However, in the H<sub>2</sub>SO<sub>4</sub> solution without passivation involved, the nanocrystalline copper showed a lower EWF and was less resistant to corrosion.
- There is close correlation between corrosion rate and EWF. The higher the corrosion rate, the lower is the EWF. EWF is a promising parameter to investigate the surface stability and resistance of a material to electrochemical attack.

- The stability of surface films formed on copper deposits with the immersion time in different solutions was studied using EIS analysis. The surface film became thin, relatively rough and less protective on exposure to NaCl and H<sub>2</sub>SO<sub>4</sub> solutions. The polarization resistance increased in the NaOH solution with immersion time, while it decreased in H<sub>2</sub>SO<sub>4</sub>. In the NaCl solution, its variation was not stable. The passive film formed on the nanocrystalline copper deposit in the NaOH solution, which exhibited lower capacitance value and higher resistance, was stronger and more protective than that formed on the microcrystalline deposit.

## CHAPTER 4

### TRIBOLOGICAL PROPERTIES

#### 4.1 Introduction

Tribology, which includes the methodical study of friction, lubrication, and wear, plays a critical role in diverse technological areas. In traditional industries such as automotive and aerospace, tribological studies help increase the lifespan of mechanical components. In the advanced technological industries of semiconductor and data storage, tribological studies become more and more important. In MEMS devices, with the device scale down to ultra-small size, the influence of friction, viscous drag and surface tension markedly increases. Consequently, tribological issues become crucial, because friction and wear affect the device's performance and in some cases, may even prevent devices from working [31]. Many studies have been conducted to develop solid and liquid lubricants and hard films to minimize friction and wear. For example, hard diamond-like carbon (DLC) coatings are used as an overcoat to diminish corrosion and wear of silicon planar head sliders for magnetic disc drives, where wear and friction are an issue because of the close proximity and contact between the slider and disc surfaces during operation [80]. A better understanding of friction and wear could save enormous amounts of energy and money. On the

other hand, friction is not only negative, since it is essential to some mechanical components such as brakes and screws. An important application of wear is nanofabrication using mechanical scratching, when use of chemicals is prohibited. Scanning tunneling microscopes (STMs) and AFMs have been used for nanofabrication by scratching a target surface with a diamond tip [31].

Since copper is widely used in electrical devices, the study of Cu's tribological behaviour is of great importance. In addition, many industrial processes require detailed understanding of tribological processes at the nanometer scale. Assembly of components may depend critically on the adhesion of materials at the nanometer length scale. The investigation of nano-tribology has attracted increasing interest. However, how the nanostructure influences the friction and wear behavior has seldom been studied. This chapter reports our studies on the tribological properties of nanocrystalline copper evaluated using micro-scratch and nano-scratch techniques. Because the nanocrystalline deposit is thin and usually used under light loads, adhesion forces may play an important role in its tribological behavior, which could behave very differently when performed under high loads. The natural passive film on the surface may also influence the friction and wear behavior.

## **4.2 Experimental details**

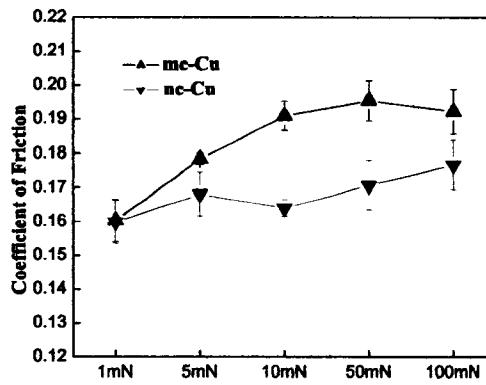
Friction coefficients of the PC- or DC- plated deposits under different loads from 1mN to 100mN were measured using a sharp conical tip (30° cone angle) and a ball tip (diameter 4mm) made of stainless steel, respectively, attached to a universal micro-tribometer. Sliding tests were carried out under a series of normal constant loads at a sliding velocity of 0.05mm/s over a distance of 6mm. During each sliding test, normal force ( $F_N$ ) and lateral force ( $F_L$ ) were

monitored *in situ*. Each coefficient of friction ( $\mu$  or  $\text{COF} = F_N/F_L$ ) was obtained by averaging 5 measurements under the same sliding condition. Micro-scratch track profiles were analyzed using AFM. Volume losses of PC- and DC-plated deposits were determined from the scratch profiles.

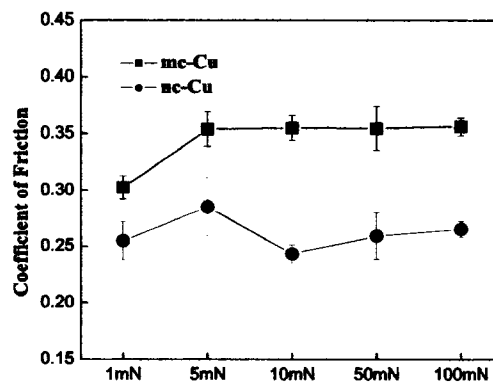
Nano-scratch experiments under light loads were also performed using the Triboscope over a travel distance of  $6\mu\text{m}$  under constant loads of 100, 300 and  $500\mu\text{N}$ . A conical diamond tip with radius of about  $450\text{nm}$  was used. Normal force and lateral force were recorded during the scratch tests. Nano-wear experiments were performed using the Triboscope as well by repeatedly scratching a region of  $500 \times 500\text{nm}^2$  for 5 trace-retrace circles under constant loads of 50 and  $100\mu\text{N}$ , respectively. The wear rate was derived from the wear scar profile.

### 4.3 Friction Behavior

Micro-scratch experiments were performed to evaluate friction properties of nanocrystalline and microcrystalline Cu deposits under relatively large loads from  $1\text{mN}$  to  $100\text{mN}$ . The coefficients of friction (COF) tested using a sharp tip and a ball tip, respectively, under different loads are shown in Figure 4.1. It was demonstrated that the nanocrystalline Cu (grain size:  $56\text{nm}$ ) deposit exhibited much lower COFs than the microcrystalline one (grain size:  $2\mu\text{m}$ ) under all applied loads except the lowest load of  $1\text{mN}$  with the ball tip. The COF of the nanocrystalline Cu deposit was almost 30% lower than that of the microcrystalline one under the sharp tip. As mentioned earlier, the as-deposited PC- and DC-plated deposit surfaces were slightly polished to have similar roughness. The lower COFs of the nanocrystalline Cu deposit can be mainly attributed to the higher hardness due to its smaller grain size. Such



(a)



(b)

Figure 4.1: Coefficients of friction of nc-Cu (56nm) and mc-Cu ( $2\mu\text{m}$ ) deposits with different loads, determined during micro-scratch experiments using: (a) a ball tip, and (b) a sharp tip.

relation is in agreement with conventional friction law [31]. The tribological performance of materials is dependent on the adhesion and mechanical interaction of asperities between surfaces in contact. With higher resistance to deformation, a harder metal exhibits a smaller penetration depth against mechanical attack and thus reduces both the plowing effect and the contact area, resulting in less friction. However the reduction of the COF by nanocrystallization was less marked when the applied load was small, e.g., 1mN under ball tip. In this case, the contact stress could be too small to lead to significant difference in COF between the nanocrystalline and microcrystalline deposits. This could also explain the smaller difference in COF between these two types of deposits and their lower COFs under the ball tip. The friction behavior under light loads was further evaluated using nano-scratch experiments using a nano-mechanical probe (Triboscope) under applied loads of 100, 300 and 500 $\mu$ N, respectively. The measured COFs are shown in Figure 4.2, which also illustrates typical profiles of the scratched surfaces. It is interesting to notice that under 300 and 500 $\mu$ N, the COFs of nanocrystalline Cu coating are a little higher than that of the microcrystalline one, whereas under 100 $\mu$ N, the COFs are similar.

According to the tribological mechanism [81], friction is caused by two main factors, adhesion and mechanical interlock and thus friction coefficient can be separated into two components, adhesion and deformation correspondingly. The adhesive force comes from the chemical interaction and the mechanical force involves asperity-plowing and deformation. Under light loads the adhesion plays a main role in generating frictional force, while under high loads the mechanical action is predominant.

Considering that under ultra light loads adhesion becomes predominant in

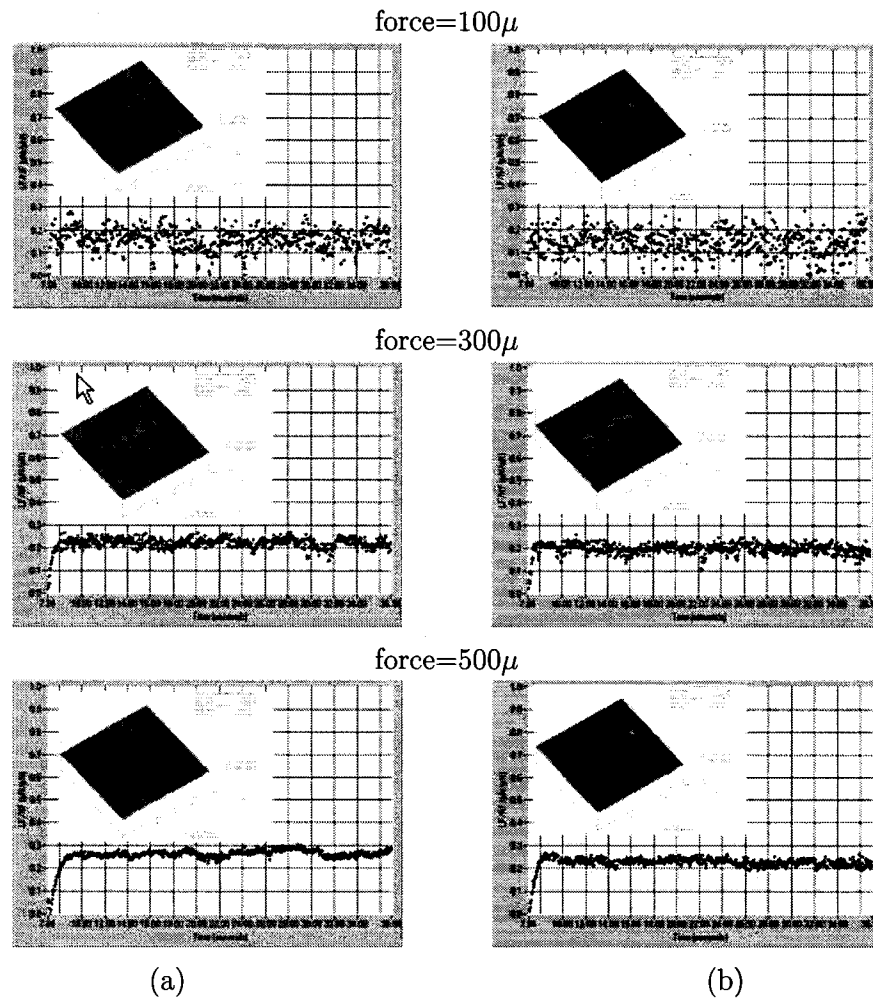


Figure 4.2: Plots of the lateral force vs. normal force during nano-scratch as the tip was moved across the specimen surface under different applied loads, respectively: (a) nc-Cu (56nm) deposit, and (b) mc-Cu ( $2\mu\text{m}$ ) deposit. (The insets show typical AFM images of scratch tracks; the scratch length is  $6\mu\text{m}$ .)

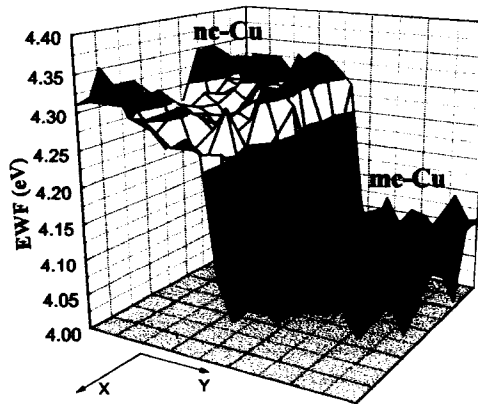


Figure 4.3: EWFs of nanocrystalline (56nm) and microcrystalline (2mm) Cu deposits with natural passive film.

friction [50], a higher adhesive force may occur between nanocrystalline Cu and the probe when the natural passive film is damaged. In the above-mentioned scratch tests, the passive film could be damaged, since the scratch penetration was about 25nm at  $500\mu\text{N}$ , larger than the thickness of natural passive film on Cu deposit. The high-density of grain boundaries on the nanocrystalline deposit made surface electrons more reactive, thus leading to larger adhesion and friction. However, the scratch penetration under  $100\mu\text{N}$  is about several nanometers, so the friction could be mainly affected by the passive film, which minimizes the difference in COF between the nc- and mc-deposits. When the contact stress was largely increased such as in the case of micro-scratch test, the hardness became predominant, the nanocrystalline coating showed lower COFs than the microcrystalline one as shown in Figure 4.1.

The EWF of nanocrystalline copper deposit with natural passive film was higher than that of microcrystalline one, which was schematically shown in Figure 4.3. Under light load, the intrinsic adhesion depends on atomic inter-

action, which is largely determined by the surface electronic behavior. Recent studies have demonstrated that lower EWF reflects higher activity of electrons that can make the adhesive force larger [53]. Therefore, the adhesion force of the nc-Cu deposit with passive film should be lower than mc-Cu, but when the passive film is damaged under large loads, it should be higher. Under ultra-light loads, the presence of the passive films cannot be ignored when considering the adhesion force.

#### 4.4 Wear Behavior

Figure 4.4 shows the micro-wear test results of mc- and nc-deposits scratched by a tungsten sharp tip (UMT) respectively under a series of normal constant loads from 1 to 10mN at a velocity of 0.05mm/s over a total sliding distance of 6mm. The wear volume loss was calculated from the cross-sectional profiles determined using AFM. Apparently, the wear volume loss of the nc-Cu deposit was approximately half that of the mc-Cu deposit. According to the classical theory of wear, the volume loss,  $V_m$ , is given by Archard's Law [82]:

$$V_m = K_w \frac{F_N L}{H} \quad (4.1)$$

where,  $K_w$  is the wear coefficient,  $F_N$  is the applied normal force,  $L$  is the sliding distance and  $H$  is the hardness of the material. The numerical value of wear coefficient  $K_w$  depends on the material removal mechanism [83]. From Equation (4.1), the wear volume loss rate should be inversely proportional to the hardness of the material. Therefore, the enhancement of the wear resistance of nanocrystalline deposits is mainly attributed to its increased hardness. The higher hardness decreased the contact area and asperity penetration. As

a result, the mechanical ploughing effect and total adhesive force could be reduced, thus diminishing the wear damage. In practice, the hardness criterion is often used for selecting wear resistance materials.

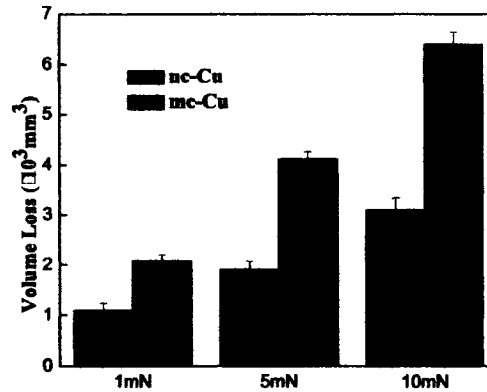
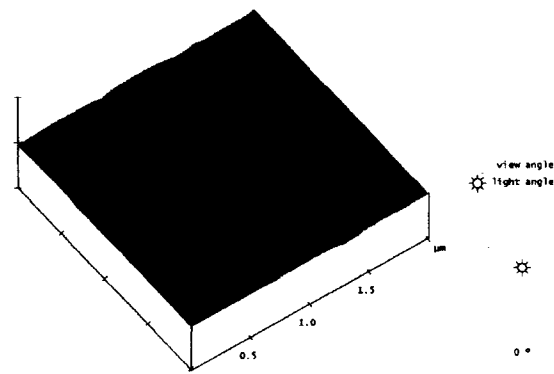
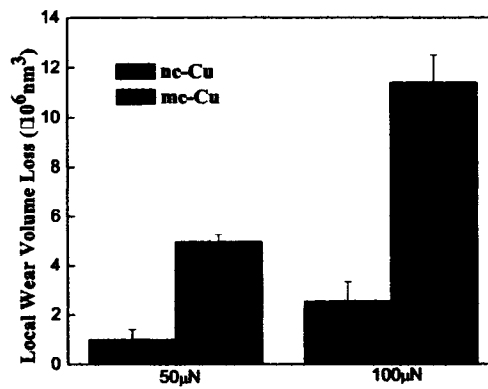


Figure 4.4: Wear volume losses of nc-Cu (56nm) and mc-Cu (2 $\mu$ m) deposits determined during micro-scratch tests.

The nano-wear test, which reflects the resistance of a material to local wear, was also carried out using the Triboscope, in which a reciprocating tip scratching a small area of 500 $\times$ 500nm<sup>2</sup> region under constant loads of 50 and 100 $\mu$ N, respectively. A typical image of wear track is shown in Figure 4.5(a). Experimental results under these ultra light loads are presented in Figure 4.5(b). It is demonstrated that the nc-Cu deposits exhibited a much higher resistance to local wear than mc-Cu. Although the grain size had been found to cause a little difference in COFs between nc- and mc-Cu deposits under light loads, a much more pronounced effect on nano-wear resistance was observed, since the wear resistance is mainly dependent on the mechanical behaviour. The local wear on very fine scales is sensitive to many factors, such as surface roughness, local structure, thickness and adhesion of natural oxide film [31]. Therefore,



(a)



(b)

Figure 4.5: Local wear tests of nc-Cu (56nm) and mc-Cu ( $2\mu\text{m}$ ) deposits under light loads determined during nano-scratch tests: (a) a typical image of a nano-wear track; (b) local wear volume losses.

the higher grain boundary density and the resultant stronger and more adherent passive film on nanocrystalline Cu coatings are also responsible for the enhancement in the resistance to local wear.

#### 4.5 Conclusions

The main conclusions drawn from studies reported in this chapter are:

- Under large loads, the friction coefficient of the nc-Cu deposit was much lower than that of the mc-one due to its higher hardness caused by the nano grain size.
- Under light loads, the adhesive force plays a main role in friction. The increased friction coefficient of the nc-Cu deposit should result from its higher surface electronic activity caused by its increased grain boundary density.
- Under ultra-low loads, the difference in the friction coefficient between the nc-Cu deposit and mc-one was minimized due to the presence of passive film.
- The nc-Cu deposit exhibited higher resistance to wear and a more pronounced enhancement in the resistance to local wear.

## CHAPTER 5

### SYNERGISM OF CORROSION AND WEAR

#### 5.1 Introduction to Synergism of Corrosion and Wear

Corrosion and wear often occur simultaneously in industry. The corrosion-wear interaction plays an important role in many industrial processes, during which industrial facilities suffer from wear in a corrosive environment. Typical examples are slurry pumps used in the oil sands industry, orthopedic implants, food processing and mining equipment [84, 85, 86]. During corrosive wear, plastic deformation makes the target surface more anodic and thus accelerates material dissolution [41]. On the other hand, corrosion degrades the surface with formation of pitting sites, brittle oxides or porous layers. The changes of surface structure in corrosive media decrease the resistance to mechanical attack and as a result, wear is accelerated by corrosion. Such synergistic attack of corrosion and wear can result in a high rate of material removal. The interaction between corrosion and wear has, however, found beneficial application in the semiconductor industry. Corrosive wear is needed for the chemical-mechanical planarization (CMP) of interconnects for multilevel metallization in advanced integrated circuits [87, 88]. This process uses the action of chemical dissolution coupled with mechanical polishing materials to remove

extensive deposited material to make interconnects on electronic chips.

The mutual effects of mechanical and electrochemical actions in corrosive wear have attracted increasing interest recently. Many efforts have been made to develop experimental techniques to investigate the interaction between corrosion and wear. Jiang [89] investigated the effect of wear on corrosion of austenitic stainless steels in sulfuric acid solution using a pin-on disc apparatus. Schmutz and Frankel [90] used AFM as scratching devices to locally remove passive film of aluminum alloys. Noel [91] evaluated the synergistic effect of abrasion and corrosion on wear of low alloy steel using a pin-on abrasive belt machine. Mishler et al. [92] investigated the effect of sulfuric acid concentration on the tribocorrosion rate of iron using a reciprocating motion tribometer. A number of authors have investigated the effect of electrochemical action on the wear behavior by imposing a fixed potential on the rubbing surface. Abd-el-kader and El-Raghy [93, 94] studied wear behavior of stainless steel in chloride medium under different applied potentials and found that wear was merely mechanical with cathodic protection; at anodic potentials, chemical reactions lead to a wear rate almost as twice that under cathodic protection. However, corrosive wear is a complex process. It was observed that cathodic polarization of titanium led to increased wear due to hydrogen embrittlement so that the mechanical wear rate is not necessarily equal to that observed under cathodic polarization [95]. How the mechanical and electrochemical actions contribute to the material removal during corrosive wear, especially how nanocrystallization influences these contributions, are not well clarified. In this work, an electrochemical scratch method was used to investigate the synergistic attack of corrosion and wear on nanocrystalline and microcrystalline Cu deposits in different solutions.

## 5.2 Fundamentals of the Analysis Method

During corrosive wear, the total volume loss rate ( $r_{total}$ ) includes three components, which are the rates of volume losses caused by pure wear ( $r_w$ ), by pure corrosion ( $r_{corr}$ ) and by their synergistic attack ( $r_{syn}$ ), respectively [41, 42]. The total wear volume loss rate is expressed as:

$$r_{total} = r_w + r_{corr} + r_{syn} \quad (5.1)$$

The synergism caused by corrosion and wear consists of two parts, the increase in wear rate due to corrosion ( $r_{c-w}$ ) and the increase in corrosion rate due to wear ( $r_{w-c}$ ):

$$r_{syn} = r_{c-w} + r_{w-c} \quad (5.2)$$

For a mechanistic interpretation of corrosive wear, one must distinguish material loss caused by corrosion from that caused by mechanical wear. The electrochemical scratch method used is very suitable for study the synergism of corrosion and wear in sliding contact to distinguish mechanical and electrochemical contributions. Using this method, one may determine *in situ* the amount of metal turned into oxide or dissolved based on changes in electrochemical current during scratch. The electrochemical scratch technique has been widely used to study the kinetics of passivation of metal surfaces activated by scratching [96, 97]. When a metal surface is scratched in a corrosive medium, there is a significant increase in current due to the increased dissolution of the target metal. During the scratch, fresh and deformed (thus more anodic) surface is generated, which is exposed to the corrosive environment and accelerates the corrosion rate by making the surface more anodic. This

is also very destructive if the metal can form a thin protective passive film in solution. Once the passive film is damaged, the enhancement of corrosion by wear will be more obvious. When the scratch is completed, the current decreases gradually due to the repassivation of the damaged area. Schematic changes in current with time during the electrochemical scratch are illustrated in Figure 5.1.

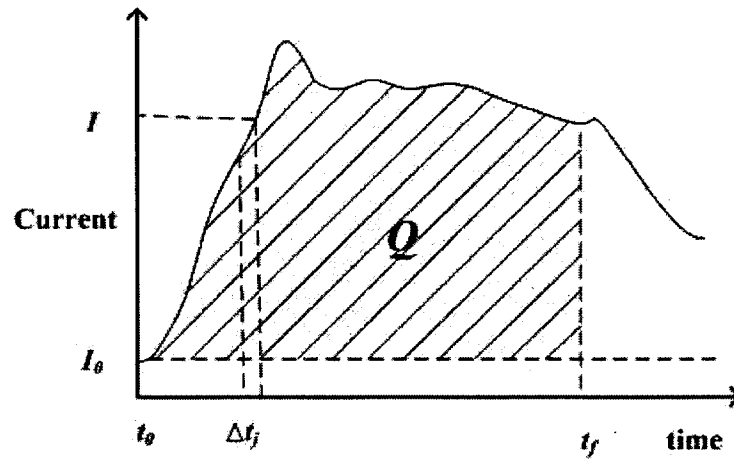


Figure 5.1: A schematic illustration of the changes in current with time during electrochemical scratch.

The increased quantity of electrical charge  $Q$  can be determined by integrating the measured current  $I$  over the time interval of the experiment, which is equal to the area under the current-time curve:

$$Q = \int_{t_0}^{t_f} (I - I_0) dt \quad (5.3)$$

where,  $t_0$  and  $t_f$  are the starting time and finishing time of scratch, respectively;  $I$  is the current and  $I_0$  is the current prior to scratch.

The volume loss caused by wear-accelerated corrosion could be determined from the measured current using Faraday's law:

$$V_{w-c} = \frac{QM}{n\rho F} \quad (5.4)$$

where,  $V_{w-c}$  is the increment of dissolved volume of metal caused by wear-assisted corrosion;  $n$  is the number of valence electrons of a metal under study;  $\rho$  is the density of metal,  $M$  is the atomic mass of the metal and  $F$  is the Faraday constant. The average additional corrosion rate due to wear,  $r_{w-c}$ , is equal to the ratio of  $V_{w-c}$  to the scratch time interval,  $t_f-t_0$ .

The total volume loss rate ( $r_{total}$ ) can be determined by measuring the volume of the wear scar or scratch groove after the scratch experiment. Profilometer and AFM, can be used to measure the dimensions of the wear track.

The volume loss rate caused by static corrosion ( $r_{corr}$ ) can be determined from the corrosion rate without wear involved [42]. The pure corrosion rate may be calculated using Equation (3.1). More discussion about corrosion rate has been given in Chapter 3. The pure volume corrosion rate is expressed as:

$$r_{corr} = \frac{i_{corr}SM}{n\rho F} \quad (5.5)$$

where,  $S$  is the area of a sample exposed to a corrosive solution. For the purpose of separating the extra-corrosion due to scratch from the total volume loss,  $S$  can be thought of as the fresh surface area generated by scratch. If the length of scratching groove  $l$ , and the cross-sectional profile  $a$  are determined, the  $S$  can be approximately calculated from the scratch dimensions.

The volume loss rate measured under cathodic protection is generally regarded as the rate of pure mechanical wear loss ( $r_w$ ) [98, 99]. Under cathodic protection, the corrosion component  $r_{corr}$  during the scratching process would be inhibited. However, this is only true for some alloy systems. Problems may

arise when the material is sensitive to hydrogen. In this case, the wear loss may increase with increasing magnitude of applied cathodic potential due to hydrogen embrittlement. Some researchers have been seeking suitable inhibitors to inhibit the corrosion component [100]. Since pure water is not a corrosive media, the wear loss measured in water may be adopted approximately as pure mechanical wear loss for some alloy system.

From the rate of total volume loss ( $r_{total}$ ), the volume loss rates caused by pure wear ( $r_w$ ) and pure corrosion ( $r_{corr}$ ), the volume loss rate caused by the corrosion-wear synergism ( $r_{syn}$ ) can be calculated:

$$r_{syn} = r_{total} - r_w - r_{corr} \quad (5.6)$$

If the wear accelerated corrosion volume loss rate  $r_{w-c}$  is determined using the electrochemical scratch method, the material volume loss rate caused by corrosion-assisted wear can thus be determined.

$$r_{c-w} = r_{syn} - r_{w-c} \quad (5.7)$$

It should be noted that the response time of the electrochemical reaction is larger than the scratch time as shown in Figure 5.1. It is therefore important to accurately determine the finishing time ( $t_f$ ).

### 5.3 Experimental Details

The contributions of mechanical and electrochemical actions during corrosive wear in different solutions, 0.1M NaOH, 3.5wt%NaCl and 1M H<sub>2</sub>SO<sub>4</sub>, were investigated using the electrochemical scratch method. As schematically illustrated in Figure 5.2, the electrochemical scratch system included two com-

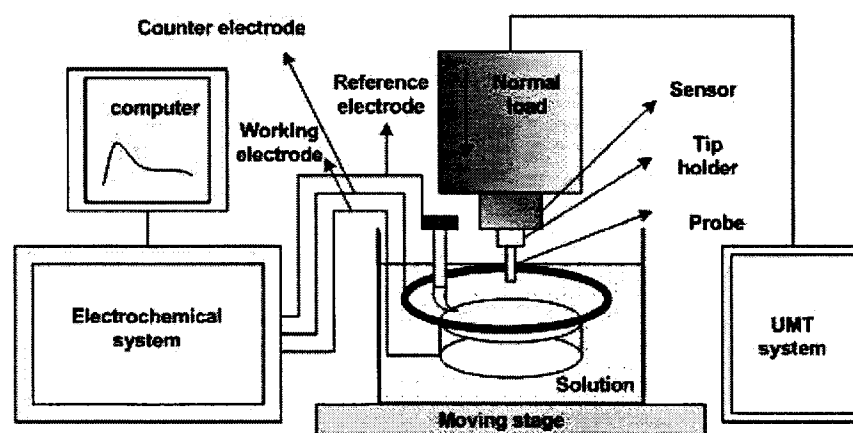


Figure 5.2: Schematic illustration of electrochemical scratch system.

ponents, a mechanical sub-system used to scratch a target surface and an electrochemical sub-system used to control the applied potential and monitor the changes in current. In the mechanical sub-system, a diamond probe was employed to scratch the sample surface immersed in a solution under a constant load. The shape of the diamond tip is shown in Figure 5.3. During scratching, the variations in current caused by the scratch were monitored *in situ*. Three-electrode cell was used with the copper deposit surface as the working electrode. The wear volume loss caused by wear-accelerated corrosion was calculated from the area under the current-time curve ( $Q$ ) as illustrated in Figure 5.1. Two different loads, 20g and 40g were applied. The scratch was carried out at velocity of 5mm/s for a period of one second. The electrochemical scratch tests were performed under two applied potentials, corrosion potential ( $E_{corr}$ ) and a cathodic potential, respectively. The wear volume loss determined under cathodic protection was regarded as pure wear. A potential of -0.2V (see next section) relative to  $E_{corr}$  was used as the cathodic potential. After scratching, the specimen was dried immediately. The topographic

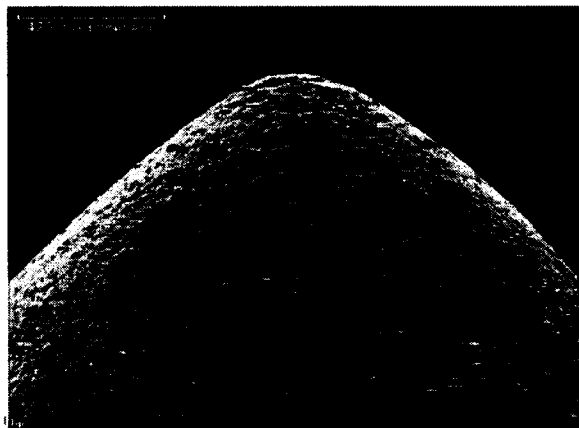


Figure 5.3: The shape of the diamond tip used in the electrochemical scratch experiment.

profile of the scratch grooves was characterized using AFM, which is ideal for three-dimension imaging. The wear volume losses caused by pure wear were obtained from cross-sectional profiles of the grooves. Figure 5.4 illustrates a typical cross-sectional profile of a few scratch grooves on the copper deposit.

#### 5.4 Results

Electrochemical scratch tests under the free corrosion potential were performed in different solutions. The variation of current was monitored and recorded during the scratch process. Figure 5.5 illustrates the variation in current with scratching time for nanocrystalline and microcrystalline Cu deposits. The scratch was carried out under a load of 20g in 0.1 M NaOH solution. It was observed that the current increased rapidly when the scratch was started. The increases in current arise from the additional corrosion caused by wear. As has been mentioned, the scratch groove can make the surface more anodic due to associated dislocations/plastic deformation and generate larger area exposed

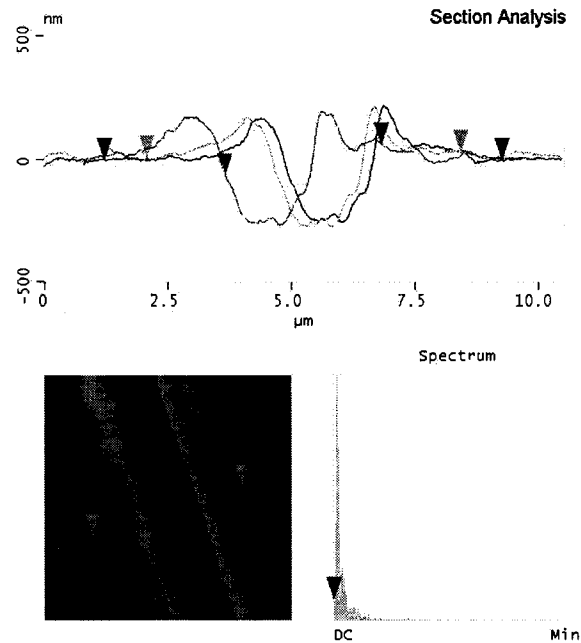


Figure 5.4: Typical cross-sectional profiles of scratched grooves on the Cu deposits and corresponding AFM image.

to the corrosive medium. Therefore, the increased quantity of electrical charge  $Q$ , which is equal to the area under the current-time curve between the starting time and finishing one, can be used to determine the volume loss of corrosion accelerated by wear using Faraday Law. Similar changes of current were observed in different solutions when scratched under loads of 20g and 40g. The calculated volume loss rates ( $\mu\text{m}^3/\text{s}$ ) of wear-assisted corrosion  $r_{w-c}$  are listed in Table 5.1 and Table 5.2.

The total volume loss rate ( $r_{total}$ ), was determined from the cross-sectional profile of the scratch groove obtained from the AFM images. The volume loss rate caused by pure corrosion ( $r_{corr}$ ) was determined from the corrosion

Table 5.1: Volume loss rates ( $\mu\text{m}^3/\text{s}$ ) of nanocrystalline (56nm) and microcrystalline ( $2\mu\text{m}$ ) Cu determined by electrochemical scratch technique under a load of 20g, at a scratch velocity of 5mm/s in different solutions.

		$r_{total}$	$r_w$	$r_{corr}$	$r_{syn}$	$r_{c-w}$	$r_{w-c}$
NaOH	nano	3215	2410	0.0043	805.00	804.74	0.258
	micro	5004	3842	0.0105	1161.99	1161.10	0.89
NaCl	nano	3850	2509	0.0082	1340.99	1335.84	5.15
	micro	5580	3859	0.0121	1720.99	1714.87	6.12
H <sub>2</sub> SO <sub>4</sub>	nano	3948	2486	0.0309	1461.97	1455.55	6.42
	micro	5632	3796	0.0132	1835.99	1833.41	2.58

Table 5.2: Volume loss rates ( $\mu\text{m}^3/\text{s}$ ) of nanocrystalline (56nm) and microcrystalline ( $2\mu\text{m}$ ) Cu determined by electrochemical scratch technique under a load of 40g, at a scratch velocity of 5mm/s in different solutions.

		$r_{total}$	$r_w$	$r_{corr}$	$r_{syn}$	$r_{c-w}$	$r_{w-c}$
NaOH	nano	5768	4508	0.0043	1260.00	1257.77	2.23
	micro	9441	7153	0.0105	2287.99	2286.22	1.77
NaCl	nano	6123	4692	0.0082	1430.99	1395.58	35.41
	micro	9848	7383	0.0121	2464.99	2446.21	18.78
H <sub>2</sub> SO <sub>4</sub>	nano	6357	4655	0.0309	1701.97	1655.83	46.14
	micro	9459	7298	0.0132	2160.99	2136.77	24.22

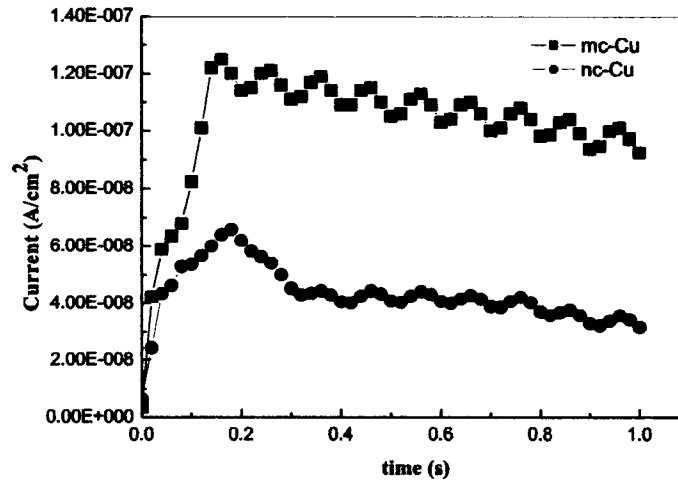
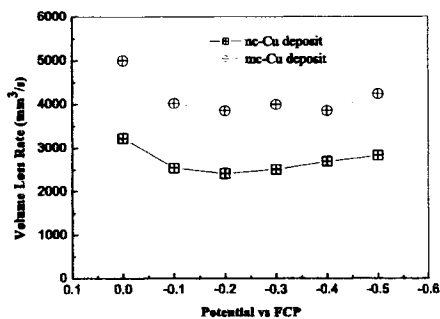


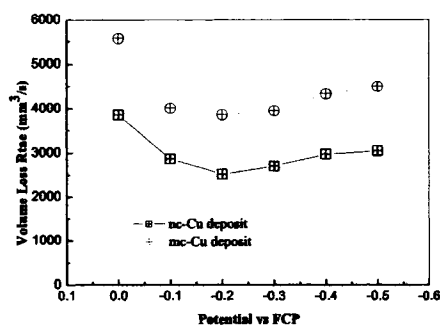
Figure 5.5: Variation in current during the electrochemical scratch (load=20g) of nanocrystalline (56nm) and microcrystalline ( $2\mu\text{m}$ ) Cu deposits in 0.1 M NaOH solution.

rate obtained from the polarization test. All results are shown in Table 5.1 and Table 5.2. More about the calculation process can be found in previous section.

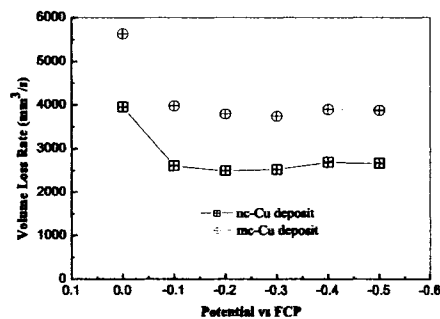
The wear removal rate of a metal scratched at a cathodic potential in the same solution may be approximately regarded as pure wear without corrosion involved, because the corrosion is inhibited under cathodic protection. Since mechanical material removal can be enhanced by corrosion in corrosive medium, it is better to use sufficient cathodic potential to inhibit corrosion. However, large cathodic potential may attract more hydrogen, leading to hydrogen embrittlement, which, in turn, decreases the wear resistance of the metal. As a result, the wear loss may increase with an increasing magnitude of cathodic potential. Therefore, it is necessary to select a proper cathodic potential to determine the pure wear volume loss rate. In this study, the elec-



(a)



(b)



(c)

Figure 5.6: The volume loss rates of the nanocrystalline (56nm) and microcrystalline (2 $\mu$ m) Cu deposits scratched at different cathodic potentials in 0.1M NaOH (a), 3.5wt% NaCl (b) and 1M H<sub>2</sub>SO<sub>4</sub> (c).

trochemical scratch experiments were carried out using a series of cathodic potentials from 0 to -0.5V relative to  $E_{corr}$ . The nanocrystalline and microcrystalline copper deposits were scratched under a load of 20g in NaOH, NaCl and H<sub>2</sub>SO<sub>4</sub>. The volume loss rates were determined from the scratch grooves and the results are illustrated in Figure 5.6. From the curves of volume loss rates versus potential, one may see that the wear volume loss rates were highest at free corrosion potential, indicating that the synergism of corrosion and wear was significant. The material removal rate showed a minimum when tested for all three solutions. In the region around -0.2V relative to  $E_{corr}$ , the volume loss rates were lower for all the three solutions, which was used in this study to evaluate the pure wear in different solutions. It should be noticed from Figure 5.6 that under the cathodic potential of -0.2V, the material loss rates of the nano-one or micro-one showed similar trend in the different solutions. This implies that under cathodic protection, the observed mechanical wear should be relatively independent of the electrolyte used. Here, we assume that the dilute solutions, 0.1M NaOH, 3.5wt% NaCl and 1M H<sub>2</sub>SO<sub>4</sub> had comparable viscosity.

Using the Equations (5.1) to (5.7) and scratched groove dimensions, all defined volume loss rates ( $\mu\text{m}^3/\text{s}$ ),  $r_{total}$ ,  $r_w$ ,  $r_{corr}$ ,  $r_{syn}$ ,  $r_{w-c}$ ,  $r_{c-w}$  of nanocrystalline and microcrystalline copper deposits in different corrosive media, were determined. Results obtained under a load of 20g are given in Table 5.1 and those under a load of 40g are shown in Table 5.2.

### 5.5 Synergistic Effect of Corrosion and Wear

According to Table 5.1 and Table 5.2, the total volume losses and pure wear volume losses of nanocrystalline copper were much lower than those of mi-

Table 5.3: The ratios of volume loss rates caused by corrosion, wear and synergism.

Load(g)		20		
	ratio	$r_{syn}/r_{total}$	$r_{c-w}/r_w$	$r_{w-c}/r_{corr}$
NaOH	nano	0.25	0.33	60.00
	micro	0.23	0.30	84.76
NaCl	nano	0.35	0.53	628.05
	micro	0.31	0.44	505.79
H <sub>2</sub> SO <sub>4</sub>	nano	0.37	0.59	207.77
	micro	0.33	0.48	195.45
Load(g)		40		
	ratio	$r_{syn}/r_{total}$	$r_{c-w}/r_w$	$r_{w-c}/r_{corr}$
NaOH	nano	0.22	0.28	518.60
	micro	0.24	0.32	168.57
NaCl	nano	0.23	0.30	4318.29
	micro	0.25	0.33	1552.07
H <sub>2</sub> SO <sub>4</sub>	nano	0.27	0.36	1493.20
	micro	0.23	0.29	1834.85

crocrystalline one under both of the applied loads. The increased hardness of nanocrystalline copper caused by finer grains is the cause of higher wear resistance. Moreover,  $r_{total}$  and  $r_w$  were on the same order of magnitude, while  $r_{corr}$  was much lower, implying that the mechanical attack made a predominant contribution to the total corrosive wear. However, although the volume loss rates caused by corrosion were about five orders of magnitude lower than those caused by mechanical wear, the synergistic interaction between corrosion and wear greatly increased the material loss by more than 20% relative to the total volume loss. The ratios of  $r_{syn}/r_{total}$ ,  $r_{c-w}/r_w$  and  $r_{w-c}/r_{corr}$  of nanocrystalline

and microcrystalline Cu deposits scratched under 20g and 40g, respectively, are given in Table 5.3. The contribution of corrosion-wear synergy to the total material loss shows appreciable difference in different corrosive media under the load of 20g. It was shown that the ratio,  $r_{syn}/r_{total}$  is the lowest in the NaOH solution and the highest in the  $H_2SO_4$  solution, indicating that the contribution of corrosion-wear synergism to the total volume loss increased when scratched in the solution with higher corrosivity. As discussed in Chapter 3, the copper deposits corroded fast in  $H_2SO_4$  and NaCl solutions, compared to that in NaOH solution, in which a protective passive film can form on the deposit surface. However, the situation changed under the higher load of 40g. As shown in Table 5.3, under 20g,  $r_{syn}$  was in the range of 25%-33% of  $r_{total}$  and the ratio increased as the corrosivity increased. Under the higher load of 40g, the ratio decreased. This happened because under high loads, the mechanical action usually dominates corrosive wear processes. In addition, in the same environment, there was no large difference between the nanocrystalline and microcrystalline copper deposits in terms of the contribution of the synergistic effect to the total volume loss. Although the synergistic volume loss rate,  $r_{syn}$  of nc-Cu was much lower than those of mc-Cu due to its higher hardness of nanostructure, the  $r_{syn}/total$  appeared not to depend greatly on the microstructure of materials.

#### **Mechanical effect on corrosion during corrosive wear**

The synergism of corrosion and wear played an important role in corrosive wear. As shown, the material loss rate caused by wear-accelerated corrosion  $r_{w-c}$  was two or three orders of magnitude lower than the material loss rate caused by corrosion-accelerated wear  $r_{c-w}$ . However,  $r_{w-c}$  is significantly

greater than the static corrosion rate  $r_{corr}$ . The ratio of  $r_{w-c}/r_{corr}$  was much greater than 1 as shown in Table 5.3, indicating that corrosion is significantly enhanced by wear and this enhancement of corrosion by wear increased with increasing load. (It should be mentioned that during the scratch process, fresh surface is generated in the groove when the tip has just passed by. Therefore, the volume loss rate caused by wear-accelerated corrosion may include part of pure corrosion. Since the whole duration of the scratch process was only 1s and the  $r_{w-c}$  was much greater than  $r_{corr}$ , the contribution of the pure corrosion caused by the fresh groove exposed to the corrosive medium during corrosive wear was neglected in the present study.) One may see in Table 5.3 that the ratio of  $r_{w-c}/r_{corr}$  of nc-Cu deposit under 20g was lower than that of mc-one in NaOH, but higher in NaCl and H<sub>2</sub>SO<sub>4</sub>. However, the situation changed when scratched under the high load of 40g. As shown, the ratio of  $r_{w-c}/r_{corr}$  of nc-Cu was higher in NaOH and NaCl but lower in H<sub>2</sub>SO<sub>4</sub> under 40g. It has been discussed in Chapter 4 that the nanocrystalline Cu deposit exhibited better corrosion resistance in NaOH solution than the microcrystalline one because of its more protective passive film. However, when there was no effective passive films formed in H<sub>2</sub>SO<sub>4</sub>, nanocrystalline Cu deposits corroded faster due to its high density of grain boundaries. Therefore, under relatively low loads, the mechanical attack may not make a large contribution to the corrosion, especially for the nanocrystalline Cu surface which had higher hardness and a stronger passive film in NaOH solution. However, when the load increased, mechanical attack began to dominate the whole process and damaged the passive films, leading to acceleration of the corrosion process. As a result, the nanocrystalline surface may have a larger  $r_{w-c}/r_{corr}$  ratio, in which passivation existed, in NaOH and NaCl solutions at the higher load.

But in  $\text{H}_2\text{SO}_4$ , its ratio  $r_{w-c}/r_{corr}$  was lower, because in this solution the  $r_{corr}$  of nc-Cu is already very high and then Cu cannot form a protective passive film, which reduced the  $r_{w-c}/r_{corr}$  not as high as those observed in NaOH and NaCl solutions.

Wear significantly accelerated the corrosion dissolution mainly due to the following reasons. 1)Wear generated surface irregularities, such as wear scar with asperities that make the surface electrons more active [48]; 2)wear increased plastic deformation and the density of dislocations which can decrease the electrochemical stability of a metal and thus accelerate corrosion [52]; 3)wear damaged the protective passive or adsorptive film and consequently accelerated surface electrochemical reactions, thus resulting in an increased corrosion rate.

#### **Electrochemical effect on wear during corrosive wear**

When a material is subjected to wear in a corrosive environment, the degradation of surface caused by corrosion can significantly accelerate the material removal by wear. Generally, corrosion occurs preferentially at surface irregularities, or occurs inhomogeneously on the surface at a microscopic level. The resultant surface pits, asperities and other surface defects could act as stress raisers to surface failure. Non-stable or porous corrosion products also facilitate the material removal. The volume loss rate caused by corrosion-accelerated wear ( $r_{c-w}$ ) made a great contribution to the total volume loss rate as shown in Table 5.1 and Table 5.2.  $r_{c-w}$  was much larger than the volume loss rate caused by corrosion-accelerated wear ( $r_{w-c}$ ) and was therefore the predominant factor in the synergism of corrosion and wear, which increased with increasing load. The nanocrystalline Cu deposit showed lower  $r_{c-w}$  value.

The rank of  $r_{c-w}$  was in good agreement with that of  $r_w$ , indicating that the mechanical behavior of the target material played a main role in resisting corrosive wear. As shown in Table 5.3, the ratio ( $r_{c-w}/r_w$ ) was influenced by the corrosivity of the environment. Under a load of 20g, nanocrystalline deposit exhibited higher  $r_{c-w}/r_w$  and this ratio increased with the aggressiveness of solutions. But under the higher load of 40g, no appreciable difference was found in  $r_{c-w}/r_w$  between nc-Cu and mc-one in different solutions, indicating that the electrochemical action played a relatively minor role in the present situation. The enhancement of electrochemical action to wear is more pronounced at the low load than that at the high load where the mechanical action dominates. Therefore, at the low load, harder nc-Cu had lower wear volume loss leading to higher ratio of  $r_{c-w}/r_w$  than mc-Cu, but this difference is diminished at the high load.

## 5.6 Conclusions

Corrosive wear, which involves mechanical and electrochemical attack and synergy can cause significant material loss. In this work, the synergistic effect of corrosion and wear on nanocrystalline and microcrystalline copper deposits was investigated using an electrochemical scratch technique:

- An experimental method was proposed to determine the mechanical and electrochemical contributions to the total material loss during corrosive wear. The contribution of wear-accelerated corrosion to the total material removal can be determined by a simple current measurement during scratch process. The pure mechanical contribution can be determined by performing a wear test under cathodic polarization. It should be noticed that excessive cathodic potential may lead to hydrogen embrit-

tlement and increase the material removal. According to the model, the volume loss rate caused by static corrosion, mechanical wear and the corrosive wear synergism, including corrosion-accelerated wear and wear-accelerated corrosion can be determined.

- The synergism of corrosion and wear leads to considerable material degradation. In the absence of corrosion, an inverse relation between wear rate and hardness has been observed. In the presence of corrosion, the hardness is no longer the only crucial governing factor. The present study indicated that the mechanical action still dominated the total material loss during corrosive wear. The synergistic effect of corrosion and wear depended on the material structure, the corrosivity of environment, the electrode potential and applied load. Corrosion can be enhanced significantly by mechanical attack. Under high loads, the ratio of  $r_{w-c}/r_{corr}$  of nc-Cu was higher in NaOH with passivation involved but lower in H<sub>2</sub>SO<sub>4</sub> without passivation. However, the situation was reversed under lower loads.
- The wear-accelerated corrosion was strongly affected by a passive film or an adsorbed layer, which formed a barrier between the metal and solution, thus protecting the metal from further corrosion. However, during corrosive wear, the damage to the passive film in combination with generation of fresh surface can lead to rapid removal of material. The failure of the passive film is responsible for a higher  $r_{w-c}/r_{corr}$  ratio of nanocrystalline Cu deposits, observed in the present studies.

## CHAPTER 6

### GENERAL CONCLUSIONS

In the present study, nanocrystalline and microcrystalline copper deposits were made using PC and DC electrodeposition processes, respectively. Their mechanical, electrochemical and tribological properties were investigated using a number of techniques, including nano-indentation, nano-scratch, nano-wear, electron work function, electrochemical scratch and etc. Efforts were also made to study the nanocrystallization effect on material properties. Based on extensive experimental studies, the following main conclusions were drawn:

- The grain size of the nanocrystalline deposit, determined by XRD and AFM, was mainly governed by the electrodeposition parameters:  $t_{on}$ ,  $t_{off}$  and  $I_P$ . Changing these parameters is an effective way to control the grain size and corresponding properties of the deposit.
- Mechanical and tribological properties of the nanocrystalline copper deposit were markedly superior to those of the DC-plated deposit; the nanocrystalline deposit showed higher hardness, lower wear rate, and lower friction coefficient under high loads. Under light loads where the adhesive force plays a main role in friction, nc-Cu showed increased friction coefficient.

- Grain refinement improved passivation of Cu in NaOH and resulted in a more protective passive film. The passive film formed on nc-Cu was stronger and more protective than that formed on mc-Cu, with higher EWF and lower corrosion rate; however, in the H<sub>2</sub>SO<sub>4</sub> solution without passivation involved, the nc-Cu was less resistant to corrosion. There exists close correlation between EWF and corrosion rate.
- Corrosion can be enhanced significantly by mechanical attack. Under high loads, the ratio of  $r_{w-c}/r_{corr}$  of nc-Cu was higher in NaOH with passivation involved but lower in H<sub>2</sub>SO<sub>4</sub> without passivation. However, the situation was reversed under lower loads. Wear can also be enhanced by electrochemical attack. Under lower loads nc-deposit exhibited higher  $r_{c-w}/r_w$  and this ratio increased with the aggressiveness of solutions, but under higher loads no appreciable difference was found in  $r_{c-w}/r_w$  between nc-Cu and mc-one in different solutions. The synergism of corrosion and wear plays an important role during corrosive wear.

## BIBLIOGRAPHY

- [1] D. Landolt and A. Marlot. Microstructure and composition of pulse-plated metals and alloys. *Surface and Coatings Technology*, 169:8–13, 2003.
- [2] K.S. Kumar, H.Van Swygenhoven, and S. Suresh. Mechanical behavior of nanocrystalline metals and alloys. *Acta Materials*, 51:5743–5774, 2003.
- [3] M. Kohler and W. Fritzsche. *Nanotechnology: An Introduction to Nanostructuring Techniques*. Wiley-VCH, Weinheim, 2004.
- [4] R. Birringer, H. Gleiter, H.P. Klein, and P. Marquardt. Nanocrystalline materials: An approach to a novel solid structure with gas-like disorder. *Physics Letter A*, 102:365–369, 1984.
- [5] A.S. Edelstein and R.C. Cammarata. *Nanomaterials: Synthesis, Properties and Application*. Institute of Physica, Bristol, 1996.
- [6] H. Gleiter. Nanostructural materials: Basic concepts, microstructure and properties. In Z.K. Tang and P. Sheng, editors, *Nanoscience and Technology: Novel Structures and Phenomena*.
- [7] E.J. Lavernia, L.M. Lau, and H.G. Jiang. Thermal spray processing of nanocrystalline materials. In G. Chow and N.I. Noskova, editors,

*Proceedings of the NATO Advanced Study Institute on Nanostructures Materials: Science and Technology*, pages 283–302.

- [8] U. Erb, K.T. Aust, and G. Palumbo. In C.C. Koch, editor, *Nanostructured Materials-Processing, properties and Potential Application*, pages 179–215.
- [9] B.H. Kear and P.R. Strutt. *Nanostructures: The Next Generation of High Performance Bulk Materials and Coatings*, volume 4. Naval Research Reviews, 1994.
- [10] G. Palumbo, S.J. Thorpe, and K.T. Aust. Tripleline disclination effects on the mechanical behavior of materials. *Scripta Metallurgica et Materialia*, 24:2347–2350, 1990.
- [11] C. Politis and W.L. Johnson. Preparation of amorphous Ti<sub>1-x</sub>Cu<sub>x</sub> (0.10 < x < 0.87) by mechanical alloying. *Journal of Applied Physics*, 60 (3):1147–1151, 1986.
- [12] R. Z. Valiev. Approach to nanostructured solids through the studies of submicron grained polycrystals. *Nanostructured Materials*, 6:73–82, 1995.
- [13] R. Birringer and H. Gleiter. *Encyclopedia of materials science*, volume 11. Pergamon, Oxford, 1998.
- [14] H. Natter, M. Schmelzer, S. Janben, and R. Hempelmann. Nanocrystalline metals and oxides i: pulse electrodeposition. *Physical Chemistry*, 101:1706–1713, 1997.

- [15] S. Bandyopadhyay and D. Chakravorty. Preparation of nanocrystalline copper by electrodeposition. *Journal of Materials Research*, 12:2719–2724, 1997.
- [16] R.Z. Valiev, A.I. Pshenichnyuk, and A.A. NAzarov. Structural model of ultrafine grained materials produced by severe plastic-deformation. *Plasticity of Metals and Alloys-ISPMA 6 Key Engineering Materials*, 97-9:59–64, 1994.
- [17] Electrochemistry Encyclopedia. (<http://electrochem.cwru.edu/ed/encycl>).
- [18] F. Ebrahimi and Z. Ahmed. The effect of current density on properties of electrodeposited nanocrystalline nickel. *Journal of Applied Electrochemistry*, 33:733–739, 2003.
- [19] S. Shriram and S. Mohan. Electrodeposition of nanocrystalline nickel- a brief review. *Trans IMF*, 78:194–197, 2000.
- [20] S. Mohan and S. Shriram. Electrodeposition of nanocrystalline nickel. *Bulletin of Electrochemistry*, 18:241–246, 2002.
- [21] Kh.M.S. Youssef, C.C. Koch, and P.S. Fedkiw. Influence of additives and pulse electrodeposition parameters on production of nanocrystalline zinc from zinc chloride electrolytes. *Journal of the Electrochemical Society*, 151:C103–111, 2004.
- [22] H. Natter and R. Hempelmann. Nanocrystalline copper by pulse electrodeposition: the effects of organic additives, bath temperature, and ph. *Journal of Physical Chemistry*, 100:19525–19532, 1996.

- [23] S. Glasstone. Electrode potentials and the form of electrodeposited metals. *Transactions of the Faraday Society*, 31:1232–1236, 1935.
- [24] R. Mishra, B. Basu, and R. Balasubramaniam. Effect of grain size on the tribological behavior of nanocrystalline nickel. *Materials Science & Engineering A*, 373:370–373, 2004.
- [25] S.S. Kulkarni and C.D. Lokhande. Electrodeposition of nanocrystalline copper from various baths. *Bulletin of electrochemistry*, 19 (11):521–524, 2003.
- [26] Kh.M.S. Youssef, C.C. Koch, and P.S. Fedkiw. Improved corrosion behavior of nanocrystalline zinc produced by pulse-current electrodeposition. *Corrosion Science*, 46:51–64, 2004.
- [27] Kh. Saber, C.C. Koch, and P.S. Fedkiw. Pulse electrodeposition of nanocrystalline zinc. *Materials Science & Engineering A*, 341:174–181, 2003.
- [28] B.D. Cullity and S.R. Stock. *Elements of X-ray diffraction*. NJ: Prentice-Hall, Englewood Cliff, 2001.
- [29] R.A. Varin, J. Bystrzycki, and A. Calka. Effect of annealing on the microstructure ordering and hardness of ball milled cubic (Ti<sub>2</sub>) titanium trialuminide intermetallic powder. *Intermetallics*, 7:785–796, 1999.
- [30] G. Binnig, C.F. Quate, and Ch. Gerber. Atomic force microscope. *Physics Review Letter*, 56 (9):930–933, 1986.
- [31] B. Bushan. *Handbook of Micro/Nano Tribology*. CRC press, Boca Raton, 2 edition, 1999.

- [32] A.L. Weisenhorn, P.K. Hansma, T.R. Albrecht, and C.F. Quate. Forces in atomic force microscopy in air and water. *Applied Physics Letter*, 54 (26):2651–2653, 1989.
- [33] G. Meyer and N.M. Amer. Novel optical approach to atomic force microscopy. *Applied Physics Letter*, 53 (12):1045–1047, 1988.
- [34] J.A. Gallego-Jurez. Piezoelectric ceramics and ultrasonic transducers. *Journal of Physics E: Scientific Instrument*, 22:804–816, 1989.
- [35] J.H. Hoh and P.K. Hansma. Atomic force microscopy for high-resolution imaging in cell biology. *Trends Cell Biology*, 2:208–213, 1992.
- [36] Anthony C. Fisher-Cripps. *Nanoindentation*. Springer, Berlin, 2 edition, 2004.
- [37] W.A. Harrison. *Electronic structure and the properties of solids: the physics of the chemical bond*. Freeman, San Francisco, 1980.
- [38] M.A. Vasil'eV, A.A. Kosyachkov, and V.S. Mikhalekov. Method of investigating surfaces by means of changes in electron work function. *Translated from Zavodskaya Laboratoriya*, 42 (11):1370–1371, 1976.
- [39] H.B. Michaelson. Work function of the elements. *Journal of Applied Physics*, 21:536–540, 1950.
- [40] H.B. Michaelson. The work function of the elements and its periodicity. *Journal of Applied Physics*, 48:1150–1156, 1977.
- [41] X.Y. Wang and D.Y. Li. Investigation of the synergism of wear and corrosion using an electrochemical scratch technique. *Tribology Letters*, 11:117–120, 2001.

- [42] X.Y. Wang and D.Y. Li. Application of an electrochemical scratch technique to evaluate contributions of mechanical and electrochemical attacks to corrosive wear of materials. *Wear*, 259:1490–1496, 2005.
- [43] W. Li and D. Y. Li. A simple method for determination of the electron work function of different crystallographic faces of copper. *Physica State Solid*, 196 (2):390–395, 2003.
- [44] A.L. Zharin. Technique of friction monitoring. *Journal of Friction and Wear*, 14 (3):111–120, 1993.
- [45] A. L. Zharin. Application of the contact potential difference technique for on-line rubbing surface monitoring. *Tribology Letters*, 4:205–213, 1998.
- [46] D.Y. Li. Kelvin probing technique: A promising method for the determination of the yield strain of a solid under different types of stress. *Physica state solid*, 191 (2):427–434, 2002.
- [47] W. Li and D. Y. Li. Effects of dislocation on electron work function of metal surface. *Materials Science and Technology*, 18 (9):1057–1060, 2002.
- [48] W. Li and D. Y. Li. Exploring the application of the kelvin method in studying the history prior to wear and the onset of wear. *Wear*, 253:746–751, 2002.
- [49] X. Y. Wang and D. Y. Li. Mechanical and electrochemical behavior of nanocrystalline surface of 304 stainless steel. *Electrochimica Acta*, 47:3939–3947, 2002.

- [50] Y.P. Li and D.Y. Li. Experimental studies on relationships between the electron work function, adhesion, and friction for 3d transition metals. *Apply Physics*, 95:7961–7965, 2004.
- [51] W. Li and D.Y. Li. Response of the electron work function to deformation and yielding behavior of copper under different stress states. *Physica State Solid A-Applied Reserch*, 201 (9):2005–2012, 2004.
- [52] W. Li and D.Y. Li. Variations of work function and corrosion behaviors of deformed copper surfaces. *Applied Surface Science*, 240:388–395, 2005.
- [53] X.S. Guan, Z.F. Dong, and D.Y. Li. Surface nanocrystallization by sand-blasting and annealing for improved mechanical and tribological properties. *Nanotechnology*, 16:2963–2971, 2005.
- [54] M.Zhao, J.C. Li, and Q. Jiang. Hall-petch relationship in nanometer size range. *Journal of Alloys and Compounds*, 361:160–164, 2003.
- [55] K.S. Siow, A.A.O. Tay, and P. Oruganti. Mechanical properties of nanocrystalline copper and nickel. *Materials Science and Technology*, 20:285–294, 2004.
- [56] N. Perez. *Electrochemistry and Corrosion Science*. Kluwer Academic Publishers, Norwell, 2004.
- [57] R. Rofagha, R. Langer, A.M. El-Sherik, U. Erb, G. Palumbo, and K.T. Aust. The corrosion behaviour of nanocrystalline nickel. *Scripta Metallurgica et Materialia*, 25:2867–2872, 1991.

- [58] A. Barbucci, G. France, P. Matteazzi, R. Riccieri, and G. Gersola. Corrosion behaviour of nanocrystalline Cu<sub>90</sub>Ni<sub>10</sub> alloy in neutral solution containing chlorides. *Corrosion Science*, 41(3):465–475, 1999.
- [59] A. John, W. Zeiger, D. Scharnweber, and H. Worch. Surface analytical investigation of the electrochemical and corrosion behaviour of nanocrystalline Fe<sub>8</sub>. *Fresenius J Anal Chem*, 365:136–141, 1999.
- [60] S. Baitz and H. Follner. Nanocrystalline coatings in copper pipes for cold water plumbing systems. *Chemical Engineering & Technology*, 25(8):841–848, 2002.
- [61] R. Pinner. *Copper and Copper-alloy Plating*. Copper Development Association, London, 1962.
- [62] E.O. Hall. Variation of hardness of metals with grain size. *Nature*, 173:948–949, 1954.
- [63] N.J. Petch. The fracture of metals. *Progress in metal physics*, 5:1–52, 1954.
- [64] S. Bandyopadhyay and D. Chakravorty. Preparation of nanocrystalline copper by electrodeposition. *Journal of Materials Research*, 12:2719–2724, 1997.
- [65] L.H. Qian, S.C. Wang, Y.H. Zhao, and K. Lu. Microstrain effect of thermal properties of nanocrystalline Cu. *Acta Materialia*, 50:3425–3434, 2002.

- [66] L. Lu, N.R. Tao, L.B. Wang, B.Z. Ding, and K. Lu. Grain growth and strain release in nanocrystalline copper. *Journal of Applied Physics*, 89:6408–6414, 2001.
- [67] S.Y. Chang, T.K. Chang, and Y.S. Lee. Deformation behavior of electrolessly deposited ultrafine nanocrystalline copper films under instrumented nanoindentation. *Electrochemical and Solid State Letters*, 9(4):c73–c76, 2006.
- [68] K.M. Youssef, R.O. Scattergood, K.L. Murty, and C.C. Koch. Ultratough nanocrystalline copper with a narrow grain size distribution. *Applied Physics Letters*, 85 (6):929–931, 2004.
- [69] *Scanning Probe Microscopy Training Book*. Digital Instruments, 1998.
- [70] T. Watanabe. *Nano-plating*. Elsevier, Tokyo, 2004.
- [71] W. Kim and R. Weil. pulse plating effect in nickle electrodeposition. *Surface & Coating Technology*, 38:289–298, 1989.
- [72] M. Stern. Electrochemical polarization iii. further aspects of the shape of polarization curves. *Journal of the Electrochemical Society*, 104:645–650, 1957.
- [73] J. Kunze, V. Maurice, L.H. Klein, H.H. Strehblow, and P. Marcus. In situ scanning tunneling microscopy study of the anodic oxidation of cu(111) in 0.1 m naoh. *Journal of Physical Chemistry B*, 105:4263–4269, 2001.
- [74] V.Brusic, M. Frisch, B.N. Eldridge, F.P. Novak, F.B. Kaufman, B.M. Rush, and G.S. Frankel. Copper corrosion with and without inhibitors. *Journal of the Electrochemical Society*, 138(8):2253–2259, 1991.

- [75] J. Kunze, V. Maurice, L.H. Klein, H.H. Strehblow, and P. Marcus. In situ stm study of the duplex passive films formed on cu(111) and cu(001) in 0.1m naoh. *Corrosion Science*, 46:245–264, 2004.
- [76] A. Srivastava and R. Balasubramaniam. Eletrochemical impedance spectroscopy study of surface films formed on copper in aqueous environments. *Materials and Corrosion*, 56:611–618, 2005.
- [77] G. Bianchi and P. Longhi. Copper in sea-water, potential-ph diagrams. *Corrosion Science*, 13(11):853–864, 1973.
- [78] R.F. North and M.J. Pryor. Influence of corrosion product structure on corrosion rate. *Corrosion Science*, 10(5):297, 1970.
- [79] J. Kruger. The oxide films formed on copper single crystal surfaces in water: rate of growth at room temperature. *Journal of the Electrochemical Society*, 108(6):503–509, 1961.
- [80] Bhushan B., A.J. Kellock, and J.W. Ager. Characterization of chemical bonding and physical characteristics of diamond-like amorphous-carbon and diamond films. *Hournal of Materials Research*, 7 (2):404–410, 1992.
- [81] H. Czichos. *Tribology*. Elsevier, New York, 1978.
- [82] J.F. Archard. Contact and rubbing of flat surfaces. *Journal of Applied Physics*, 24 (8):981–988, 1953.
- [83] S.C. Lim, M.F. Ashby, and J.H. Brunton. Wear-rate transitions and their relationship to wear mechanisms. *Acta Metallurgica*, 35 (6):1343–1348, 1987.

- [84] S.W. Watson, F.J. Friedersdorf, B.W. Madsen, and S.D. Cramer. Methods of measuring wear corrosion synergism. *Wear*, 181:476–484 Part 2, 1995.
- [85] S. Mischler, S. Ayrault S, and D. Landolt. Investigation of tribocorrosion of tic coatings using electrochemical techniques. *Electrochemical Methods in Corrosion: Research and Application Materials Science Forum*, 247:9–18, 1997.
- [86] D. Landolt, S. Mischler, and S. Stemp. Electrochemical methods in tribocorrosion: a critical appraisal. *Electrochimica Acta*, 46:3913C3929, 2001.
- [87] A.E. Miller, P.B. Fisher, A.D. Feller, T.N. Andryushchenko, and K.C. Cadien. Chemical-mechanical planarization for semiconductors. In B.S. Covino S.D. Cramer, editor, *Corrosion: Fundamentals and Protection and Tesing*, volume 13A of *ASM Handbook*.
- [88] T.H. Tsai, Y.F. Wu, and S.C. Yen. A study of copper chemical mechanical polishing in urea-hydrogen peroxide slurry by electrochemical impedance spectroscopy. *Applied Surface Science*, 214:120–135, 2003.
- [89] X.X. Jiang, S.Z. Li, D.D. Tao, and J.X. yang. Accelerative effect of wear on corrosion of high-alloy stainless steel. *Corrosion*, 49 (10):836–841, 1993.
- [90] P. Schmutz and G.S. Frankel. Influence of dichromate ions on corrosion of pure aluminum and aa2024-t3 in nacl solution studied by afm scratching. *Journal of the Electrochemical Society*, 146 (12):4461–4472, 1999.

- [91] R.E.J. Noel and A. Ball. On the synergistic effects of abrasion and corrosion during wear. *Wear*, 87 (3):351–361, 1983.
- [92] S. Mischler, E. Rosset, G.W. Stachowiak, and D. Landolt. Effect of sulfuric-acid concentration on the rate of tribocorrosion of iron. *Wear*, 167 (2):101–108, 1993.
- [93] H. Abd-El-Kader and S. M. El-Raghy. Wear-corrosion mechanism of stainless steel in chloride media. *Corrosion Science*, 26 (8):647–653, 1986.
- [94] H. Abd-El-Kader and S. M. El-Raghy. Electrochemical kinetics of stainless steel in aerated chloride solutions during wear process. *Electrochimica Acta*, 30 (7):841–849, 1985.
- [95] X.X. Jiang, S.Z. Li, C.T. Duan, and M. Li. A study of the corrosive wear of ti-6al-4v in acidic medium. *Wear*, 129 (2):293–301, 1989.
- [96] P.D. Bastek, R.C. Newman, and R.G. Kelly. Measurement of passive film effects on scratched electrode behavior. *Journal of Electrochemical Society*, 140 (7):1884–1889, 1993.
- [97] D.G. Kolman and J.R. Scully. Limitations of potentiostatic repassivation techniques and their relationship to the applicability of the high-field approximation to the repassivation of titanium. *Journal of Electrochemical Society*, 142 (7):2179–2188, 1995.
- [98] B.W. Madsen. Measurement of erosion-corrosion synergism with a slurry wear test apparatus. *Wear*, 123:127–142, 1988.

- [99] Y.L. Huang, X.X. Jiang, and S.Z. Li. Pure mechanical wear loss measurement in corrosive wear. *Bulletin of Materials Science, Indian Academy of Sciences*, 23 (6):539–542, 2000.
- [100] W. Schumacher. High-temperature wear of stainless steel. *Materials Engineering*, 101 (3):23–25, 1985.